RECONFIGURABLE MICROWAVE ELECTRONICS USING ADDITIVE MANUFACTURING AND MAGNETIC NANOMATERIALS

By

Yuxiao He

A DISSERTATION

Submitted to
Michigan State University
in partial fulfillment of the requirements
for the degree of

Electrical Engineering - Doctor of Philosophy

2020

ABSTRACT

RECONFIGURABLE MICROWAVE ELECTRONICS USING ADDITIVE MANUFACTURING AND MAGNETIC NANOMATERIALS

By

Yuxiao He

This dissertation investigates how to design and fabricate low cost, lightweight, and reconfigurable RF and microwave electronics using additive manufacturing and nanomagnetic materials. A key goal is to provide a specific methodology on obtaining high performance RF electronics by taking advantage of the expanded design freedom, economic fabrication process offered by the additive manufacturing technology, as well as the unique microwave properties of the magnetic nanomaterials. A number of commonly used RF and microwave electronics are designed, fabricated, and measured to demonstrate that we have successfully achieved such goal. The performance tradeoffs of the above two approaches during experimental implementation are also discussed for each specific circuit and component category, depending on the corresponding desired performance. This in turn provides us with practical and important comments regarding the limitations of our approaches. Therefore, we can obtain an insightful guideline for achieving our key goal in terms of both design potentials and implementation capabilities. The first chapter addresses the current trend of smaller, smarter, and cheaper electronics which motivates our work in this dissertation. The second chapter provides the background on additive manufacturing technology and magnetic materials that were utilized as two separate approaches to achieve high performance and low cost RF and microwave applications prior to this work. Based on such context, we are motivated to propose a new thrust which pushes the boundaries beyond the current development of both approaches and explores the new realm of combining them together. The third chapter introduces several types of additive manufacturing techniques, and presents a number of lightweight, reconfigurable, and high performance RF components that are developed using one or two techniques and in a combined manner. Manufacturing factors that negatively

affects the RF performance are analyzed and discussed with the corresponding technique to alleviate such issue. In chapter four, we study the fundamental properties of the magnetic materials and explore the potential of using the magnetic nanomaterials fabricated by novel chemical methods in microwave applications operating at frequencies higher than a traditional range. The magnetic nanoparticle thin films were fabricated using various composites and were characterized for high frequency RF applications. Chapter five expands our work by combining the additive manufacturing technology, magnetic nanoparticle films, and liquid crystal polymer substrate to develop low cost, miniaturized, and reconfigurable RF components with compact and lightweight packages. The fabrication process is optimized by considering the practical limitations from chapter two, and enhanced RF performances are obtained in several applications. However, tradeoffs due to the magnetic materials are also observed, which are then theoretically analyzed and verified by the measurement results. Our work has successfully demonstrated how the RF and microwave components and circuits can be made as low cost, compact, and lightweight with enhanced performance using additive manufacturing and magnetic nanomaterials. Future work will continue by exploring new design capabilities and optimizing the fabrication process to further improve the performance while reducing the overall fabrication cost.

To my parents, my wife, families and friends.

TABLE OF CONTENTS

LIST OF TABLES

LIST OF FIGURES

CHAPTER 1
INTRODUCTION

1.1 Motivation

In recent years, we have witnessed the fast expansion of the consumer electronics market, including smart electronics which can perform a number of jobs just beyond their basic function, such as smart phones, smart watches, and smart home speakers. The additional functions offered by those smart electronics are mostly achieved wirelessly through wireless communication network or sensors using delicate electronics modules that are integrated within the device housing. The emerging trend of industrial design often dictates that those devices have to be aesthetically appealing, such as sleek and slim, compact and conformal, low-profile and lightweight; while at the same time the functions of the devices cannot be compromised or may even require more functions to be included in the next production generation. Therefore, such trends pose a critical challenge to the design of electronics that all the circuits and components have to be highly integrated and miniaturized, but with maintained or better performance. On the other hand, the cost of massive production for such highly integrated circuits will increase as better fabrication precision is needed, especially at high frequency range. However, to balance the final price of the product and the profit margin, it is pivotal to greatly reduce the overall fabrication cost through low-cost and efficient manufacturing techniques.

As one of the most important parts for those smart electronics to perform wirelessly, the RF front end in such applications has to be compact, robust, and power efficient. The fact that many services or functions in the devices operate at different frequencies demands that the RF front end circuits sometimes may also need to be reconfigurable, since it is difficult to put one or more independent RF front ends that operate at every corresponding frequency band into the already tight device housing. Especially with the advent of 5G, the cellphone antennas for example, have to be compatible with the 4G LTE low band around 1 GHz and the 5G high band around 5.9 GHz, so that the antennas have to be designed either with multi-band characteristics or with reconfiguration capabilities. As a result, it is advantageous to have one set of RF front end that can be reconfigured to operate at two or more frequency bands. Again, as we mentioned previously, the overall package of the RF circuits need to be miniaturized and lightweight, and with the fabrication cost to be greatly reduced. Therefore, to comply with the current trend and need of small and high performance electronics, we are aiming to investigate new methodologies to design and fabricate low cost, lightweight, and reconfigurable RF circuits and components.

1.2 Problem Formulation

To achieve the aforementioned goal, we propose to use additive manufacturing technology and nanomagnetic thin films. Additive manufacturing is well known for fast prototyping, low cost, and environmental friendliness. For example, additive manufacturing can print a whole piece of complex 3D structure without laborious cutting and modeling compared to the traditional manufacturing process. Recently, this technology has attracted extensive focus on applying it to RF and microwave applications. In this thesis, we target the design of high performance RF circuits and components by taking advantage of the extra design freedom offered by the additive manufacturing, as well as fabricating the prototype with compact and lightweight package in a low-cost manner. Moreover, the RF reconfigurability also may be achieved through designing and fabricating special fixtures of the RF circuits which are usually hard and costly and realizable by traditional forging process. However, the major RF reconfigurability mechanism we propose here is through the magnetic tuning using magnetic nanoparticles thin film, as opposed to the commonly used electronically tuning approach. Nevertheless, some important properties of the magnetic nanoparticles thin film have to be first studied in order to control this unique magnetic tuning mechanism, which involves the fabrication and characterization of the magnetic nanoparticle films. In addition, since the relative permeability μ_r of magnetic nanoparticles is usually greater than unity, i.e., $\mu_r \gg 1$, depending on the specific characteristics such as types of the composites, film thickness, fill factor of the magnetic nanoparticles films, thus we can utilize this property to miniaturize the RF circuits, while exploring the potential performance improvement and tradeoffs as well. Ultimately, we would like to investigate a way to combine both additive manufacturing technology and the magnetic nanoparticle thin films to design and fabricate low cost, compact, and high performance RF circuits and components.

To elaborate the above statements concisely, we formulate our problem in this thesis in the following points:

- Develop novel RF circuits and components by taking advantage of extra design freedom offered by additive manufacturing technology.

- Investigate the fabrication process for specific RF applications using stand-alone or combined additive manufacturing technologies to achieve satisfying performance.

- Characterize and fabricate the magnetic nanoparticle thin films for high frequency RF applications.

- Utilize the magnetic nanoparticle thin films to achieve RF reconfigurability and circuit miniaturization.

- Implement both additive manufacturing technology and magnetic nanoparticle films to obtain low cost, lightweight, miniaturized, and reconfigurable RF circuits and components.

- Discuss the potential, limitation, and tradeoff of applying both additive manufacturing technology and magnetic nanoparticle films onto RF applications

1.3 Thesis Statement

This dissertation consists of a series of studies that allow for the development of compact and miniaturized, lightweight and reconfigurable RF components. The main contributions of the present work include: investigation of using one or two additive manufacturing technologies and liquid crystal polymer substrate to develop novel RF circuits including filters, transmission lines, resonators, and antennas; fabrication and characterization of magnetic nanoparticle films; the development of miniaturized and reconfigurable RF circuits with low cost and lightweight packages combining both additive manufacturing technology: and magnetic nanoparticle thin films, which provides an unique approach and expanded vision of tackling the problem of smaller, smarter, and cheaper electronics.

Thesis Statement: *By applying the additive manufacturing technology onto various RF applications and characterizing the magnetic nanoparticle thin films, we intend to propose novel RF circuit design and efficient fabrication process to significantly reduce the overall fabrication cost, and shrink the circuit package size while obtaining the RF reconfigurability.*

1.4 Anticipated Research Contributions

This dissertation will directly address each of the research problems listed in **Section 1.2**. Various novel RF components utilizing one or two additive manufacturing technologies were successfully designed, fabricated and measured, pushing the boundary of applying additive manufacturing technology into RF applications. By fabricating magnetic nanoparticle films using various composites and low cost chemical methods, we are able to characterize the films to study their important properties for high frequency RF and microwave applications. Based on the above two foundations, we are capable of designing RF components with very low cost, compact and miniaturized packaging, enhanced RF performance and reconfigurability. The theoretical analysis are also carried out to provide some insightful understanding in terms of the physics behavior, design potentials, and performance tradeoffs. Therefore, it paves the way to implement such configuration and technology in monolithic RF and microwave applications.

1.5 Dissertation Outline

The remainder of this dissertation is organized as follows; in **Chapter 2** the background information on additive manufacturing technology in terms of its history original, current development, types of implementation techniques, and especially the research on applying it onto RF applications is provided. Similarly, we also discuss the usage of magnetic materials including ferrites and ferrites based magnetic thin films in RF and microwave circuits and analyze the potential and limitation of using magnetic nanoparticles thin films in such applications operating at much higher frequency.

In **Chapter 3**, we demonstrate a number of RF components that are designed by taking advantage of the extra design freedom offered by the additive manufacturing technology. They are fabricated using one or two additive manufacturing technologies. The measurement results show satisfying performance compared to the counterparts fabricated by the traditional approaches, while the overall fabrication cost is significantly reduced. Also, RF reconfigurability can be achieved by designing special fixtures in certain applications which also exhibits the great potential of using additive manufacturing technology to implement high performance RF circuits and components. Based on the experimental results, we also discuss the limitations of such technology from a practical point of view, especially when it is intended to be used in a high frequency range.

Chapter 4 first studies several properties of the magnetic materials that are particularly important for RF and microwave applications operating at high frequencies. Then we demonstrate the magnetic thin films that are made with various composites through two novel and low cost chemical methods. The characterization of the fabricated magnetic nanoparticle films proves the efficiency of the chemical methods thus enabling us to make much thicker films, and granting us the vast potential of using such films to make miniaturized and reconfigurable RF circuits and components.

Based on the foundations of the previous two chapters, in **Chapter 5**, we propose a thrust of combining additive manufacturing and magnetic nanoparticle thin films to implement high performance and reconfigurable RF components with low cost, lightweight, and miniaturized packages. In this chapter, we demonstrate a number of RF components using unique design configurations to achieve our goal, also the fabrication process is optimized based on the practical considerations offered by **Chapter 3** and our extensive experiment trials. Additionally, theoretical analysis is performed to provide physical explanation on the measured results of our fabricated samples, thus we can obtain some insightful understanding and design guideline of using such configurations. **Chapter 6** demonstrates a bandstop filter using the similar topology shown in **Chapter 5**, such that a tunable stop band can be achieved. **Chapter 5** and **Chapter 6** showcases the tunable and high performance planar RF devices with low cost and light-weight packages using additive manufacturing and magnetic materials. **Chapter 7** presents a 3D printed spherical cavity resonator with fine tuning using magnetic materials. Additionaly, the theoretical analysis is carried out to understand the tuning mechanism, fabrication process, measurement results, and comparison with the state-of-the-art. Finally, **Chapter 8** draws the conclusions and summarizes the contributions of this dissertation.

CHAPTER 2
BACKGROUND

Originally developed as a more efficient way to build objects with complex shapes, additive manufacturing technology has now become an alternative approach to manufacturing mechanic objects, compared to the conventional machining, casting, and forging process, where materials are removed from a stock item or poured into a mold and shaped by means of dies, press and hammers. Therefore, additive manufacturing uses less material and thus produces less waste. Although it is commonly used in automobile and aerospace industries to make mechanic parts, recently people have explored using such technology to design and fabricate RF circuits and components. However, applying such technology in high frequency range RF and microwave applications is still in its the early stages.

In the 1940s, ferrites were first investigated to be used in microwave applications, especially for spinel and hexagonal ferrite families, and because of the intense interest from the military in the 1950s and 1960s using ferrite phase shifters in phased array radar, research on the use of ferrites materials in microwave applications underwent a vast transformation. By the 1980s, conventional ferrites used in microwave applications reached its maturity. Due to the excessive magnetic loss, these conventional ferrite materials found their applications up to Ka-band. In the beginning of the 20-th century, people were able to synthesis ferrite based thin films, which enabled their applications operating at much higher frequency. Recently, thin films made of spinel magnetic nanoparticles were demonstrated in several RF applications with operating frequencies at several GHz, which shows great potential in using such films in high frequency RF and millimeter wave applications.

2.1 Background of additive manufacturing technology

It is well known that additive manufacturing (AM) technology has a number of advantages compared to the traditional fabrication process such as milling and machining. The AM technology usually builds 3D objects in an additive layer-by-layer manner, which is why it is often synonymously called 3D printing. The materials used for printing can be plastic, metal, rubber, and possibly any material that would fit the printer configuration. In retrospect, the AM technology was originally investigated by Hideo Kodama of Nagoya Municipal Industrial Research Institute in 1981, where the three dimensional objects were printed using photo-hardening thermoset polymer and then cured by UV exposure. A more close-to-modern 3D printing technology was developed at Massachusetts Institute of Technology in 1993, where the inkjet printer head was employed in a power bed processing. The founding of several corporations based on this technology in 1993 demonstrates the commercialization of AM technology. With decades of development, the AM technology has merged into several types of techniques, each of them having its own unique way of executing the 3D printing process which we are going to introduce in the following subsections.

2.1.1 General 3D printing process

Although different AM techniques have their unique printing characteristics, the general 3D printing process involves several common phases.

2.1.1.1 Modeling

First, the 3D object that is intended for printing has to be modeled in a computer-aided design (CAD) software. Although other methods such as 3D scanner, plain digital camera, and photogrammetry software may be used for the same purpose, CAD file is preferable as it allows for modification before printing is executed, thus it is more flexible and use-friendly. The format CAD file is commonly saved as stereolithography file format (STL) which stores the data based on triangulations of the surface of CAD models. This type of file has relatively large file size since it contains topology optimized parts and lattice structures due to the large number of surfaces involved. In 2011, a new file format called Additive Manufacturing File Format (AMF) was introduced where data is based on curved triangulations and thus is more suitable for AM and has accordingly smaller file size. However, due to practical issues, we are using the STL format CAD file since it is still widely used in most 3D printers.

2.1.1.2 3D Printing

The the verified error-free STL file is then imported to a special ”slider” software which basically converts the 3D model into a stack-up of multiple thin layers, which provides a sort of printing guide for the 3D printer since as we mentioned before, the 3D printing process builds the objects in a layer-by-layer manner. Then the generated guide file is read by the client 3D printer to execute the printing process. Since the actual speed of different printers may vary, the consumed printing time is different for similar objects. In general, the lead time of a 3D printing process is significantly less than the conventional fabrication process, for example it usually takes at most a day to 3D print a batch of ten 50 mm $\times$ 50 mm squares in house whereas it may take several weeks or months for out-sourced foundry manufacture. Hence, 3D printing is much more efficient for fast prototype.

2.1.1.3 Polishing

After the printing process is complete, the object is taken out from the printing tray, and depending on the types of 3D printing techniques, the objects may need to be cleaned to eliminate the supporting materials in some structures like holes and bridges. Usually this cleaning process can be easily done by flashing away the supporting materials using water. Most of the 3D printed objects have to thereafter undergo a polishing process to get better surface finishing. Especially for RF and microwave applications, the surface roughness will strongly affect the surface resistance, and given that the skin depth at high frequency tends to be small, poor surface roughness will result in the surface current being heavily attenuated. In general, the surfaces of the printed objects can be polished using very fine sandpapers or machine sanders, however, more advanced approaches must be developed in order to further improve the performance of the applications used at a much higher frequency range. It also has to be pointed out that in some cases where the 3D printed surface is very thin, for example a 3D printed dielectric substrate which only has several tenths of micrometers, the polishing process handled by human hand or simple machine will most likely create inevitable large concave area on the horizontal substrate surface, which may end up with even worse negative effects on the surface current and thus the RF performance. Therefore, in such a scenario, (i.e., a very thin or fragile 3D printed object), we usually do not polish the surface in order to maintain the geometric integrity of the 3D printed piece. Instead, alternative methods may be applied to address the surface roughness to create a smoother surface finish, such as coating the surface with another thin layer of material to fill the saw-like gaps of the rough surfaces, or applying special chemical etching solution onto the surface to eliminate such saw-like gaps. When the surface roughness will not heavily affect the RF performance, no polishing is needed in this case to maintain the simplicity of the fabrication process.

2.1.1.4 Metalization

Ideally, 3D printing can print any material that is fit for the printer, however, current development only allows for using limited a number of materials, such as plastic, rubber, and metal powder based filament. In general , for RF and microwave applications, researchers often choose to first print the circuit or component structures using non-metal materials, such as plastic waveguides and plastic horn antennas, then after surface polishing, metalize the needed surfaces of the objects. This metalization process can be performed either through sputtering or electroplating, or combineinf both. For example, in a combined manner, the target surfaces are fist sputter with 0.5 - 1 μm of Titanium which serves as the seed/adhesion layer, then the object is soaked into the electrolyte solution to electroplate the target surfaces with desired metal, such as copper or aluminum. The thickness of the final metal layer can be controlled by adjusting the parameters of electroplating process including processing time, current amplitude, and electrolyte density. As we previously stated, metal can also be 3D printed using power based filament, or using nanoparticle based solution. However, the conductivity of those materials becomes the most critical issue for the RF application usage. For power based filament, the conductivity is currently 50% of copper at best, whereas due to the aforementioned surface roughness issue and actual object geometry, the actual conductivity will be lower. While for the nanoparticle based solution, special curing process has to be carried out to get good conductivity. The best reported and most promising conductivity is 80% silver using a heat curing process. However, such a curing process has several practical limitations, because it acts a major barrier in cases where low thermal temperature dielectric materials are used with the printed silver.

2.1.2 Types of AM techniques

For the past few decades, AM technology has merged into several types of techniques which feature different printing characteristics in term of materials, ways of constructing models, and printing time. In the following, we will focus on some of the popular techniques and give a brief description for each of them.

2.1.2.1 Stereolithography (SLA)

This technique builds objects in a pool of photopolymer resin. Using the sliced STL file, the printer laser beam directing into the pool of resin traces the cross-section pattern of the model for each sliced particular layer, then prints and cures layer-upon-layer until the whole structure of the object is finished. Specialized material may be needed to add support to some model features. Models can be machined and used as patterns for injection molding, thermoforming or other casting processes. Figure 2.1 shows an SLA printer produced by FormLabs.

Figure 2.1: Form 3L SLA 3D printer [1]

2.1.2.2 Fused Deposition Modeling (FDM)

Similar to SLA, FDM constructs objects layer by layer using thermoplastic from the very bottom up. The so called thermoplastic transforms to liquid upon the application of heat and solidifies to a solid when cooled. First, the printer heats the theormplastic until its melting point and extrudes it through a nozzle on a printing platform or tray, on a predetermined pattern determined by the 3D model and Slicer software. Just like the SLA process, the nozzles trace the cross-section pattern for each particular layer with the thermoplastic material hardening prior to the application of the next layer. The process repeats until the build or model is completed. In addition to thermoplastic, a printer may extrude support materials too, which can be flashed away using water. Figure 2.2 shows a professional grade FDM printer develped by Stratasys Inc.

2.1.2.3 Digital Light Processing (DLP)

DLP is another popular 3D printing process that is widely used in the production of projectors. Larry Hornbeck of Texas Instruments, first invented this type of technique in 1987. Due to the fact that it utilizes digital micromirrors laid out on a semiconductor chip, DLP's

Figure 2.2: Stratasys Fortys 450mc 3D printer [2]

applications include mobile phones, film projectors, and many 3D printing applications.

2.1.2.4 Selective Laser Sintering (SLS)

Quite similar to SLA, SLS builds the objects in a layer-upon-layer manner using a laser as power supply to sinter the power based plastic, metal, ceramic or glass, to form strong 3D printed objects. However, no supporting material is needed for SLS as the build is supported by unsintered material.

2.1.2.5 Polyjet

Developed by Stratasys Inc, Polyjet technology produces high quality 3D objects with more realistic finishes compared to the aforementioned techniques. PolyJet builds by jetting layers of liquid photopolymer at 27 micronmeters (0.00106") layer by layer as a UV light cures simultaneously. PolyJet can print rigid and flexible materials in a single build to create over-molded parts without tooling. The technology delivers parts with shore hardness ranging from 30A-95A. Because PolyJet does not require hard tooling to deliver an over-molded part, it is frequently used for prototypes requiring an elastomeric surface, such as grips or buttons, or for testing material hardness. PolyJet can also print parts with a variety of flexibilities, from rubber-like parts to those that have a more rigid feel. The benefits of polyjet include the following:

1. Creating smooth, detailed prototypes that convey final-product aesthetics.

2. Producing accurate molds, jigs, fixtures and other manufacturing tools.

3. Achieving complex shapes, intricate details and delicate features.

4. Incorporating the widest variety of colors and materials into a single model for unbeatable efficiency.

The Polyjet printer we used is the Connex Objet350 from Stratasys, which is shown in Figure 2.3

Figure 2.3: Stratasys Connex Objet350 3D printer [2]

2.1.2.6 Aerosol Jet Printing (AJP)

Unlike the above techniques, AJP achieves the 3D printing process by directly printing the objects using a dense aerosol of materials, such as silver nanoparticles and polyimide materials. First, the printing materials are usually diluted with water or other solution, then they are atomized using either pneumatic atomizer or ultrasonic atomizer. Then the atomized materials are mixed with carrier gas, for example Nitrogen gas, to create a dense aerosol into the printing nozzle. The sheath gas injected into the nozzle helps to shape and focus the aerosol, delivering high resolution of the printed trace. In addition, some advanced AJP printed, for example the Optomec AJ 5X system shown in Figure 2.4, the printing platform can be rotated during the printing process. Along with the X,Y,Z moving directions of the printing head, such system offers higher flexibility that allows for printing extremely complex objects with much higher precision. The advantages of AJP technique

Figure 2.4: Optomec AJ 5X system [3]

are the following:

1. Feature resolutions from 10 microns to millimeters.

2. Conformal printing on non-planar and 3D surfaces.

3. Print interconnects and active/passive components.

4. Print using commercially-available materials and bio-materials Print bio-materials.

5. Print on plastic, ceramic, and metallic substrates.

6. Scalable to support high-volume production requirements.

Because of the above advantages, the AJP technique is ideally suited for 3D Printed Electronics applications such as fully printed antennas, sensors, and Molded Interconnect Devices (MIDs).

2.1.3 3D printing in RF and microwave applications

Since 2005, researchers all around the world have worked on applying 3D printing technology into various RF applications. Among these, SLA, Polyjet, and AJP techniques are the most widely used 3D printing technologies. In general, this work involves the characterization of the materials used for 3D printing, fabrication of lightweight, low cost RF components compared to the traditional counterparts, novel design for ultra-low loss, compact passive RF circuits and sensors, integration of active and passive components using 3D printed interconnects and packages.

One of the important purposes of applying 3D printing technology in RF application is to reduce the cost and weight of the fabricated circuits or packages while obtaining close or the same performance of the conventional counterparts. For this purpose, people have found that the fabrication process usually play a pivotal role. Except AJP, all the other 3D printing techniques employed in RF applications rely on the printed dielectrics like plastic to form the structural object for the RF circuits and components. For example, a waveguide is first realized by 3D printing the pipe-like structure using either SLA or Polyjet, then the inner surfaces of the structure have to be metalized to actually achieve the RF functionality of the waveguide. During this process, the surface roughness of the inner walls of the waveguide which is dictated by the resolution of the printer heavily affects the RF performance of the waveguide, i.e., the transmission and reflection coefficient. Depending on the actual metalization process, the geometric shape of the waveguide may be affected, for example warpage due to the heat during the metal sputtering process, which will cause the wave propagation characteristics to be changed such as the modes of the wave and the cutoff frequency of the waveguide. For this reason, researchers have experimented using a number of approaches to address this issue.

As for the AJP, although great potential can be realized with higher resolution and printing capabilities, the most critical problem which hinders its applicability into production realization still comes from the fabrication process. Unlike the SLA, FDM, and Polyjet which can print a relatively large object in a short amount of time in a layer-by-layer fashion, AJP features tens of micrometers of ultra high resolution single printed trace, it is unrealistic to print bulk geometry using AJP, but rather, to print extreme compact planar RF circuits, such as transmission lines, interconnects, and millimeter wave antennas and power dividers. Also, due to the nature of aerosol, the issue of overspray is inevitable which poses a major problem when for example, the printed circuit is down to 20 μm and thus is close to the AJP printing resolution range. On the other hand, the surface roughness still exists however is more controllable since such surface roughness is actually determined by the extent of overlapping between adjacent printed traces. Therefore, a careful study and experiment in terms of the amount of materials fed to the printer, the printing speed, the clearance between the print head and the printing platform, and so on has to be carried out to find the best configuration of the system for achieving the best surface roughness. Besides, since AJP can easily print the metal using the uncured silver nanoparticles, it is desirable to find the best curing process to achieve high conductivity to ensure good RF performance of the printed circuitry. Currently, two major curing methods, UV exposure and heat curing, are tested to achieve moderate to high conductivity ranging from 20% - 80%, however, practical limitations may prevent them from achieving the best tested conductivity. For example, when the silver nanoparticles are printed on top of some dielectrics with low glass transition temperature, the heating method which usually requires very high curing temperature will be less effective.

Therefore, an important research direction is how to minimize the negative effect caused by the fabrication process on RF performance through better utilizing 3D printing technologies to propose new design, and combining other effective techniques to further improve the overall RF performance. It will be interesting and challenging to combine one or more 3D printing techniques to obtain higher printing capabilities, in particular for some designs that are theoretically beneficial but hard to realize using conventional fabrication process or just a single 3D technique. By doing so lower fabrication cost and better RF performance are expected to be achieved compared to single 3D printing technique strategy.

2.2 Background of magnetic materials in RF applications

It is widely known that magnetic materials in RF applications are usually referred to microwave ferrite devices because of extensive research that was done from the 1940s to 1980s. Microwave ferrite devices permit the control of microwave propagation by a static or switchable DC-magnetic field. The devices can be reciprocal or nonreciprocal, linear or nonlinear, and their development requires a knowledge of magnetic materials, electromagnetic theory, and microwave circuit theory. Unlike a magnetic metal, a ferrite is a magnetic dielectric that allows an electromagnetic wave to penetrate the ferrite, thereby permitting an interaction between the wave and magnetization within the ferrite. However, due to the excessive magnetic loss at high frequency and the vast development of silicon technology, the traditional ferrite materials are less used in the >600 MHz high frequency applications. Since 2004, ferrite based magnetic thin films have been developed and characterized to have high demagnetization which enables them to be used at GHz range even under self-biased condition. This implies the magnetic nanoparticle thin films have great potential in RF and millimeter wave applications.

2.2.1 Traditional microwave ferrite devices

2.2.1.1 Circulators and isolators

In microwave systems that use a single antenna aperture for both sending and receiving, the function of circulators is primarily to facilitate the routing of outgoing and incoming signals to the transmitter or receiver as appropriate. This is illustrated in Figure 2.5, which shows a schematic diagram of a phased-array antenna module using a switchable circulator in addition to an ordinary (nonswitchable) circulator. The module also contains two T/R switches. Their function can also be satisfied by two further circulators, but switches are generally preferred in these locations because of cost and size considerations. Circulators and isolators are made possible by the nonreciprocal character of the microwave behavior of ferrites (and certain other materials).

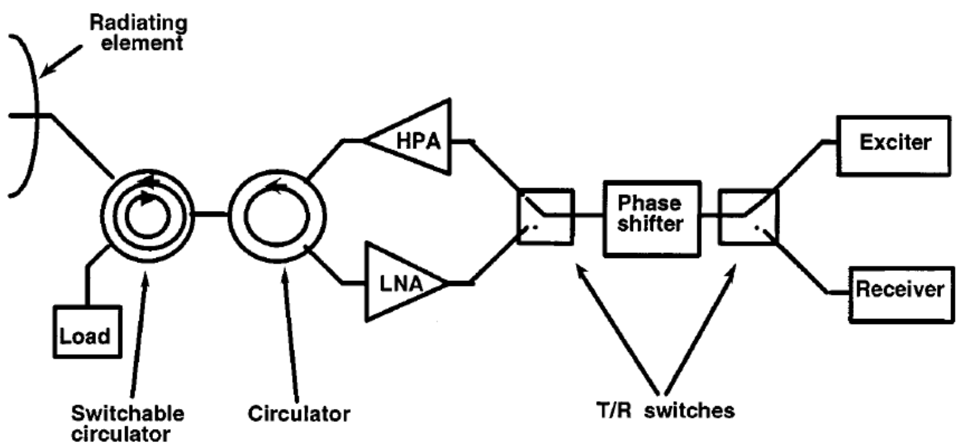

Figure 2.5: Schematic diagram of phased array antenna module [4]

In microwave systems that use separate antenna apertures for sending and receiving, nonreciprocal devices are required in order to control the voltage standing-wave ratio (VSWR) seen by the high-power amplifier at the output of the transmitter, and also to control undesirable reflections from the receive antenna array. In this case, isolators rather than circulators are required. These isolators can be made by connecting a matched load to one of the ports of a circulator, but under some conditions, a "dedicated" isolator design may be preferable.

2.2.1.2 Ferrite phase shifters

Ferrite phase shifters generally take advantage of the ability to control the permeability of a waveguiding medium to vary the phase velocity of a microwave signal passing through it. In most cases, the change in permeability changes the phase velocity and, therefore, the insertion phase. In a few cases, such as in the rotary field phase shifter, the orientation of the internal magnetization controls the phase shift. A meander line can be used to enhance the phase shift by generating a circularly polarized RF magnetic field around the center conductor, as shown in Figure 2.6. The main use of ferrite phase shifters is in phased-array antenna systems. The direction of a beam radiated by an array of elements in a linear array can be steered by inserting a different phase shift in each radiators feed. A phase control range of only 360^o is required, but that full 360^o range is required regardless of the scan angle.

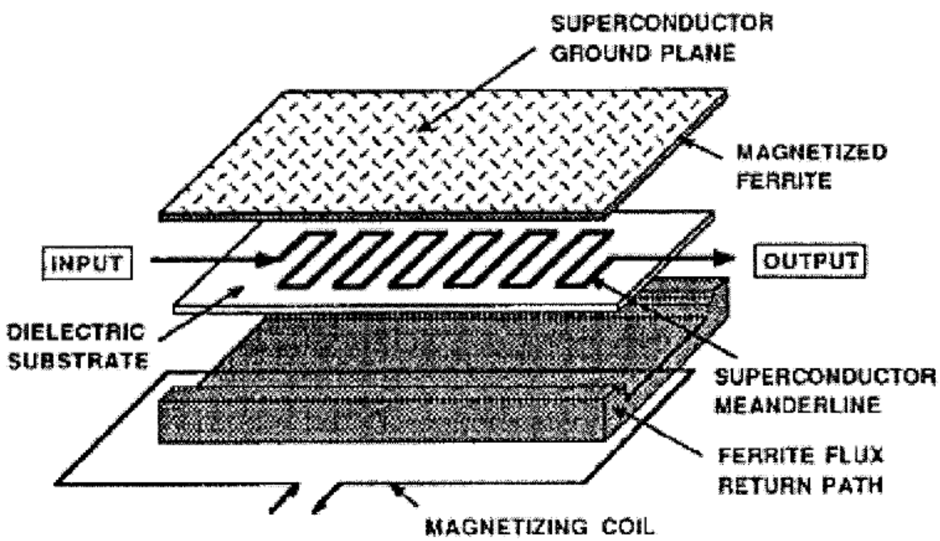

Figure 2.6: Superconducting meander-line phase shifter [4]

2.2.1.3 YIG filters

In Grenoble, France, in 1956, Bertaut and his colleagues synthesized the rare-earth iron garnets and analyzed their magnetic characteristics. These findings were quickly replicated and refined by Geller and Gilleo at BTL, and then expanded to form a base of crystallographic and magnetic data for most of the known garnet compounds, the most important of which was yttriumiron garnet (YIG). By the end of the decade, both the spinel and garnet systems were becoming available to microwave device engineers. Relying on the FMR of the single crystal YIG, electronically tunable microwave filters can be achieved by integrating the YIG sphere into the filter package. Basically, because of the narrow linewidth of YIG, i.e., ΔH<0.5 Oe, yields the potential unloaded quality factor $Q = f/(\gamma \Delta H)$ >5000 at 10 GHz, where γ = 2.8 MHz/Oe is the gyromagnetic ratio. The negative permeability shown by ferrite materials at frequencies higher than the FMR frequency enables wave propagation in structures with arbitrary small cross section over limited frequency ranges. These are referred to as Magnetodielectric Surface Waves (MSW) since the electric-field contribution is negligibly small. The theory and experiments were performed specially on planar epitaxial YIG films spaced from conducting ground planes, an example of YIG film based MSG filter is shown in Figure 2.7.

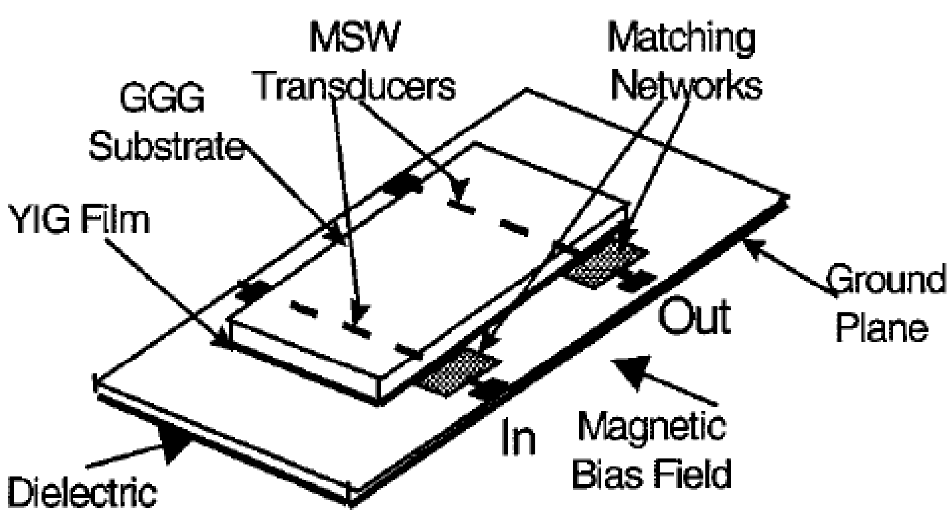

Figure 2.7: Simple MSW device with microstrip transducers. Depending on design, this can provide time delay and filtering functions [4]

2.2.1.4 Frequency selective limiter

In a high-signal density environment, receivers and signal processors are easily overloaded in this situation. An ordinary diode limiter placed in front of a wide-band receiver to limit the high-level signals, will attenuate all signals by the same amount. A frequency selective limiter (FSL) is defined as one that can attenuate strong signals without attenuating other weaker signals present simultaneously, as illustrated in Figure 2.8. Most microwave FSLs utilize the

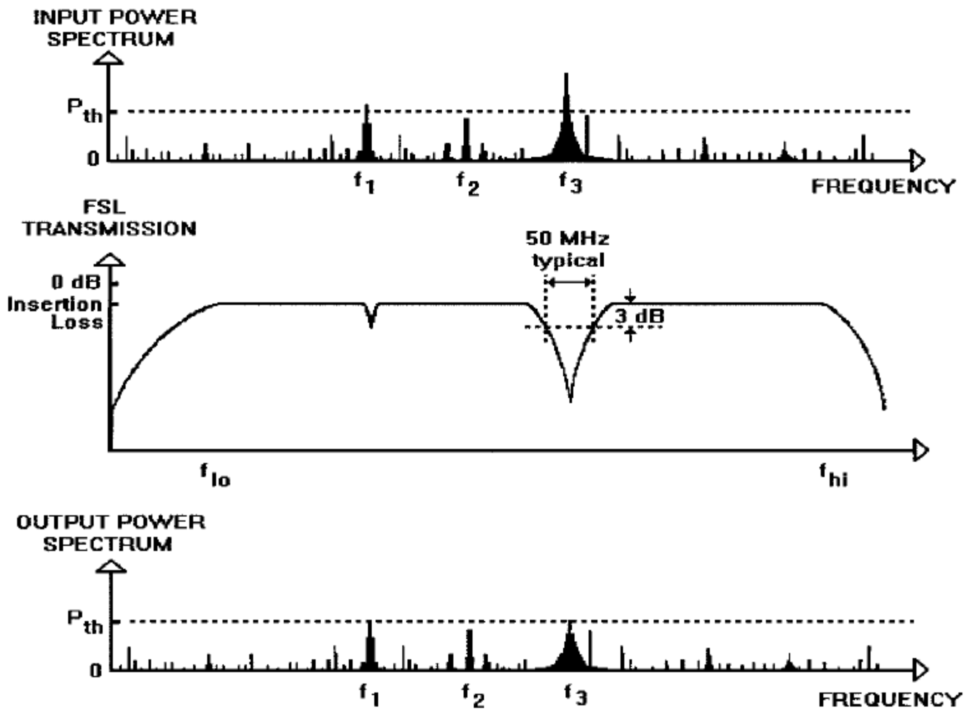

Figure 2.8: Frequency response of an FSL, and input and output power spectra, from multiple weak and strong signals, showing the frequency selectivity inherent in YIG limiters [4]

frequency-selective nature of a magnetized ferrite. Above a critical RF magnetic-field level, the spin precession angle can increase no further, and coupling to higher order spin waves begins to grow exponentially. Energy is efficiently coupled to spin waves at approximately one-half the signal frequency and then into lattice vibrations (heat) in the ferrite. The critical field strength is proportional to the spinwave linewidth of the ferrite, and because of the narrow linewidth of YIG, it can be used in high power FSLs severing as the receiver protector to prevent burnout. Ferrite FSLs have been achieved in a variety of transmission line structures, for example stripline using single crystal YIG film, while another type of FSL is based on the nonlinear excitation of spin waves in structures that can propagate MSW.

2.2.2 RF devices using magnetic nanoparticle films

The traditional ferrite materials have magnetic loss due to the lower FMR frequency which caps them to be used at RF applications at very high frequencies, especially for antennas. Recently, the ferrite based magnetic nanoparticle based thin films have been developed and characterized to have high magnetization saturation, which results in the FMR frequency can be as high as several GHz. This implies such magnetic thin films can be used in RF and millimeter wave applications. In the past decade, researchers have used such thin films in antennas and filters to achieve circuit miniaturization and performance enhancement. For example, under self-biased conditions, it has been demonstrated that the patch antennas can be first fabricated on a regular PCB substrate, then multiple layers of magnetic films are deposited on top of the antenna acting as the superstrate, which can shift down the resonant frequency as well as increase the impedance bandwidth and efficiency. The thickness of single layer film is typically 2 μm, and each film layer is constructed as the magnetic nanoparticles are sandwiched in between two protective polymer thin layers. Depending on how much magnetic film layers are deposited, the resonant frequency can be shifted down to tens of MHz, while the antenna efficiency can be enhanced by at most 40%. However, the magnetic film layer deposition process is rather complicated which prevents such method from making thick enough magnetic films, thus large resonant frequency shift is hard to achieve. In other words, the potential of miniaturizing the overall package cannot be realized. On the other hand, by applying the DC magnetic bias, the FMR frequency of the magnetic films can be tuned. Using the similar superstrate configuration, a transmission line based tunable bandstop filter was demonstrated to achieve a relatively wide tuning range by applying moderate DC magnetic bias. Nevertheless, the reported bandstop filter shows large insertion loss within the operation frequency range, which again due to the magnetic loss of the film and the dielectric loss of the PCB substrate.

Therefore, to better utilize the magnetic nanoparticle films in high frequency RF applications, three important issues have to be addressed.

1. Fabricate magnetic films using low cost and effective method to have large thickness, good fill factor, and acceptable surface roughness

2. Characterize the fabricated films to determine important properties of the films including FMR frequency, magnetization saturation, and the relative permeability

3. Propose better design to integrate the magnetic films into RF applications to improve the RF performance while obtain compact, robust, and minimized overall package

2.3 Summary

This chapter discussed the backgrounds of both additive manufacturing and magnetic materials in RF and microwave applications. We reviewed the history and development of both technologies, introduced several types of the AM techniques and the ferrite microwave devices. We also addressed their advantages and challenges when applied to RF devices.

For additive manufacturing technology, we would like to propose new design for microwave devices by utilizing the expanded printing capabilities and extra design freedom through combining two or more additive manufacturing and other low cost techniques, thus a cheap, robust, and compact RF components can be realized. For the magnetic materials, we are targeting the fabricating and characterizing of thicker magnetic films and proposing new design of miniaturized, reconfigurable RF devices by combining the magnetic materials with the additive manufacturing technology.

CHAPTER 3

RF DEVICES USING ADDITIVE MANUFACTURING TECHNOLOGY

In this chapter, we profiled a number of RF devices designed and fabricated using additive manufacturing technology with one and two 3D printing techniques to achieve comparable performance with traditional counterparts but lower fabrication cost. Also, by incorporating with other low cost techniques, we are able to improve the RF performance and get reconfigurability for certain devices.

3.1 Ultra-low loss lowpass filter using improved air substrate

We know that RF circuits such as filters, antennas fabricated on regular dielectric PCB boards suffer from dielectric loss, which will cause series associated problems, such as the reduced overall quality factor, higher insertion loss, and degraded antenna efficiency. One of the effective ways to address such problems is by suspending the planar circuits above the ground plane such that the circuits can be treated fabricated on top of an air substrate. Due to the ultra-low loss of this air substrate, the aforementioned problems can be alleviated by minimizing the dielectric loss. AM technology offers the great flexibility for achieving such air substrate since it can directly print out the fixtures from the design concept that is normally hard or costly to achieve using conventional techniques. For example, one of the recent strategies involves printing the cavity or well-like substrate structure using dielectric, for example plastic, and metalizing the inner walls afterwards, then the circuits pattern is 3D printed in a trench manner on another piece of planar dielectric boards, such that the pattern is “etched” out on it. The circuits pattern is metalized using sputtering and an electroplating process. Finally, these two pieces are snapped together using a lego-like self-alignment structure face to face to form the air substrate.

However, in such configurations, three issues may hinder the final performance of the circuits. First, the effective dielectric loss tangent is still partially affected by the top dielectric piece where the circuit pattern is "etched" onto. Especially when the top dielectric piece occupies a greater portion of the air substrate, the effective loss tangent is deviated from zero, but close to that of the dielectric piece; and the effective dielectric constant is close to that of the top dielectric piece instead of unity. Higher dielectric loss tangent will increase the loss, while the effective dielectric constant deviating from unity will make the circuit design less accurate, otherwise additional characterization process of the air substrate needs to be performed. Secondly, the metalization process may cause warpage of both the bottom and top dielectric pieces which will cause the thickness of the air substrate to be non-uniform, which will negatively affect the wave propagation characteristics within the air substrate. For example, for a simple microstrip transmission line, the non-uniform air substrate will cause mismatch of the line since the characteristic impedance of the transmission line is related to the substrate thickness. Third, from a practical point of view, very fine finishes of both dielectric pieces have to be achieved in order to reduce the surface resistance on the metal parts, i.e., the ground plane and the circuits pattern. Nevertheless, it would still be less comparable to the quality of the regular PCB board in terms of the surface roughness.

Therefore, we proposed a new design using both AM technology and thin membrane process. Basically, a very thin layer of LCP substrate is suspended on top of the metalized cavity ground plane to form the air substrate. Because the LCP is very thin, typically as thin as 1 mil, the effective dielectric loss tangent is very close to zero, and the effective dielectric constant creates a very close unity. Due to this improvement, we can ensure the actual fabricated circuit performance is as close as possible to the designed one as we assume the effective dielectric constant of the air substrate is unity. Also, the circuits pattern can be easily etched out on the LCP substrate using standard photolithography process without worrying about the surface roughness issue encountered during the 3D printing process. Additionally, the engineered coefficient of thermal expansion (CTE) of LCP substrate is the same as copper, the fabricated circuits can have better heat and power handling capabilities when compared to the "etched" pattern on the dielectric boards which generally have different CTE from copper.

3.1.1 Low pass filter design

A common method to realize high frequency low pass filters are stepped-impedances using microstrip transmission line structures [5]. Here a five element maximally flat low-pass filter design with a cutoff frequency of 3 GHz, impedance of 50 Ω, and 35 dB of insertion loss at 4 GHz was designed using the stepped-impedance design procedure. Finite-element method (FEM), with the aid of ANSYS HFSS (High Frequency Structure Simulator), was used to optimize the design layout of the complete structure. Figure 3.1 shows the schematic of top view of the filter implemented using the stepped impedance design. The dimensions of various microstrip lines used for designing the filter are shown in Table 3.1. For the foil, thin LCP, from Rogers Corporation, with a thickness of 0.1 mm and copper thickness of 18 μm was used. Air cavity thickness between the ground conductor and the LCP layer is 1.524 mm. This configuration provides an effective dielectric constant value of 1.06. Holes in the LCP layer are also introduced to achieve alignment between the different layers during assembly. The filter is connected to 50 Ω transmission lines and in turn to coaxial cables at the input and output ports. These were included in the simulations.

Table 3.1: Design parameters of the Lowpass filter.

Parameter	A	B	C	D	E	F
mm	68.87	0.96	3.83	14.83	55.07	115.62

3.1.2 Fabrication process

Figure 3.2 shows the schematic of the low-pass filter implemented using a combination of thin-film process and 3D printing. The top supporting structure (I) and cavity for ground plane (III) are fabricated using a 3D printer; the filter was patterned on LCP with no ground

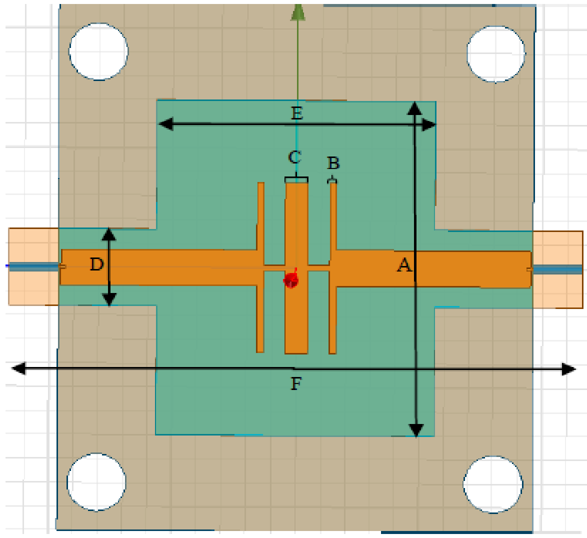

Figure 3.1: Layout of the lowpass filter design

plane (II) using standard optical lithography. The structures were stacked together to form a filter as shown in Figure 3.3. The spacer in the 3D printed cavity (III) creates an air gap between the LCP and the ground plane. All 3D printed components are printed using a professional-grade commercially available 3D printer (Objet Connex350) using a photo-polymer resin. The material used here for 3D printing is called verowhite which has a dielectric constant $\epsilon_r = 2.8$ at the frequency of interest and a loss tangent ($\tan\delta$) of 0.04. After 3D printing the top and the bottom layers, both were blanket coated on one side. First a 50 nm of Titanium (Ti) is sputtered followed by a 1 µm thick copper (Cu) layer. Ti is used here to promote adhesion between the verowhite and the copper. The low pass filter is patterned on a thin LCP (Roger 3850) substrate using standard lithography process. LCP is used here as a supporting material and thus Cu on back side (ground plane) has to be removed. First a thin layer of positive resist S1813 is coated on LCP followed by UV exposure and development. Then, Cu is selectively etched using sodium persulphate : water (1:4) solution at 40^o C. During this etching process, copper on the back side of LCP is also etched. A CO_2 laser is then used to open alignment holes in order to assemble the filter structure. For opening of the holes using the laser, holes in the Cu layer were simultaneously patterned during etching of the filter structure. Copper acts as the shadow mask for the laser to etch through the LCP layer.

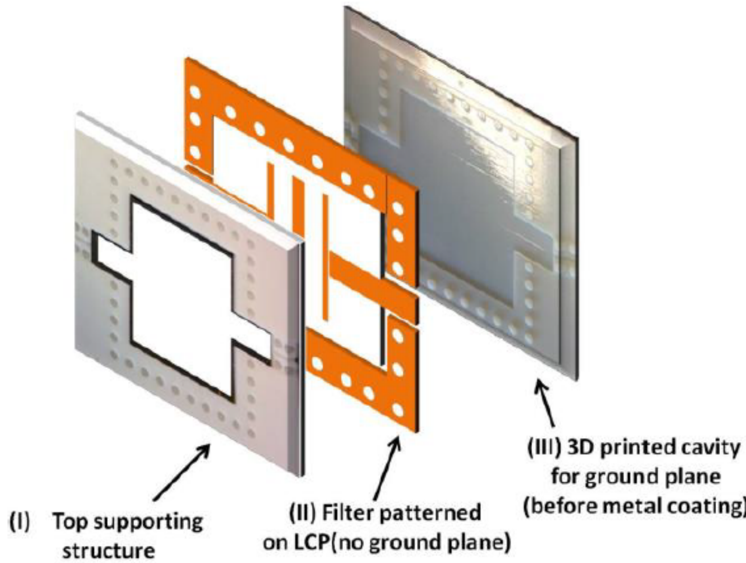

Figure 3.2: Schematic of low-pass filter implemented using combination of thin-film process and 3D printing

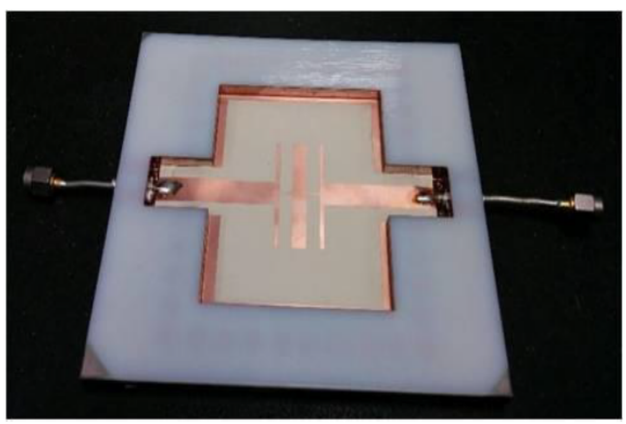

Figure 3.3: Final assembled filter with all three layers combined together in a Lego-like approach

3.1.3 Measurement results

Measurements for the transmission and reflection coefficients were done using an Agilent N5227A PNA network analyzer. Figures 3.4 and 3.5 show the simulated and measured results for reflection (S_{11}) and transmission (S_{21}) ratios, respectively. The measured results match closely over a wide frequency range. Measured isolation of 32 dB is achieved at 4 GHz as opposed to design value of 35 dB. There is a small difference in cutoff frequency which can be contributed to some discrepancy in the fabricated cavity size. The gap between the LCP and the ground plane is slightly lower than the designed value. In addition, the extra loss in the measured results as opposed to simulations can be attributed to loss from the electrically conductive silver adhesive used for connecting coax cable connectors. Overall the filter performs well and shows equivalent or better characteristics than some of the previously demonstrated LPF using other technologies to obtain low-loss substrates [6][7].

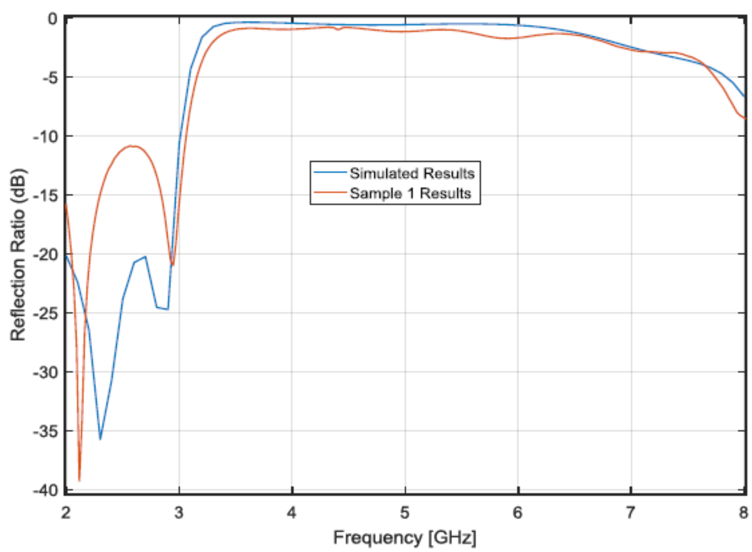

Figure 3.4: Simulated and measured reflection ratio (S_{11}) for low pass filter

3.1.4 Conclusion

Taking advantage of additive manufacturing and thin film process, a new air substrate filter is demonstrated. The filter provides low-loss performance and ease to manufacture. Simulation and measured results match closely. Slight loss in the measured results is noticed which is largely due to the attachment of coax based connector using electrically conductive silver adhesive. This technique allows the fabrication of novel RF structures that would be difficult to realize using conventional fabrication approaches.

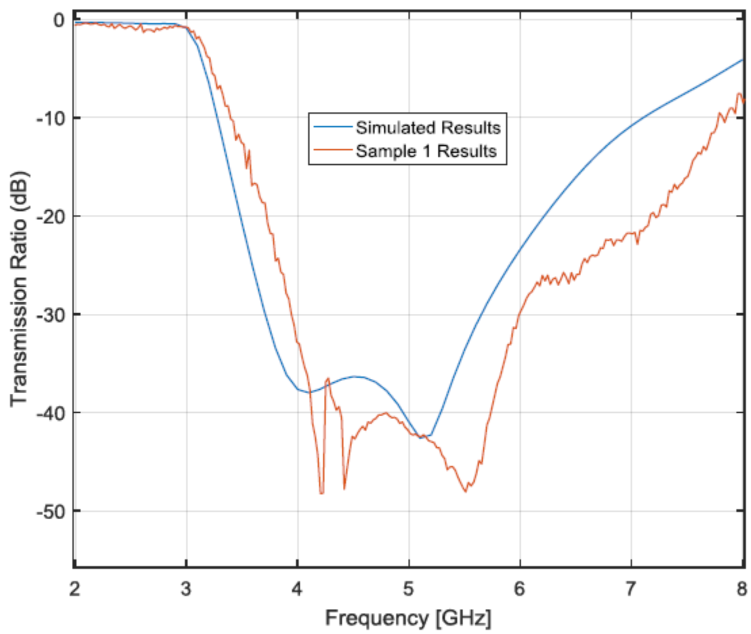

Figure 3.5: Simulated and measured reflection ratio (S_{21}) for low pass filter

3.2 Lego-like reconfigurable X-band cavity resonator

Traditional microwave waveguides as well as the cavity resonators are bulky and heavy since they are made of thick metal (brass), and are especially expensive to build. In [8] an X-band high Q rectangular resonator was built using a commercially available 3D Polyjet printer called Object Eden 250, in which the feature resolution was improved to be 16 μm per layer and the surface roughness is measured to be 0.5 μm $\pm$ 0.1 μm. The measured resonator with 0.3% frequency shift yielded a quality factor of 214 at 10.26 GHz, indicating a good implementation of low loss and low cost RF devices using polyjet printing.

Here we demonstrate a low cost, low loss, lightweight reconfigurable cavity resonator by utilizing the 3D Polyjet printing technique in combination with a novel lego-like assembling process and tuning posts structure. The cavity is achieved by assembling two 3D Polyjet printed half sections through a simple lego-like process to achieve a good alignment when assembled. The specially designed structure on the cavity allows the 6 lego-like posts to perturb the field inside the resonator, thus tuning the resonant frequency. Furthermore, the conductive silver paste is applied at the edges to help mechanically seal the cavity.

The simulation of the cavity resonator was carried out using ANSYS HFSS. The details of the cavity design, its fabrication and its experimental characterization are presented in this section.

3.2.1 Reconfigurable rectangular cavity resonator design

A X-band rectangular cavity resonator is designed to operate at the TE_{101} dominant mode. The corresponding resonant frequency is determined by [5]:

$$f_{TE_{101}} = \frac{c}{2\pi\sqrt{\mu_r \epsilon_r}} \sqrt{\left(\frac{m\pi}{a}\right)^2 + \left(\frac{n\pi}{b}\right)^2 + \left(\frac{l\pi}{d}\right)^2} \tag{3.1}$$

where ϵ_r and μ_r are the relative permittivity and the relative permeability, respectively. Here, $\mu_r = \epsilon_r = 1$ since the cavity is filled with air. The mode indices of TE_{101} mode are $m = l = 1$, and $n = 0$. $a = 20$ mm, $b = 10$ mm, and $d = 40$ mm are the width, height and length of the cavity correspondingly. Therefore the fundamental resonant frequency can be calculated as 8.39 GHz. Also, the theoretical total unloaded quality factor $Q_{0\text{-}theo}$ is given as

$$\frac{1}{Q_{0\text{-}theo}} = \frac{1}{Q_c} + \frac{1}{Q_d} \tag{3.2}$$

where Q_c and Q_d are the unloaded Q's of the cavity with lossy conducting walls and a lossy dielectric filling, respectively. By [5], both Q_c and Q_d can be found as

$$Q_c = \frac{(kad)^3 b\eta}{2\pi^2 R_s} \frac{1}{(2l^2a^3b + 2bd^3 + l^2a^3d + ad^3)} \tag{3.3}$$

and

$$Q_d = \frac{1}{tan\delta} \tag{3.4}$$

Since the cavity is filled with air, which can be treated as lossless, thus $1/Q_d = tan\delta = 0$. Assuming the cavity walls are metalized using copper, whose conductivity is $\sigma = 5.813 \times 10^7 S/m$, and the permeability of the air is $\mu_0 = 4\pi \times 10^{-7}\, H/m$, then we can determine the surface resistance R_s to be

$$R_s = \sqrt{\frac{\pi f_{TE_{101}} \mu_0}{\sigma}} = 0.0239\,\Omega \tag{3.5}$$

Note the permittivity of the air is $\epsilon_0 = 1/(36\pi) \times 10^{-9} F/m$, hence the wave number k and the wave impedance η in (3) can be easily calculated as

$$k = 2\pi f_{TE_{101}} \sqrt{\mu_0 \epsilon_0} = 175.6204 \tag{3.6}$$

and

$$\eta = \sqrt{\frac{\mu_0}{\epsilon_0}} = 120\pi\,\Omega \tag{3.7}$$

Therefore, by plugging (3.5), (3.6) and (3.7) in (3.3), and setting a = 20 mm, b = 10 mm, d = 40 mm and $l = 1$, we can finally calculate $Q_c = 7301$. Recall that $1/Q_d = 0$, thus the theoretical total unloaded quality factor of the caity is $Q_{0\text{-}theo} = Q_c = 7301$.

To excite and detect the TE_{101} mode inside the cavity, two coaxial cables with characteristic impedance of 50 Ω are used to electrically couple energy. For the purpose of maximizing the energy transfer, the feed probes of the coaxial cable should be parallel to the electric field lines of the excited mode. The feed position should be near the maximum of the electric field which in this case is $\lambda_g/4$, where λ_g is the guided wavelength. But for better impedance matching, such position can be slightly varied. Finite-element method (FEM) with the aid of ANSYS High Frequency Structure Simulator (HFSS), was used to optimize the feed positions as well as the probe length of the coaxial cable inside the cavity. The detailed parameters are provided in Table 3.2. Figure 3.6 shows the simulated electric field of the TE_{101} mode excited by the coaxial cables given the optimized feed positions and probe length.

Table 3.2: Design parameters of the cavity resonator

Dimensions (mm)			
a	20	b	10
d	40	T	10
Feed_lo	7.1	Post_d	1.46
Base_d	2.78	hCu	0.003

To perturb the field inside the cavity resonator, either the approach of material perturbations or shape perturbations is commonly used. Here we utilize the shape perturbation method by using the lego-like metal posts, so that the resonant frequency can be tuned.

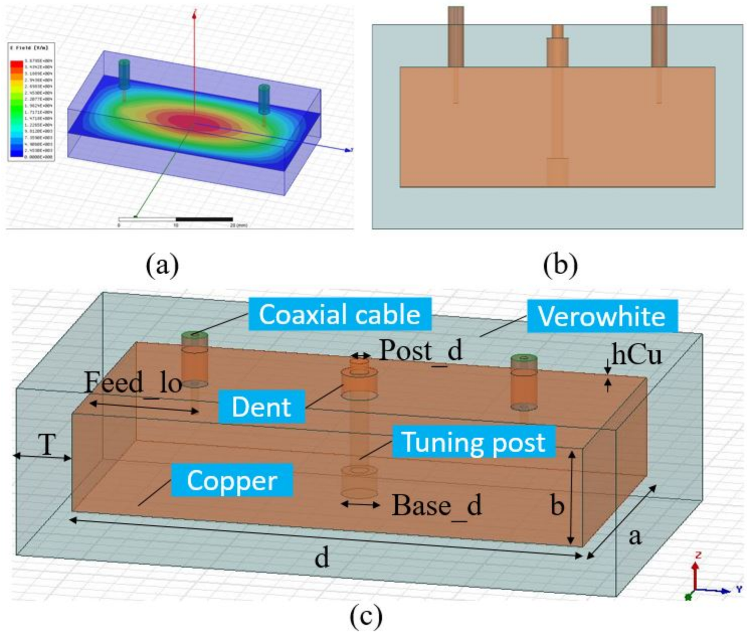

Figure 3.6: (a).Simulated electric field of the dominant TE_{101} mode; (b).Cross-sectional view of the cavity; (c). Schematic view of the cavity.

Various positions of the tuning posts will result in different resonant frequency shifts. A total of 6 tuning posts are used. Therefore, when one of the posts is pushed into the cavity to perturb the field, other posts are pulled up to prevent perturbation. In order to make a good contact between the tuning post and the cavity wall, the base of the tuning post is made larger in diameter than that of the post. However, such base requires a same size dent at the top of the cavity wall, so that when one post is pulled up not to perturb the field, the base will merge into the top cavity wall to restore its flatness. Otherwise, the resonant frequency shift will be created by not only the tuning post, but also the bases of the 5 posts sticking out into the cavity. The schematic view and detailed design parameters are shown in Figure 3.6(c) and Table 3.2.

3.2.2 Fabrication process

The 3D Polyjet printer used here is a professional-grade commercially available printer, Objet Connex 350 that uses a photo-polymer resin. It provides a fine feature resolution as well as high quality surface finish with rapid prototyping. The material used here for printing is called "VeroWhitePlus" with a relative permittivity ϵ_r of about 2.8 and a loss tangent tanδ of 0.04. The fabrication process is clean and cost-effective, combined with a high accuracy resolution, making the 3D Polyjet printing techniques suitable for the fabrication of RF circuits.

The cavity cap and base were printed by the 3D Polyjet printer. A layer of 50 nm Titanium (Ti) is sputtered first followed by another layer of 1 μm thick copper (Cu). Ti is used to promote adhesion between the VeroWhitePlus and the copper. The two cavity pieces are also electroplated with copper to increase the coverage and the metal thickness to approximately 6 μm. Figure 3.7 shows the assembling process of the cavity resonator with 6 tuning posts. First, the 6 tuning posts are assembled through the holes on the cavity cap, then the cavity cap stacks on top of the cavity base through the lego-like process. To help better seal the cavity and make a good contact between the coaxial cable and cavity wall, silver paste is applied to the four side walls of the cavity as well as around the coaxial cables, and about 4 - 5 hours is needed for the silver paste to dry and become conductive. Fig. 3.8(a) shows the cavity resonator fed by two coaxial cables and with all 6 tuning posts pulled up (no perturbations). Fig. 3.8(b) shows the cavity with one tuning post pushed into the cavity to perturb the field inside the resonator.

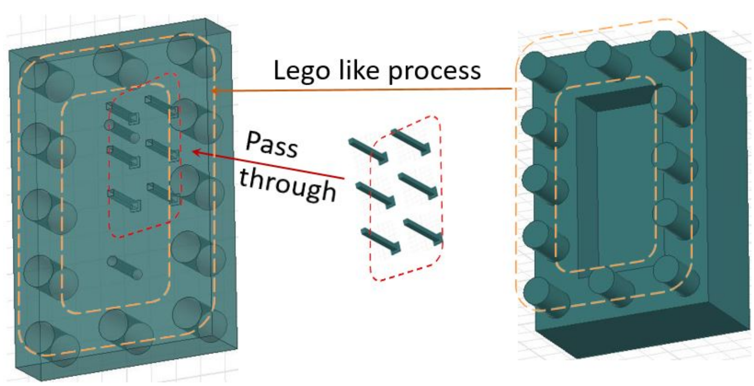

Figure 3.7: The assembling process of the cavity resonator

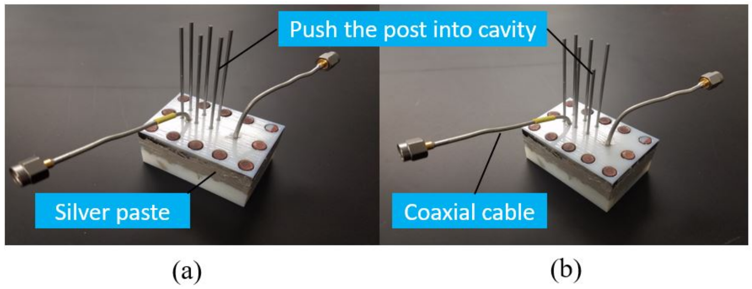

Figure 3.8: (a) All the 6 posts are pulled up (no perturbation); (b) The center post is pushed into the cavity to perturb the field.

3.2.3 Bi-material printed quasi yagi-uda antenna

All EM-simulations were performed using Ansys HFSS. The measurement was carried out using a Keysight N5227A Performance Network Analyzer from 8 - 10.3 GHz. An SOLT calibration was performed up to the edge of the coaxial cable connectors, and all measurements are carried out at room temperature.

The measured and simulated results are shown in Fig. 4. The simulated unperturbed dominant resonant frequency of the TE_{101} mode is 8.32 GHz, which is a little bit different from the 8.39 GHz calculated from (3.1). That is because the probes of the coaxial cables themselves also inevitably serve as a perturbation of the field. From Fig. 4, it can been seen that the measured unperturbed dominant frequency is 8.31 GHz, which is 0.1% of frequency shift relative to the simulated one. This small difference is due to fabrication tolerance. Additionally, we can see the measured frequency tuning range is from 8.31 GHz - 10.12 GHz, which gives 1.81 GHz of tuning bandwidth.

By observing the unperturbed resonant frequency f_{r_0} = 8.31 GHz and the 3 dB bandwidth Δf_{3dB} = 0.04 GHz from Fig. 4, the loaded quality factor Q_L can be calculated as:

$$Q_L = \frac{f_{r_0}}{\Delta f_{3dB}} \approx 208 \tag{3.8}$$

The external quality factor Q_e as well as the unloaded quality factor Q_0 can be respectively determined by:

$$S_{21}(dB) = 20log_{10}\frac{Q_L}{Q_e} \tag{3.9}$$

and

$$\frac{1}{Q_0} = \frac{1}{Q_L} - \frac{1}{Q_e} \tag{3.10}$$

From Figure 3.9, $S_{21}(f_{r_0}) =$ -10.68 dB, thus the unloaded quality factor can be calculated as $Q_0 = 391$. However, it is relatively lower than the simulated one. Also, except no obvious peak was observed in the measured "P1" curve, all the other 5 measured curves show the corresponding tuned resonant frequencies which agree very well with the simulation. The differences between the simulated and measured results are due to the following reasons: (a). The weak coupling between the two coaxial cables during the measurement, (b). The two VeroWhitePlus cavity pieces were not polished after they were printed (certain surface roughness exists, ~5 μm, that was not included in the simulation); thus, surface roughness increases loss, (c). There are fabrication tolerances both for the cavity and the posts, (d). The conductivity of the silver paste is not as good as that of metal at these freqencies. Deembedding the data up to the front end of the coaxial cables will be carried out in the future. Table 3.3 lists all the simulated and measured tuned resonant frequencies by pushing one tuning post into the cavity each time, which shows a very close matching between the simulation and measurement. The average unloaded quality factor is calculated to be 169, and the average frequency shift is 1.05%. Furthermore, the simulated unperturbed unloaded cavity quality factor is 3418 assuming perfectly smooth walls. However, if one considers the average measured surface roughness of 5μm, then the simulated unperturbed quality factor reduces to 3351. The lower measured values can be attributed to the overall waviness of the printed material, as well as the lossy nature of the silver epoxy used to seal the two cavity pieces. The overall result demonstrates a good combination of 3D Polyjet printing techniques and the novel RF circuits.

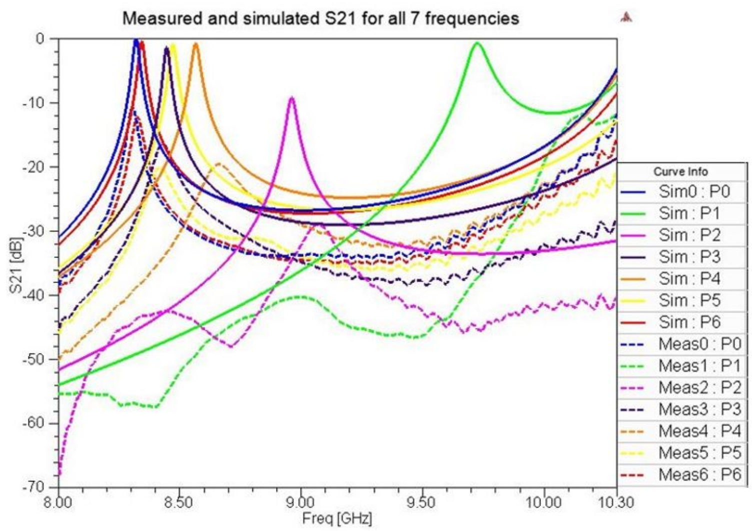

Figure 3.9: Measured and simulated S_{21} for all 7 frequencies

Table 3.3: The measured unloaded qualify factor Q_L, simulated and measured tuned frequencies (exclude P2, and Po is the unperturbed resonant frequency)

Metrics	**P0**	**P1**	**P2**
Sim/Meas freqs (GHz)	8.32/8.31	9.72/10.12	8.96/9.06
Measured Unload Q_0	391	91	72
Metrics	**P3**	**P4**	**P5**
Sim/Meas freqs (GHz)	8.45/8.43	8.57/8.66	8.47/8.42
Measured Unload Q_0	132	111	107
Metrics	**P6**		
Sim/Meas freqs (GHz)	8.34/8.33		
Measured Unload Q_0	276		

3.2.4 Conclusion

This section presents a combination of lego-like tuning posts and a cavity resonator structure using 3D Polyjet printing techniques. The fabricated X-band reconfigurable cavity resonator shows the dominant resonant frequency of 8.31 GHz with 0.1% frequency shift and an unload qualify factor of 391. By using the tuning posts, the field inside the cavity is effectively perturbed resulting in 1.81 GHz of tuning bandwidth. These results provide an avenue for fabricating low cost and good performance RF components using the 3D Polyjet printing techniques. Further performance improvement can be achieved by addressing the substrate waviness and roughness issue, as well as using sealing materials with higher conductivity.

3.3 A Bi-material fully aerosol jet printed W-band quasi-yagi-uda antenna

The planar quasi-Yagi-Uda antenna is chosen to achieve the end-fire radiation pattern because of its merits of high gain, low profile and compatibility with the standard IC fabrication. The design of the antenna was based on the standard cylindrical-wire element Yagi-Uda antenna in air which features one reflector, one driver and two directors. The initial dimensions were first obtained for maximum directivity and then were scaled to the designed dimensions on the polyimide substrate [9]. Given that the dielectric constant of the polyimide is $\epsilon_r = 3.5$ [10], we can determine the effective dielectric constant of the air-polyimide media to be $\epsilon_{eff} = 2.6$ which yields the dimension scaling factor to be $1/\sqrt{2.6} = 0.62$. The equivalent widths of the microstrip elements were also obtained by mapping from the diameter of the cylindrical-wire elements.

3.3.1 Antenna design

Figure 3.10 shows the schematic of the antenna, in which the ground plane was utilized as the pseudo reflector instead of adding an independent reflector element. The two dipole arms are separately Aerosol Jet printed on both sides of the polyimide substrate, and are connected to the microstrip line and the ground plane, respectively, such that the dipole is directly fed by the microstrip line. Thus, the traditionally used microstrip balun for feeding the dipole is avoided. In particular, given the high antenna input impedance at the driver element, a quarter wavelength transformer is designed to match with the 50 Ω microstrip line. Moreover, a vialess Coplanar Waveguide (CPW) to microstrip transition is designed as part of the feeding network for W-band probing, as can be seen in Fig. 1.

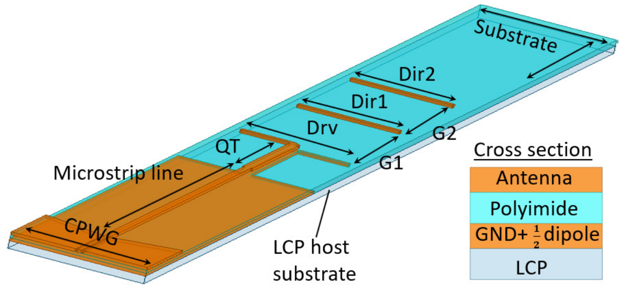

Figure 3.10: The design schematic of the W band antenna. All metal layers and the dielectric substrate are Aerosol Jet printed

3.3.2 Fabrication Process

Compared to the traditional photolithography in which the antenna pattern is etched out of the copper cladding sheet, the Aerosol Jet printing technology utilizes the atomized liquid material, such as silver ink or polyimide dielectric, to directly print the pattern on the substrate, offering a more economic, green and rapid fabrication process. The basic illustration of the Aerosol Jet printing process is shown in Figure 3.11. First the liquid material is atomized to create dense aerosol droplets with diameter between 1-5 μm; then the aerosol is transported using an inert gas to the deposition head where the aerosol is focused by an annular sheath gas, creating the jetted aerosol material. The feature resolution of the Aerosol Jet ranges from 5 μm to 1 mm depending on the size of the nozzle, the amount of the feeding material, and the sheath gas pressure.

Here we use the commercially available Optomec Aerosol Jet 5X printer. Its 5 axes degree of motion freedom allows for printing electronics onto complex 3D surfaces. The printing preparations begin by generating the CAD toolpath file by specifying the trace pattern, trace width, and the trace overlapping percentage for sufficient coverage. A 4 mil Rogers 3850 HT LCP host substrate was cleaned with alcohol after removing the copper cladding. For maximum dimension accuracy while considering shortening the printing cycle, the 100 μm nozzle was used to print the top antenna layer since the elements dimensions are crucial to the antenna performance. Whereas the ground plane with one driver arm and the polyimide substrate were printed using the 150 μm and 300 μm nozzles, respectively, since

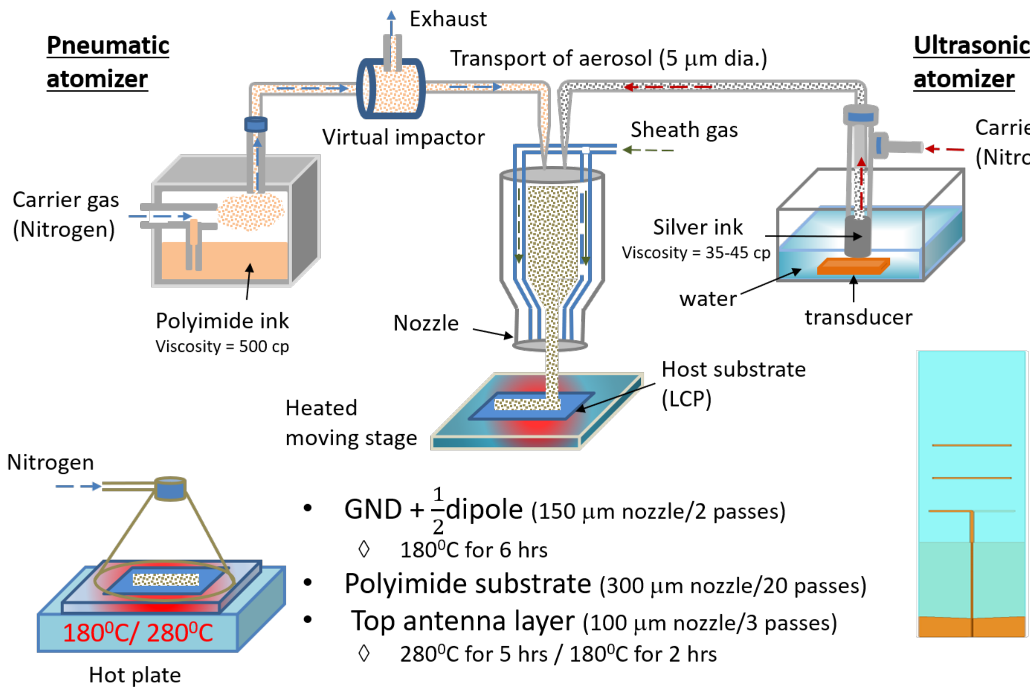

Figure 3.11: The illustration of the Aerosol Jet printing process

less accuracy is required and certain thickness needs to be achieved quickly. In addition, the printer parameters, such as the amount of feeding material and the sheath gas pressure, were also adjusted to obtain the same trace width as specified in the toolpath. After the preparation, the host substrate was loaded onto the stage for printing. Note that the desired metal or polyimide thickness was achieved through stacking multiple layers. Particularly, 2 layers of silver ink were first printed on the LCP forming the ground plane with one driver arm, which was then cured on the hot plate in nitrogen under 180^oC for 6 hours to sinter the silver nanoparticles, resulting in the measured ground plane thickness of about 3 μm. Next, the polyimide substrate and the antenna elements were sequentially printed above the ground plane. Specifically, 20 layers of polyimide and 6 layers of the silver ink were printed using the aforementioned different nozzles respectively. As a result, the polyimide substrate was sandwiched in between the ground plane and the antenna layer. Finally, the whole sample was cured in nitrogen under 280^oC for 5 hours to solidify the polyimide and a subsequent 180^oC for 2 hours to sinter the silver nanoparticles of the antenna layer. Figure 3.12 shows the printed antenna sample under the microscope and the measured surface profile of the polyimide substrate. As can be seen, the surface roughness of the polyimide is about 0.5 μm and the average substrate thickness is about 22 μm. The slope of the surface profile curve is due to the fact that the sample was placed on the non-horizontal plane right after the printing, causing the uncured polyimide to flow to one side.

Compared to fabricating the substrate using the polyjet technology, three major advantages of using AJP technology with the polyimide are highlighted: (a) the polyimide substrate is smoother and remains in shape, as opposed to the "potato-chipped" polymer substrate, after the curing process; (b) the polyimide substrate can be as thin as several micrometers whereas the polymer substrate is limited to $\geq$100 μm; (c) the loss tangent of the polyimide substrate is significantly less than that of the polymer substrate, making it better for W-band and high frequency circuits and components.

3.3.3 Measurement setup and results

In order to justify the printing quality, the printed dimensions were measured under the microscope and compared with the designed values, as shown in Table 3.4. We can see that the dimensions of the printed key antenna features are almost exactly the same as the designed values, and the maximum percentage difference between the measured and designed dimensions is 3% indicating a highly accurate fabrication process using the AJP technology. Due to the small antenna size, the four-point conductivity measurement of the silver ink was not performed. Under the curing process specified in previous section, the printed silver can achieve 40% of the bulk conductivity of the solid silver.

The return loss of the antenna sample was measured using the Cascade Industry 150 μm pitch G-S-G waveguide Infinity probe on a MPI TS150-THZ on-wafer probe station utilizing a Keysight N5227A Performance Network Analyzer, which was calibrated with the LRRM method up to the probe tips from 75 - 110 GHz. The full-wave simulations were carried out using ANSYS HFSS. Figure 3.13 compares the measured and simulated

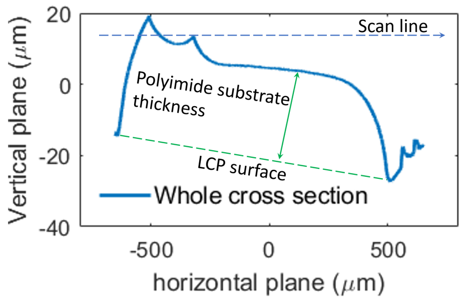

(a)

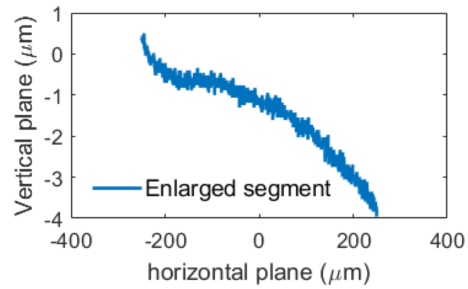

(b)

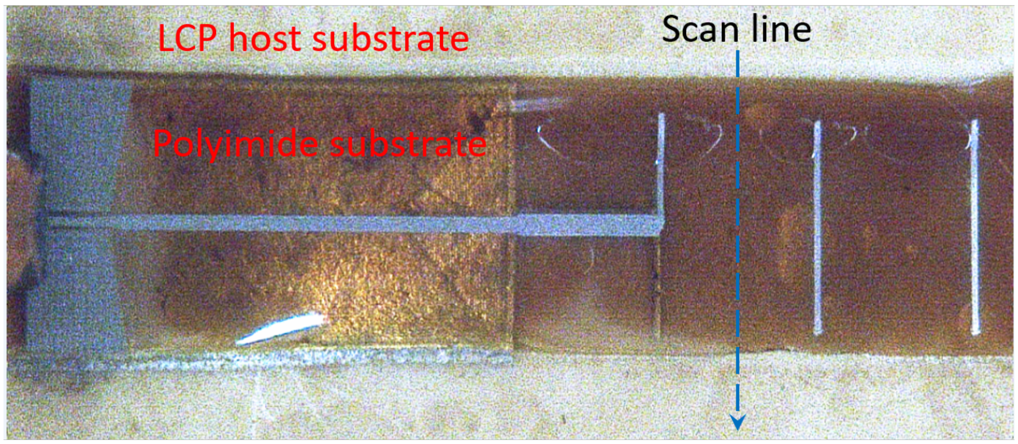

(c)

Figure 3.12: (a) The surface profile of the whole polyimide cross section (b) The enlarged segment of the polyimide cross section (c) The top view of the printed quasi-Yagi-Uda antenna

S_{11}, from which we can see that a good agreement is achieved. Specifically, the measured resonant frequency is 92.7 GHz with 20 dB of return loss, whereas the simulated return loss at 94 GHz is 31.6 dB given the conductivity of the printed silver is 40% of the solid silver. Furthermore, the measured and simulated 10 dB impedance bandwidth is 12.5 GHz and 8.1 GHz, respectively. Wider measured impedance bandwidth can be attributed to the tradeoff between the radiation efficiency and the impedance matching. The far field radiation was not measured due to the equipment limitations; as a reference, the simulated radiation pattern as well as the realized gain versus frequency are provided in Figure 3.13. As shown in Figure 3.14, with 40% of the bulk conductivity for the printed silver, the simulated maximum realized gain is 7.65 dBi at 94 GHz and the 3 dB gain bandwidth is 9 GHz, suggesting that a good end-fire radiation with decent gain is obtained from this design.

Table 3.4: The measured and designed dimensions of the key features of the 94 GHz Quasi-Yagi-Uda antenna

Features	Dimensions (mm)	
	Designed	Measured
Substrate	1.3 (W) × 7.7 (L) × 0.023 (H)	1.3 (W) × 7.6 (L) × 0.022 (H)
Dir 1, Dir 2	0.03 × 0.96	0.03 × 0.95
Drv	0.03 × 1.02	0.03 × 1.01
G1, G2	0.88	0.87
Microstrip	0.065 × 2.2	0.063 × 2.1
QT	0.09 × 0.78	0.09 × 0.78
CPWG	0.015 (G), 0.04 (S) 0.45(L)	0.015, 0.04 0.44
Max diff. %	3 %	

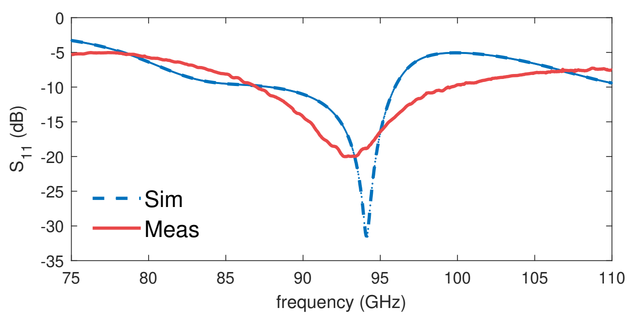

Figure 3.13: The simulated and measured S_{11} of the printed quasi-Yagi-Uda antenna

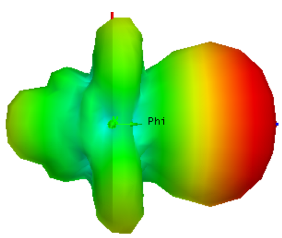

(a)

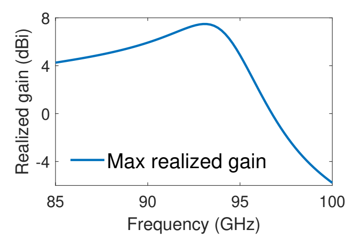

(b)

Figure 3.14: (a) The simulated 3D far field radiation pattern at 94 GHz (b) The simulated maximum realized gain V.S. frequency

3.3.4 Conclusion

This work demonstrates for the first time a bi-material, fully Aerosol Jet printed W-band quasi-Yagi-Uda antenna operating at 94 GHz. A 4 mil LCP served as the host substrate, where silver ink nanoparticles were used to print the ground plane and the top metal antenna layer with the same thickness of 3 μm, and polyimide materials were deposited to form the 22 μm dielectric substrate. Various nozzle sizes were utilized for high quality geometry resolution and fast prototyping. The measured S_{11} matches well with the simulation results, suggesting a successfully fabricated antenna and paving the way for fabricating RF circuits and components in W-band or even higher frequencies band fully using the AJP technology. Future works involve improving the surface quality and the silver ink conductivity, as well as measuring the antenna gain.

3.4 Aerosol jet printed 24 GHz quasi-yagi-uda antenna on a poly-jet printed cavity substrate

The purpose of this section is to demonstrate a low loss, high gain and good efficiency quasi-Yagi-Uda antenna by utilizing the Aerosol Jet printing technology and 3D Polyjet printing technique. The substrate is printed by the commercially available 3D printer using VeroWhitePlus material, and the antenna structure is mostly printed using silver ink. Full EM wave simulation was carried out using ANSYS HFSS. The details of the antenna design, fabrication process and the measurement results are presented.

3.4.1 The antenna design

Similar to the quasi-yagi-uda antenna shown in the previous section, two directors are used here. But here to feed the antenna properly, a microstrip balun is used to convert the signal carried by the transmission line into two equal magnitude but opposite polarity (180° phase shift) signals that feed two arms of the driven element. Since the input impedance is largely affected by the lengths of the driven element, directors and the spacing of the directors, these parameters are intentionally optimized to match the 50 Ω microstrip transmission line. In the measurement, a 1.85 mm end-launch connector whose characteristic impedance is 50 Ω is used to connect to the microstrip line.

The antenna and the feed structure are Aerosol Jet printed on top of a 3D printed substrate fabricated with the Polyjet technology. In a traditional design, to have a relatively low loss, a localized back-side etching process is utilized to create a cavity by etching out the silicon substrate underneath the antenna, and another piece of SiO_2 is used as the support substrate for the antenna and the feed network. In this design, we take advantage of additive manufacturing technology to 3D print a single piece of substrate which integrates the cavity into the back side of the substrate, thus simplifying the fabrication process and minimizing the prototyping time. Moreover, the dielectric constant ϵ_r and loss tangent $tan\ \delta$ of the material used for printing are 2.8 and 0.04, respectively, hence providing a merit of relatively low loss compared to silicon and SiO_2. Figure 3.15 and Figure 3.16 illustrate the design schematic of the end-fire quasi Yagi-Uda antenna on the 3D printed substrate. From the figures, we can see that the total thickness of the 3D printed substrate is 300 μm. Considering the practical fabrication resolution limit as well as the mechanical stability, the distance between the top of the cavity and the surface of the substrate ("hSub-hCav") is chosen to be 150 μm. Other parameters, for example the size of the cavity ("xCav", "yCav" and "hCav"), can also affect the performance of the antenna. Particularly, the size of the cavity should not be less than the area occupied by the antenna (5 mm $\times$ 5.6 mm), otherwise the gain of the antenna will be significantly deteriorated. By taking the fabrication resolution limit into account, we performed an EM-simulation using Ansys HFSS to optimize the design parameters, and the results are reported in Table 3.5.

3.4.2 Fabrication process

Figure 3.17(a) shows the fabricated sample of the 3D printed substrate compared to a U.S. quarter coin. Note that the two vias with diameter of 1.98 mm on the substrate are for connecting the 1.85 mm end launch connector to perform measurements. First, the substrate is printed using an industrial-grade commercially available 3D printer called Object Connex 350 with a photo-polymer resin. The material used here is called "VeroWhitePlus" which

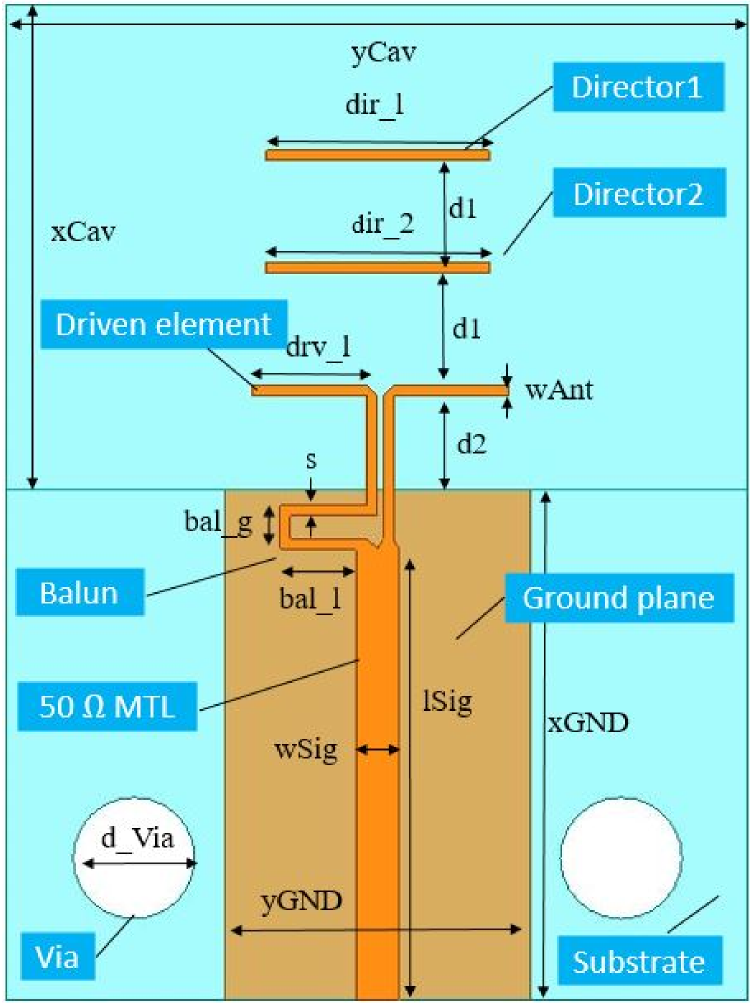

Figure 3.15: Top view of the quasi-Yagi-Uda antenna on the substrate

has a dielectric constant ϵ_r of 2.8 and a loss tangent $tan\ \delta$ of 0.04. Then a 1 μm layer of copper is sputtered on the backside of the substrate. The area of the metalized ground plane is 10 mm $\times$ 6 mm which is isolated by a 3D printed special cover.

The design pattern of the antenna as well as the feed network is first processed by AutoCAD to generate the toolpath for the Aerosol Jet printer nozzle. Then the pattern is printed on the opposite side of the 3D printed substrate where the ground plane is. By adjusting the pressure of the sheath gas flow, the width of one single toolpath is fixed at 10 μm. As illustrated in the design schematci, the width of the driven element, two directors and microstrip balun is 0.2 mm, whereas the microstrip transmission line has a width of 0.84 mm. The average thickness of the printed lines is 4 μm. Compared to the commonly used

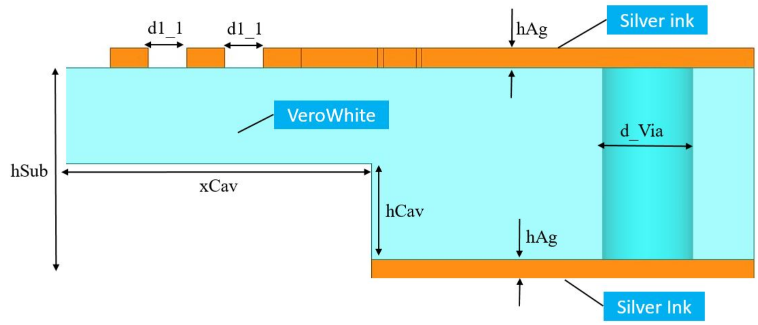

Figure 3.16: Cross-sectional view of the quasi-Yagi-Uda antenna on the substrate

Table 3.5: Quasi-Yagi-Uda Antenna Design Parameters

Dimensions (mm)			
dir_1	4.35	dir_2	4.4
drv_l	2.25	wAnt	0.2
d1	2.2	d2	1.84
xCav	9.5	yCav	14.5
bal_l	1.497	bal_g	0.85
wSig	0.84	lSig	8.656
xGND	10	yGND	6
s	0.31	d_Via	1.98
hSub	0.3	hCav	0.15
hAg	0.003		

photolithographic processes which demand a strict clean room environment, a big advantage of Aerosol Jet printing technology is that the entire process is accomplished in a single step without wasting materials and resources, hence lowering the overall cost and relaxing the environmental requirements. Finally, after the whole pattern is printed, the sample was first baked under 65 celsius for 1.5 hour, and then was cured using 1 minute of Argon and 1 minute of plasma which contains 97% of Argon and 3% of SF6. Then the silver ink can achieve a conductivity of about 10% of that of solid silver, which is calculated to be 5.13×10^6 Siemens/m. Figure 3.17 (b) shows the cured quasi-Yagi-Uda antenna sample. Note the darkened ground plane beneath the antenna is due to the curing process. Figure 3.18(a) shows the Aerosol Jet printing system as well as the process of printing the antenna on the 3D printed VeroWhitePlus substrate. Figure 3.18(b) shows the Aerosol Jet printed quasi-Yagi-Uda antenna with a 1.85 mm end launch connector.

(a) (b)

Figure 3.17: (a) 3D printed substrate compared to the U.S. quarter coin, (b) Aerosol Jet printed quasi-Yagi-Uda antenna on the VeroWhitePlus substrate after curing

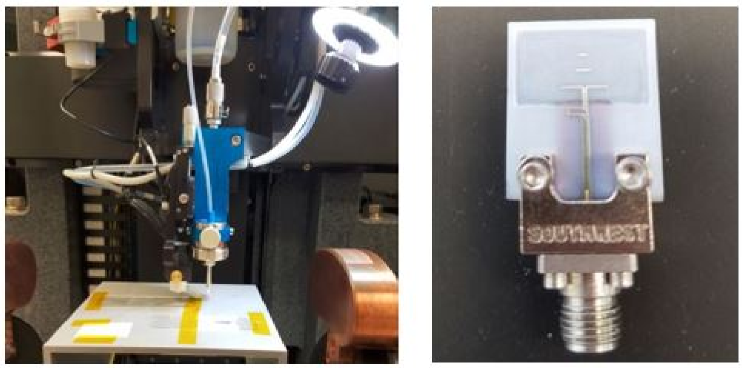

(a) (b)

Figure 3.18: (a) The Aerosol Jet printing system, (b) The quasi-Yagi-Uda antenna with a 1.85 mm end launch connector

3.4.3 Simulation and measurement results

The EM-simulation was performed using Ansys HFSS. Since the silver ink used by the Aerosol Jet achieves 10% of conductivity of the solid silver, the conductivity of the silver ink was set to be 5.13×10^6 Siemens/m in the simulation. The measurement was performed with a Keysight N5227A Performance Network Analyzer. One 1.85 mm end launch connector was used to connect to the microstrip feed line of the antenna. The measurement was calibrated with the SOL method up to the end launch connector.

Figure 3.19 compares the simulated and measured return loss over a frequency range of 20 - 30 GHz. At 24 GHz, the simulated return loss is 26.6 dB, and the measured return loss is about 37.4 dB at 26.3 GHz. The difference is due to the fabrication accuracy, since the resonance frequency is highly sensitive to the dimensions of the antenna, and the connector.

Also because of the low conductivity of the printed silver, the antenna is more lossy which give lower impedance matching. Table 3.6 provides the measured dimensions of several critical antenna parameters after the curing process. It can be seen that the length of the driven element "drv_l" reduces to 2.28 mm compared to the designed 2.45 mm, which also explains why the measured resonance frequency increases to 25.8 GHz. The simulated and measured E plane radiation patterns displayed in Figure 3.20 exhibits a good agreement. Simulated maximum realized gain versus frequency are presented in Figure 3.21. We can see that simulated the 3 dB bandwidth is more than 10 GHz. Table 3.7 provides the summary of the simulated parameters in terms of the antenna performance. We can see that there is a tradeoff between the 3 dB bandwidth and the maximum gain; wider bandwidth will result in lower maximum gain.

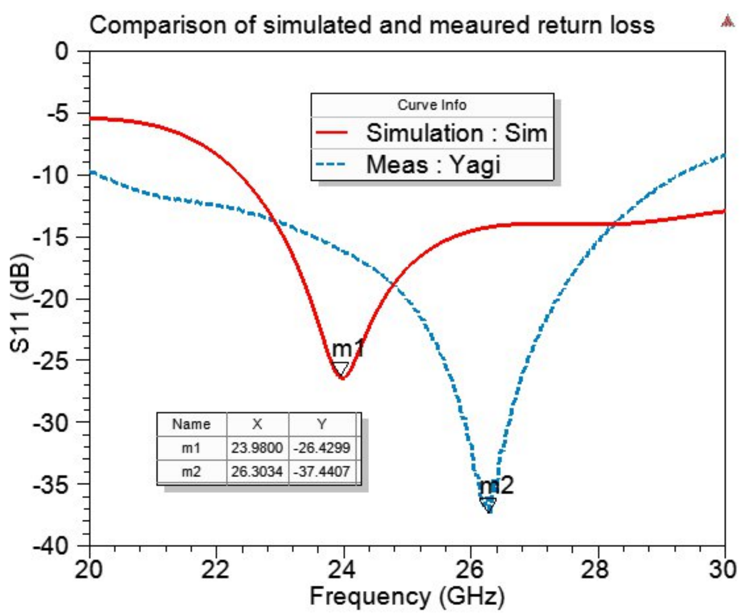

Figure 3.19: The simualted and measured return loss of the antenna fabricated by AJP and polyjet technology

3.4.4 Conclusion

In this section, a compact, low profile 24 GHz quasi-Yagi-Uda antenna was developed using additive manufacturing techniques. The antenna is optimized to be impedance matched with

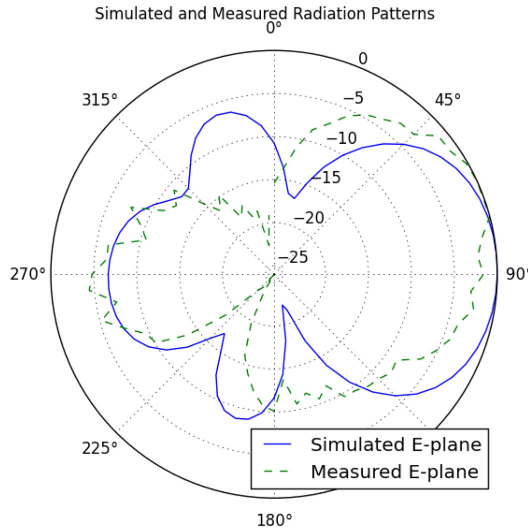

Figure 3.20: The simualted and measured E plane radiation patterns of the antenna fabricated by AJP and polyjet technology

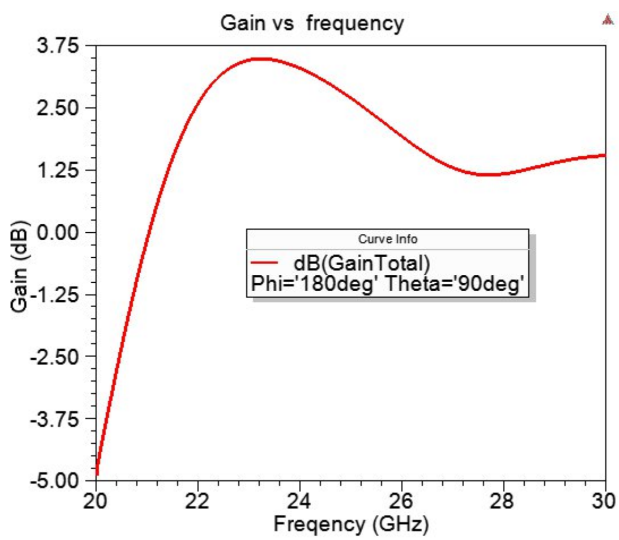

Figure 3.21: Maximum simulted realized gain versus frequency

a 50 Ω microstrip transmission line. Good return loss and end-fire radiation patterns are achieved. The simulation and the measurements match closely. Moreover, the combination of Aerosol Jet printing and Polyjet printing technologies is demonstrated for the first time at mm-wave frequencies, which facilitates low cost and fast prototyping. It shows the advantage of additive manufacturing technology that allows for highly efficient fabrication of novel RF structures.

Table 3.6: Measured quasi-Yagi-Uda Antenna Design Parameters after curing process

Dimensions (mm)			
dir1_l	4.02	dir2_l	4.03
drv_l	2.15	wAnt	0.18
d1	1.31	d2	1.63
bal_l	1.47	bal_g	0.84
wSig	0.79	lSig	8.58

Table 3.7: Quasi-Yagi-Uda Antenna Performance Parameters

Simulated performance parameters at 24 GHz	
S_{11}	26.4 dB
Maximum Gain	5.75 dBi
Radiation efficiency	47.7%
3 dB bandwidth	>10 GHz
Front-to-back ratio	4.6

3.5 Summary

In this chapter we demonstrated a number of RF devices that have very good RF performance as well as low cost. These devices are either fabricated used one 3D printing techniques but achieved reconfigurability, or printed two different materials at one single device to obtain showcase fully printed capability, or fabricated by combining two 3D printing techniques to display printing flexibility. The above results show great potential of utilizing 3D printing technologies of designing and fabricating RF circuits and devices.

CHAPTER 4
CHARACTERIZATION OF MAGNETIC NANOPARTICLE FILM

With the advent of the 5G wireless communication system, wireless applications utilizing the radio frequency (RF) and millimeter wave bands will become more widespread [11]. However, the signals generated by other nearby applications, especially occupying the same or adjacent bands, can be treated as an RF interference or jammer to the local receiver. Given the scarce bandwidth, the RF interference can get more critical which degrades the quality of service [12]. However, if such a high power jammer is above a certain power threshold, some power-sensitive electronic components in the RF front end can be adversely affected or even damaged. In many practical RF systems, the input power threshold for the low noise amplifiers (LNAs) is around 30 dBm to prevent the LNA from being damaged due to a high collector current density in the transistor [13]. Power limiters are also employed to protect the LNAs and receivers by blocking the high power interferences [14][15]. Given the narrow band nature, these high power interfering signals can still damage the components since the limiters are not frequency selective.

To track down the narrow band high power interference signals, a device called Frequency Selective Limiter (FSL) has been proposed which is able to capture and suppress the large power interference signal even if it has a very narrow bandwidth. The FSL can be achieved through many approaches such as using paramagnetic [16], parametrics [17] and switched-multiplexers [18][19]; however, these FSLs either suffer from severe distortion or require sophisticated topology and manufacturing which limits their integration capability (especially for monolithic circuits) and increases their cost. It has been reported that the magnetic ferrite materials and nanoparticles offer an intrinsic non-linear signal property that is widely explored in microwave and millimeter-wave applications. Above a critical RF power level, the non-linear spin wave excitation will cause the magnetic loss to the RF signal.

In light of this, one promising solution is the FSL utilizing the magnetic ferrite materials [20][21]. This type of FSL can selectively track down and attenuate more than one large power interference signals while maintaining the dynamic range of the signals of interest, or with little attenuation. In light of this, the FSL becomes a passive circuit without additional complicated circuitry, so that the overall size as well as the cost is greatly reduced.

Recently, FSLs using magnetic thin films or spheres have been developed with single crystal Yttrium Iron Garnet (YIG) and scandium doped Barium Hexaferrite materials [21][22][23][24]. These films or spheres are produced by using a sol-gel method which is simple and cost-effective. Nevertheless, such a method is unable to produce significant amounts of magnetic materials in a solid state configuration. For example, the achieved scandium doped Barium Hexaferrite film thickness on the alumina (99.6%, Al_2O_3) substrate is only 10 μm [23], which is too thin to show any significant FMR effect. Given the relatively large actual size, these FSLs are hard to be integrated into RF integrated circuits.

In this work, a broad range of magnetic ferrite nanoparticles has been chosen to explore their fundamental magnetic properties and the fabrication process. Particularly, Cobalt Ferrite ($CoFe_2O_4$) and Manganese Ferrite ($MnFe_2O_4$) nanoparticles are deposited on a soda-lime glass substrate to form the magnetic films with thicknesses ranging from 2.5 μm to 125 μm, which is much thicker than the 100 nm $CoFe_2O_4$ films in some reported works [25][26]. These magnetic nanoparticles show a much higher saturation magnetization than that of YIG. Two types of methods, the Layer-by-Layer (LbL) process and the Solution Cast (SC) method, are employed to fabricate the magnetic films. These methods are-to the best of our knowledge-implemented for the first time to develop relatively thick magnetic films on large area substrates without the usage of expensive vacuum deposition systems. By integrating the magnetic films with a microstrip transmission line structure, we created a basic microwave device to investigate the properties of the magnetic thin films in terms of the film thickness, types of the materials and deposition methods. A 3-D polyjet printer is used to enable the flexibility and fast prototyping to fabricate the microstrip line, as well its assemblies for measurement purposes, so the overall cost of the fabrication can be reduced.

4.1 FMR Frequency and Magnetic Susceptibility in Magnetic Nanoparticles

The unique non-linear property of the magnetic ferrite materials can be attributed to the Ferromagnetic Resonance (FMR) phenomenon, which represents the absorption capability of a magnetic material to electromagnetic waves of some frequency. The small-signal theory of FMR was developed by Kittel [67]. This intrinsic property gives rise to the use of the magnetic materials in the FSL to achieve the unique performance aforementioned.

Note that different types of magnetic materials may display distinct FMR effect, so in this work, very diverse magnetic metal oxides nanoparticles have been chosen to study the determining factors to the frequency of FMR. These nanoparticles were synthesized via aminolytic reactions with fine controls of sizes and metal ion concentrations, which included MnO, $ZnFe_2O_4$, $MnFe_2O_4$, $Zn_xMn_{1-x}Fe_2O_4$, $Gd_xMnFe_{2-x}O_4$, $Ho_xMnFe_{2-x}O_4$, $CoFe_2O_4$, $HoCoFe_{2-x}O_4$ and $NdCoFe_{2-x}O_4$ ($0 \leq x \leq 1$), as shown in Table 4.1. The exact chemical compositions of these nanoparticles are still being studied. Figure 4.1 shows the X-ray diffraction (XRD) patterns collected with a Bruker X-Ray Diffractometer over a 15^o-85^o 2θ range. Particle sizes were determined from the average peak broadening of the five strongest Bragg peaks using the commercial program IGOR and the Debye-Scherrer equation. Figure 4.2 shows the temperature dependent magnetic moment of these nanoparticles. Magnetic measurements were performed using a Quantum Design MPMS-5S SQUID magnetometer. Zero-field cooled (ZFC) susceptibility measurements were conducted under an applied field of 100 G with temperature ranging from 5 - 310 K.

Spinel ferrite nanoparticles have displayed FMR under magnetic fields. After forming nanoparticle films, the FMR peak position and profile do not display any difference from the original nanoparticles. The nanoparticles and their films have shown different FMR absorption profiles with different chemical composition as shown in Figure 4.3, which were determined under a constant excitation wavelength, $f = 9.88$ GHz. The resonance frequency increases with the increase of nanoparticle size. However, the peak width is independent of the nanoparticle size at least in the 4 - 10 nm size range that we studied. FMR spectroscopies were acquired with a Bruker EMX EPR spectrometer with a center field of 5125.0 G and a sweeping width of 9750.0 G under a resonance frequency of 9.88 GHz at room temperature.

Table 4.1: Characterization of the selected magnetic nanoparticles.

Sample names	Species	Metal substitution (mol/mol, %) from ICP-MS	Particle size (nm)
MnO_20nm	MnO	-	20
$ZnFe_2O_4$_6nm	$ZnFe_2O_4$	-	6
$CoFe_2O_4$_9nm	$CoFe_2O_4$	-	9
$CoFe_2O_4$_Ho2.8_6nm	$HoCoFe_{2-x}O_4$	Ho(III) 2.8% for M(III)	6
$CoFe_2O_4$_Ho3.3_6nm	$HoCoFe_{2-x}O_4$	Ho(III) 3.3% for M(III)	6
$CoFe_2O_4$_Ho5.9_6nm	$HoCoFe_{2-x}O_4$	Ho(III) 5.9% for M(III)	6
$CoFe_2O_4$_Nd2.5_6nm	$NdCoFe_{2-x}O_4$	Ho(III) 2.5% for M(III)	6
$CoFe_2O_4$_Nd3.5_6nm	$NdCoFe_{2-x}O_4$	Ho(III) 3.5% for M(III)	6
$MnFe_2O_4$_7nm	MnFe2O4	-	7
$MnFe_2O_4$_6nm	MnFe2O4	-	6
$MnFe_2O_4$_Gd14_6nm	$GdxMnFe_{2-x}O_4$	Gd(III) 14% for M(III)	6
$MnFe_2O_4$_Gd4_6nm	$GdxMnFe_{2-x}O_4$	Gd(III) 4% for M(III)	6
$MnFe_2O_4$_Ho6_6nm	$HoxMnFe_{2-x}O_4$	Ho(III) 6% for M(III)	6
$MnFe_2O_4$_Zn14_4nm	$ZnxMn_{1-x}Fe_2O_4$	Zn(II) 14% for M(II)	4
$MnFe_2O_4$_Zn57_4nm	$ZnxMn_{1-x}Fe_2O_4$	Zn(II) 57% for M(II)	4

4.1.1 FMR and magnetic susceptibility analysis

The nanoparticles shown in Table 4.1 are ferromagnetic spinel ferrites except for the MnO nanoparticles. All these nanoparticles have displayed FMR under various magnetic fields applied, although they have shown different FMR absorption profiles as we can see in Figure 4.3. With careful examinations of the Electron Paramagnetic Resonance (EPR) absorption profiles and the magnetic susceptibility measurements, the change of resonance frequency can be simply correlated to the change in the magnetic susceptibility of these nanoparticles, despite the difference among all various chemical compositions and possible spin orders. As shown in Figure 4.4, the applied fields for the maximum FMR absorption under a constant excitation

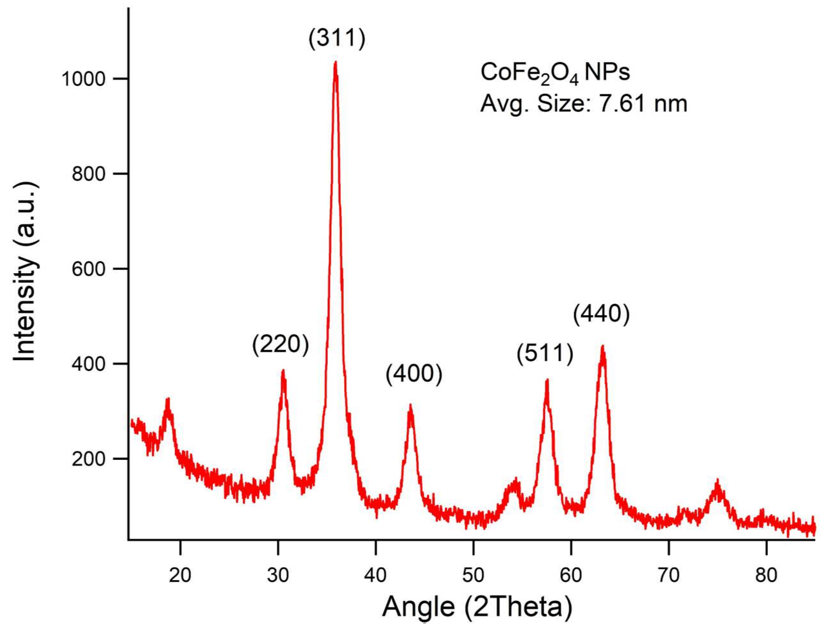

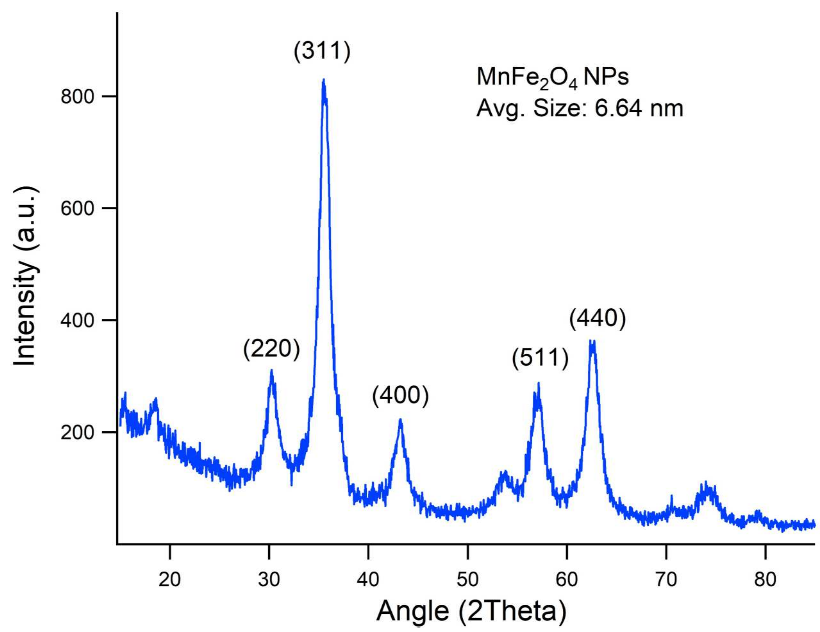

Figure 4.1: XRD pattern for $CoFe_2O_4$ (top) and $MnFe_2O_4$ (bottom), sizes calculated by Debye-Scherrer equation.

wavelength, $f = 9.88$ GHz were plotted versus the room temperature magnetic susceptibilities. Qualitatively, a trend could be addressed among these nanoparticles: with a larger magnetic susceptibility, a lower applied field is required to reach the resonance frequency at $f = 9.88$ GHz.

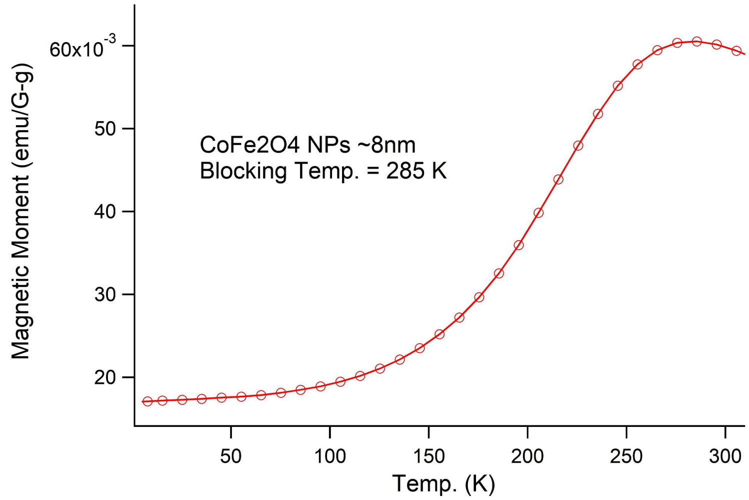

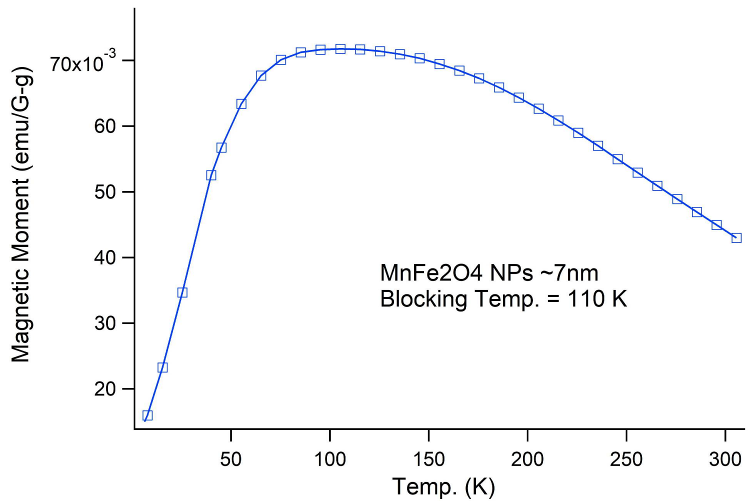

Figure 4.2: Temperature dependent magnetization for $CoFe_2O_4$ (top) and $MnFe_2O_4$ (bottom), zero-field cooled (ZFC) susceptibility measurements were conducted under an applied field of 100 G with temperature range from 5 - 310 K.

FMR is really an excitation of the nanoparticles between two energy states. With a higher magnetic susceptibility, the degree of magnetization would be larger in response to an applied magnetic field, and thus cause a larger energy difference between two energy states. This results in a smaller applied field in EPR measurements to achieve the fixed resonance frequency. In our EPR studies, this FMR excitation can be achieved by sweeping the applied magnetic field under a fixed frequency. Also this excitation can occur with a sweeping frequency under a fixed applied magnetic field as in microwave components of a wireless device. The trend in Figure 4.4 suggests that the FMR frequency increases with increasing magnetic susceptibility of the materials. FMR absorption profiles can also be affected by more physical factors, i.e. spin-orbit coupling, g-value shift and damping factor of the ferromagnetic materials. It is worthy to note that two different slopes could be found based on the difference of the FMR line widths in Figure 4.4. A more detailed study within certain types of particles and with the elimination of other factors has addressed the qualitative correlation between the susceptibilities and FMR frequency [28].

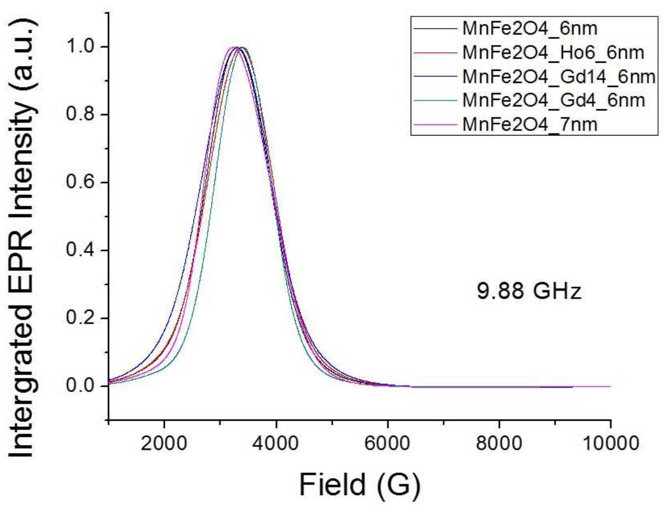

Figure 4.3: Selected FMR absorption profiles.

4.1.2 FMR measurement of film particles

For RF applications, the nanoparticles have been cast into films with a layer-by-layer method with a thickness of a few micrometers or a solution casting method with a film thickness of several ten to hundreds of micrometers. The nanoparticles and organic components that form the film were collected from the complete films to measure the FMR absorptions. The results shown in Figure 4.5 are 7 nm $MnFe_2O_4$ nanoparticles and 8 nm $CoFe_2O_4$ nanoparticles, with a 10 times magnification of the original signal. Compared to $CoFe_2O_4$, $MnFe_2O_4$ tends to gain narrower absorption peak profiles with a stronger intensity which is easier to observe

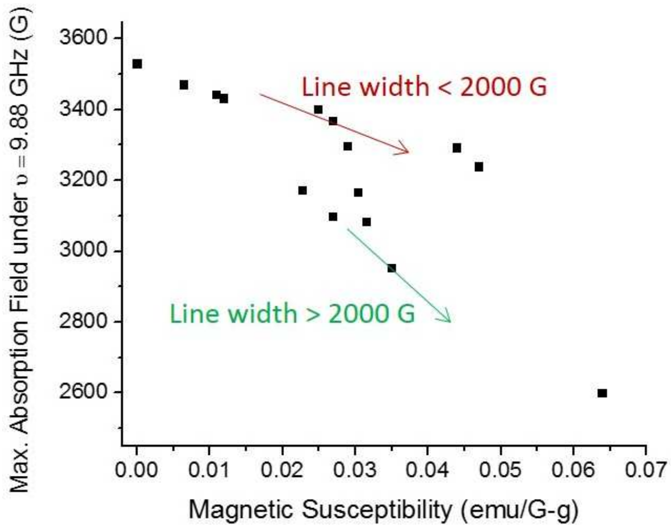

Figure 4.4: Correlation between resonance fields and magnetic susceptibilities.

during the measurements. The resonance intensity of $MnFe_2O_4$ nanoparticles is 100 times stronger than the same amount of $CoFe_2O_4$ nanoparticles. As shown in Figure 4.5, the strong spin-orbit coupling arising from Co^{2+} could broaden the FMR absorption profile and thus $CoFe_2O_4$ tends to be a lot less sensitive than $MnFe_2O_4$ in FMR spectrum. In all, such comparison exhibits the stronger signal response for $MnFe_2O_4$ nanoparticles over the weak signal response of $CoFe_2O_4$ nanoparticles. It requires 100x $CoFe_2O_4$ to achieve a similar RF response to the $MnFe_2O_4$ nanoparticles. Thus, from a device performance perspective, it is better to have manganese ferrite films to be integrated into RF devices such as FSL, to have narrower and sharper signal absorption profiles given the same amount of magnetic nanoparticles in the films.

4.2 Fabrication process of the magnetic nanoparticle thin film and the basic microwave device

The magnetic nanoparticle films used for the characterization here are fabricated on the 1 inch × 1 inch soda lime glass slides of 1 mm thickness. Two types of magnetic material nanoparticles-$CoFe_2O_4$ and $MnFe_2O_4$-are deposited on the glass substrate through

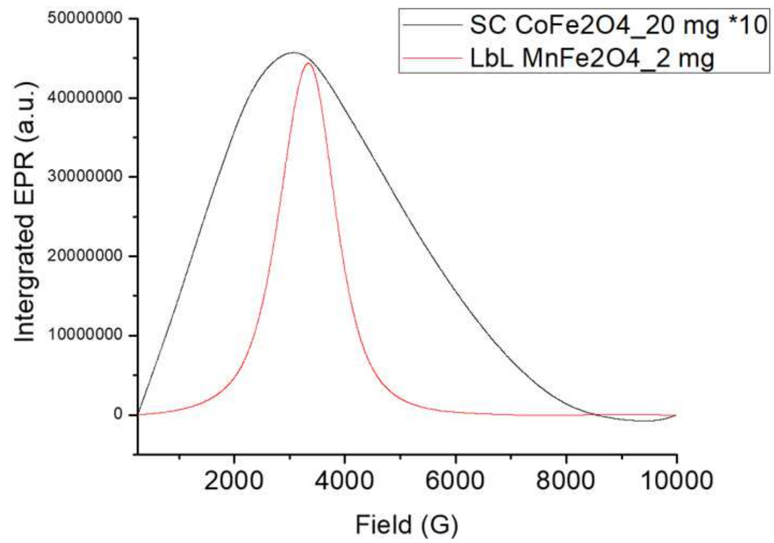

Figure 4.5: FMR of nanoparticle films. The intensity from $CoFe_2O_4$ nanoparticle film has been amplified 10 times from the original signals.

either the LbL process or the SC method. Details of these two kinds of deposition methods are introduced and compared. The LbL film fabrication technique has been developed for decades and proven to produce high-quality nanoparticle thin films with high loading density; whereas the SC method has been pretty common in industrial manufacturing for films with thickness in micro-meter range. In order to achieve comparable FMR absorptions, different film fabrication methods were applied onto different particles. $MnFe_2O_4$ films were built up through LbL to maintain uniform layer structures with thickness not exceeding 5 μm. $CoFe_2O_4$ films were made with the SC method to ensure that a large quantity of particles could be deposited onto one film surface. It is worth noting that the thickness of SC $CoFe_2O_4$ films was more than 10 times the thickness of LbL $MnFe_2O_4$ films; which provides the compensation of the FMR sensitivity from the particle nature. For the purpose of the characterization, we designed and 3-D printed a simple tapered microstrip line as the test bed. Together with the 3-D printed clamping and supporting structures, we built a basic microwave device using the magnetic film.

4.2.1 Layer-by-Layer Fabrication of $CoFe_2O_4$ Thin Films via Epoxy Curing

The $CoFe_2O_4$ nanoparticles were chemically bound to the glass substrate using the S_N2 nucleophilic addition between the surface-coated amine groups and epoxy groups. Hence two sets of surface modified particles were prepared, namely, 3-aminotriethoxypropylsilane coated particles and (3-glycidyloxypropyl) trimethoxysilane coated particles. The glass slides were surface modified with (3-glycidyloxypropyl) trimethoxysilane prior to particle attachment.

4.2.1.1 Epoxy coated slides

(3-glycidyloxypropyl) trimethoxysilane ethanol solution was prepared (1% v/v) and the glass slide was dipped into the solution and allowed to soak for 30 minutes. After the slide was removed from the solution, it was air dried and ready to be further coated with particles.

4.2.1.2 Amine/ epoxy coated $CoFe_2O_4$ particles

The $CoFe_2O_4$ nanoparticles were synthesized and followed with NaOH stripping ensuring that the particle surface is bare without other capping agent: a 3-Aminotriethoxypropylsilane ethanol solution was prepared (1% v/v) and bare particles were added to it (1 mg/ 1mL). The solution was stirred overnight and the particles were collected through a magnet and washed with ethanol three times to remove any excess coating agent. The particles were then re-suspended into ethanol and agitated before being used. The same procedure was followed for epoxy coated particles, but the (3-glycidyloxypropyl)trimethoxysilane ethanol solution was used.

4.2.1.3 Layer-by-Layer Fabrication

The glass slide was dipped into an amine coated particle solution and then an epoxy coated particle solution. Each dipping step was set to 30 minutes and followed with rinsing and air-drying. With the alternating dipping from these two solutions, a film with a certain thickness could be made. The film was then protected by spin-coating a layer of Torlon TF4000 polymer onto the surface to both chemically and physically protect the underlying film.

4.2.2 Fabrication of $CoFe_2O_4$ Films via Solution Cast Method

4.2.2.1 Epoxy coated slides and particles

A (3-glycidyloxypropyl)-trimethoxysilane ethanol solution was prepared (1% v/v) and the glass slides and particles were dipped/soaked into the solution individually. The glass slide was removed from the solution after 12 hours and air-dried. The particles were collected through a magnet after stirring overnight and washed with ethanol for three times to remove any excess coating agent. The coated particles were suspended in an appropriate amount of dichloromethane.

4.2.2.2 Film Casting

Approximately 10-20% (w/w) poly(methyl methacrylate) PMMA was added to the particle DCM solution and stirred for approximately 30 minutes before the solution was cast onto the substrate. With a syringe the nanoparticle solution was applied to the prepared substrate evenly, allowing the solution to flood above the substrate. The film was air-dried and stored in a desiccator until treated with Torlon protective coating. The film was then protected by spin-coating a layer of Torlon TF4000 polymer onto the surface to both chemically and physically protects the underlying film.

The details of the fabricated magnetic films are summarized in Table 4.2. Figure 4.6 shows the images of a few samples. Specifically, sample LbL1 is made of $MnFe_2O4$ nanoparticles by the LbL process, whereas samples SC3, 39I and SC7 are deposited using the $CoFe_2O_4$ nanoparticles through the SC method. The film thicknesses of LbL2 and SC3 are 3 μm and 40 μm respectively. As we can see, both LbL1 and SC3 have evenly distributed nanoparticles and the color difference is mostly because of the materials nature. However, there is a large void in SC6 and a condensed area in SC7, which are due to the fabrication defects. The measured film thicknesses of the smooth area in both samples are 60 μm and 125 μm, respectively.

Table 4.2: Film thickness, types of materials and deposition methods of the magnetic films

	$MnFe_2O_4$					$CoFe_2O_4$			
	3μm		5.4μm	20μm	30μm	40μm	50μm	60μm	125μm
SC	-		-	SC1	SC2	SC3	SC4	SC5/SC6	SC7
LbL	LbL1	LbL2	LbL3	-	-	-	-	-	-

(a) LbL1

(b) SC3

(c) SC6

(d) SC7

Figure 4.6: Images of the $MnFe_2O_4$ sample LbL1 and $CoFe_2O_4$ samples SC3, SC6 and SC7.

4.2.3 Basic microwave device

To characterize the magnetic films, it is necessary to fit them into a test bed so that we can observe their effect. Here we first design a microstrip transmission line with a wide-to-narrow line taper transition as the core test bed. Particularly, most of the center area of the substrate is designed to be thin to let the substrate thickness be as comparable as possible to the magnetic film thickness as shown in Figure 4.7(a). The thick areas featured with the vias at the end of the substrate are used to maintain the substrate rigidity as well as facilitate the RF measurements by using the end-launch RF connectors, as illustrated in Figure 4.7(b). Then we flip the magnetic film on top of the microstrip line. In order to ensure a good

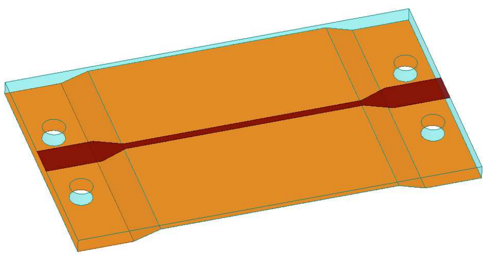

(a)

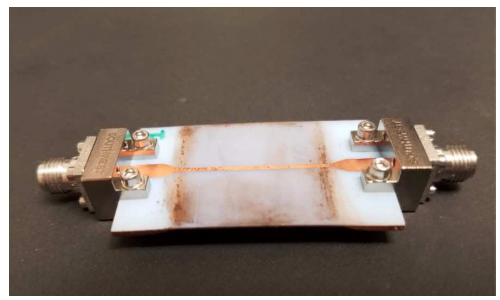

(b)

Figure 4.7: (a) Microstrip line design (b) Microstrip line characterized with end-launch connectors.

contact between the film surface and the microstrip line, we incorporate them using two 3-D printed fixtures. Figure 4.8(a) illustrates the overview of the whole basic microwave device. In practice, we also use two metal clamps for additional mechanic stability and applying more pressure, as shown in Figure 4.8(b). The transmitted electromagnetic wave along the

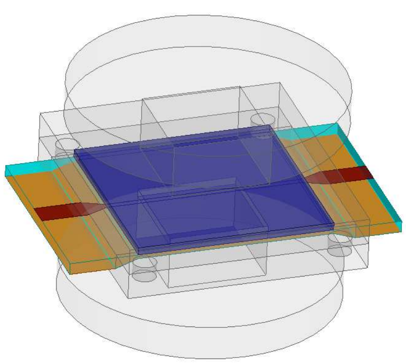

(a)

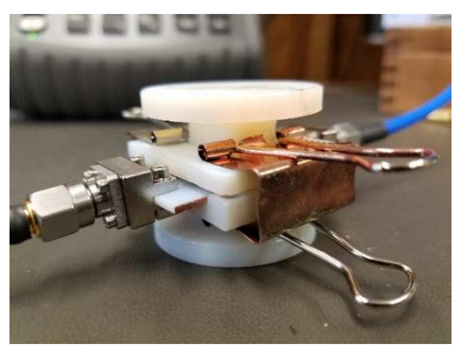

(b)

Figure 4.8: (a) Overview of the basic microwave device (b) The microwave device using additional two metal clamps and characterized by the RF end-launch connectors.

microstrip line is therefore mostly confined within the region that is near the signal trace. The presence of the magnetic nanoparticle film on top of the microstrip line now serves as the material perturbation to the RF magnetic field, affecting the scattering parameters of this two-port network, which is illustrated in Figure 4.9. As such, the influence due to the existence of the magnetic nanoparticles can be seen from the changes of the corresponding group delay and insertion loss.

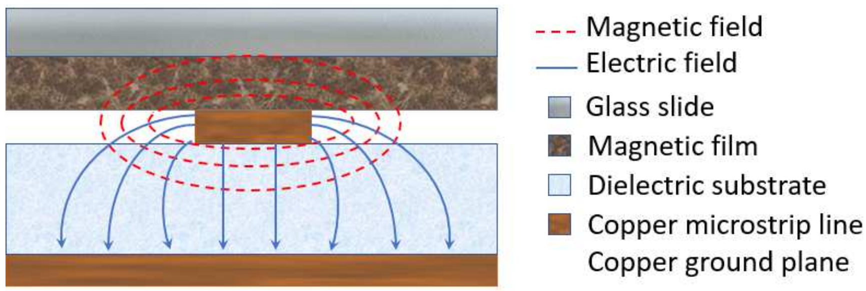

Figure 4.9: Electromagnetic fields illustration of the flipped magnetic film sample on the microstrip line.

4.2.4 3-D polyjet printing technology

The microstrip substrate and the basic microwave device assemblies are 3-D printed. The 3-D polyjet technology is advantageous for its low cost and fast prototyping, especially since it allows for fabricating complex structures that are difficult and expensive to manufacture by using the traditional micro-machining and photo-lithography methods. A commercially available Objet Connex 350 3-D polyjet printer is used, with a resolution of 100 μm in the X/Y axes and 30 μm in Z axis as shown in Figure 4.10. The printer head can move in X and Y axes patterning the planar geometry, and the thickness profile can be generated by moving along the Z axis. The material used to print the substrate is a photopolymer resin named *VeroWhitePlus*, with a dielectric constant of 2.8 and loss tangent of 0.04 [29]. The material is instantly cured by the UV light integrated on the printer head. Temporary supporting material can be easily flushed away after the printing is done. After the substrate is printed and cleaned, the microstrip line is patterned through a copper sputtering process using a

3-D printed mask which avoids the expensive cleanroom and photo-lithography fabrication process. Especially the 3-D printed assemblies would be difficult and costly to manufacture traditionally.

(a)

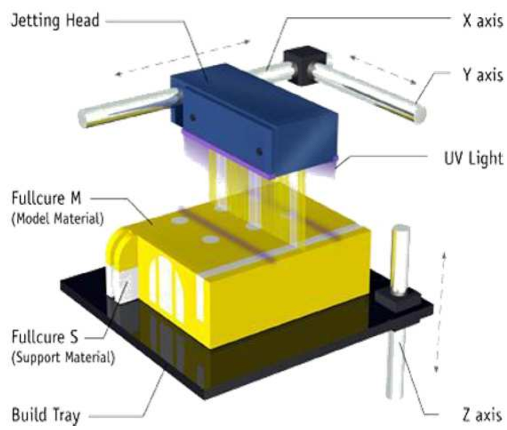

(b)

Figure 4.10: (a) Objet Connex 350 (b) Illustration of the 3-D polyjet technology [69].

4.3 Measurement results using the basic microwave device

As discussed in Figure 4.9 of Section III, due to the existence of the magnetic nanoparticles in the film, the RF magnetic field of the microstrip line is perturbed, which is reflected by the changes of the group delay and insertion loss compared to the case without the magnetic film. Furthermore, magnetic films with various thicknesses which differ in the amounts of magnetic nanoparticles, deposited using different types of materials and methods are supposed to display distinct amount of group delay. For example, although the relative permeability of different types of magnetic nanoparticles may vary, given the same type of magnetic nanoparticles and fabrication method, thicker films are supposed to result in higher group delay. Considering the fabrication limits in practice, the optimum combination of the fabrication method, types of materials and films thickness is needed to obtain the desired film properties in a time and cost efficient manner. Therefore, by examining the extracted group delays of all the samples, we can get some insights into the relationship of the magnetic film thickness, types of magnetic material, deposition methods and the amount of group delay. Ultimately, our goal is to characterize the magnetic material by determining the relative permeability which enables us to fabricate the monolithic microwave devices and circuits utilizing such materials.

4.3.1 Measurement setup

Since the magnetic film sample mainly consists of a layer of magnetic nanoparticles and a 1 mm thick soda-lime glass substrate, in order to justify the observation results in terms of the group delay, we establish the observation baseline by measuring the group delay of a mere soda-lime glass substrate with the same size of the magnetic film sample, but without the magnetic nanoparticles, flipped on top of the microstrip line, as illustrated in the upper picture of step 2 in Figure 4.11. Therefore, the only difference between the baseline case and the magnetic film sample case is whether the magnetic nanoparticles exist or not. In other words, assuming that all the environmental factors are the same, the difference of the group delays between the baseline case and the magnetic film sample case can be only attributed to the existence of the magnetic nanoparticles. The measurement setup has four steps as illustrated in Figure 4.11: a) tightly connect two coaxial cables to the end-launch connectors of the microstrip line (note that the microstrip line substrate should be flat without any twist since the *VeroWhitePlus* substrate is thin and flexible); b) place the microstrip line on the fixture platform; c) establish the observation baseline by flipping the glass slide on top of the microstrip line in step 2, and enclose the whole sample with the fixture cap as well as two clamps in step 3 such that the RF structure is stable and ready to measure; d) measure the scattering parameters using the portable Keysight Vector Network Analyzer (VNA) and record the data. After measuring the baseline case, we take off the clamps and the fixture cap (while keeping the connection between the VNA and the microstrip line), replace the mere glass slide with the magnetic film sample (glass slide + magnetic nanoparticle film) and repeat steps 3 and 4 to obtain the data of the magnetic film case.

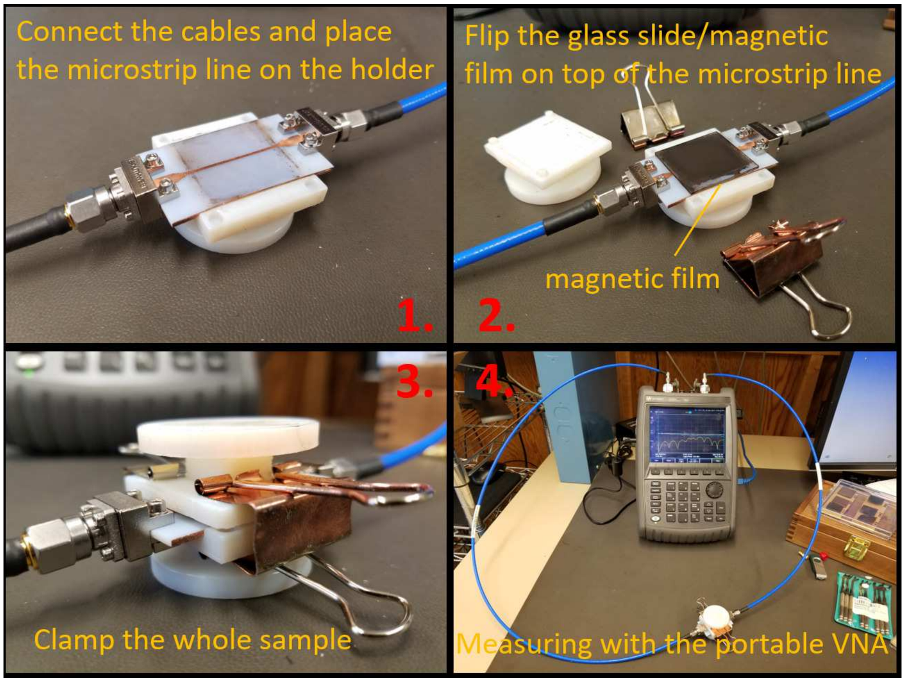

Figure 4.11: Measurement setup process steps 1-4.

4.3.2 Measurement Results

The scattering parameters can be measured for the above basic microwave device, where S_{21} denotes the ratio of the transmitted signal over the incident signal between the two ports of the device. The group delay that is associated with the relative permeability is a measure of the phase response of the transmitted signal. From the magnetic field distribution of Figure 4.9, we can see the thicker and denser the magnetic film, the more the RF magnetic field is confined within the magnetic film region, thus causing a stronger phase delay. Therefore the measured group delay is a good indicator of the effect due to the magnetic film. From the measured scattering parameters, the group delay can be extracted from the S_{21} using the following equation:

$$Group\ delay = -\frac{d\phi}{d\omega} \tag{4.1}$$

where the phase $\phi = rad(S_{21})$, and ω denotes the angular frequency. Although it is sufficient to have the baseline established, another reference line in which no glass slide is flipped on top of the microstrip line is also provided. Specifically, if step 2 in Figure 4.11 is skipped, then the measured result reflects the group delay of the microstrip line itself, which can be used as the reference line of the established baseline, as shown in Figure 4.12. We can see from Figure 4.12 that the “baseline” has a higher group delay than the Reference line, and the average group delay value for both cases is 350ps and 337ps, respectively, indicating that the presence of the mere glass slide introduces an extra group delay than the plain microstrip line as expected. Therefore, the baseline measurement and the whole microwave device setup are proven to be effective and correct.

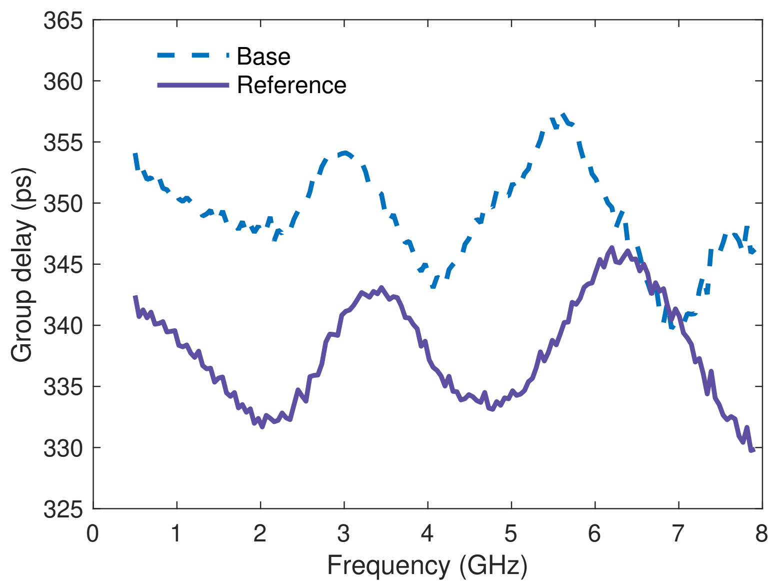

Figure 4.12: baseline: Mere glass substrate flipped on top of the microstrip line. Reference line: Only microstrip itself.

Figure 4.13 shows the measured group delay for all the Cobalt Ferrite samples deposited against the baseline. As we can see, a higher group delay is displayed for the Cobalt Ferrite samples than the baseline. And within all the Cobalt Ferrite samples, we can observe different values of the group delay. For example, the average group delay for the sample SC1 is 354ps, while that of the sample SC3 is 357ps. Since all samples except sample LbL3, are deposited using the same type of material (Cobalt Ferrite) and method (Solution Cast), the primary reason for the difference of the group delay is the magnetic film thickness. According to the nature of the SC method, higher quantity of the magnetic nanoparticles is supposed to exist in the thicker magnetic film, thus causing higher group delay compared to the baseline or thinner magnetic films. To verify this proposition, the samples are first ordered in an ascending manner in terms of the film thickness from Table 4.2; such film thickness sequence is then compared to the measured group delay sequence from Figure 4.13 which is ordered in a similar fashion as the film thickness sequence. The comparison result is illustrated in Figure 4.14. We can see that the sequence based on the film thickness can be mostly verified

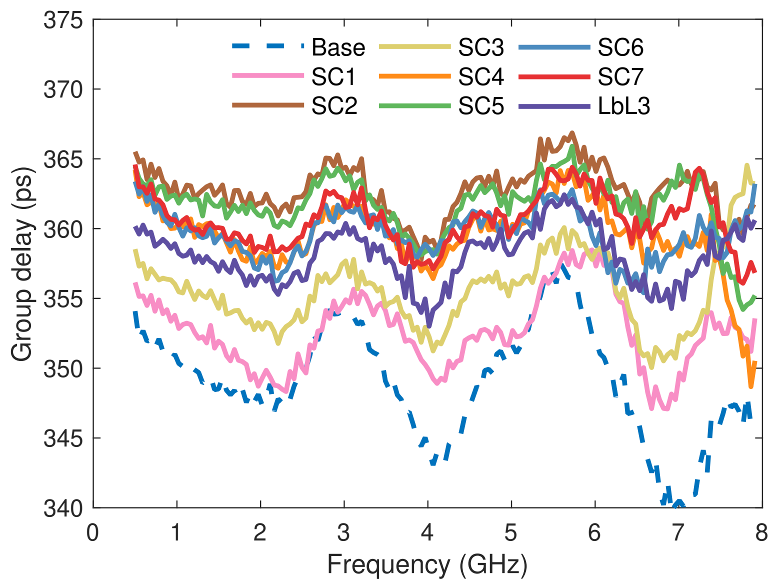

Figure 4.13: Group delay for all the solution cast $CoFe_2O_4$ samples and the baseline.

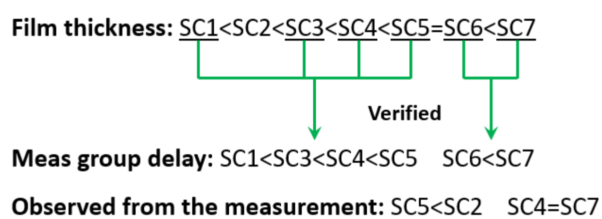

Figure 4.14: Solution cast $CoFe_2O_4$ sample sequences in terms of the film thickness and the measured group delay.

by the measured group delay in Figure 4.13. However, SC6 and SC7 are supposed to exhibit the second and first most group delay among all the samples, as opposed to about the same amounts of group delay as sample SC4. As observed previously in Figure 4.6, the large void in SC6 and the condensed area in SC7 that occurs during the deposition process reduces the amount of the group delay, which is supposed to be higher if the magnetic nanoparticles are evenly distributed. And the reason of SC5<SC2 from the group delay, which is contrary to the film thickness based result, may be attributed to the fabrication variation resulting in more magnetic nanoparticles actually deposited in SC5 than SC2. Therefore, based on the verified sequence of SC1<SC3<SC4<SC5, the relationship between the average group delay and the magnetic film thickness is plotted in Figure 4.15, where the measured group delay is averaged in the range of 1-8 GHz for each sample. From Figure 4.15 we can see that within our expectation, the thicker the magnetic film, the higher group delay. More importantly, the relationship between the above two quantities is almost linear, indicating that the good effectiveness of the SC method and the group delay can be potentially even higher if we continue increasing the magnetic film thickness (assuming an almost uniform nanoparticle distribution with no major fabrication defects).

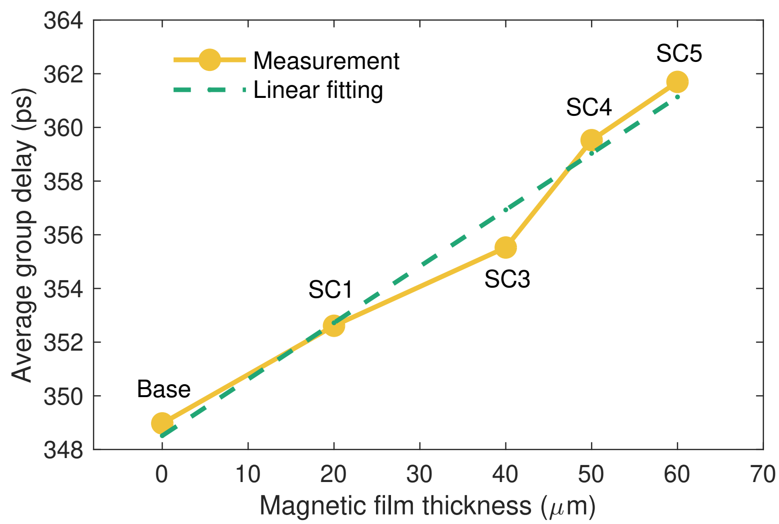

Figure 4.15: The relationship between the average group delay and the magnetic film thickness for selected solution cast $CoFe_2O_4$ samples and the baseline.

On the other hand, sample LbL3 is fabricated by depositing the same $CoFe_2O_4$ nanoparticles via the LbL process. Hence it can be used to study the effects of the different deposition methods. Again, it can be observed from Figure 4.13 that SC3<LbL3<SC4 in terms of the differences of group delay. However, Table 4.2 shows the film thickness of LbL3 is only 5.4 μm as opposed to the film thickness of SC3 (40 μm) and SC4 (50 μm), suggesting the LbL

process is better than the SC method at producing magnetic film that results in higher group delay given the same film thickness. In fact, through the TGA experiment on the film fill factor, the LbL process results in 90% weight percent nanoparticles, while that of the SC method is about 68%, as shown in Figure 4.16. However, it takes much longer to deposit the same film thickness using the LbL process than the SC method. Specifically, using the LbL process, it usually takes 4-5 days to achieve a 5-6 μm film thickness; for the SC method, approximately 3-4 hours are needed to fabricate a 50-60 μm film, including 1-2 hours of substrate preparation and 1-2 hours of film deposition. Therefore, given no restrictions on the film thickness and targeting the same level of group delay, the SC method is more efficient in producing much thicker films if a shorter fabrication cycle is preferred.

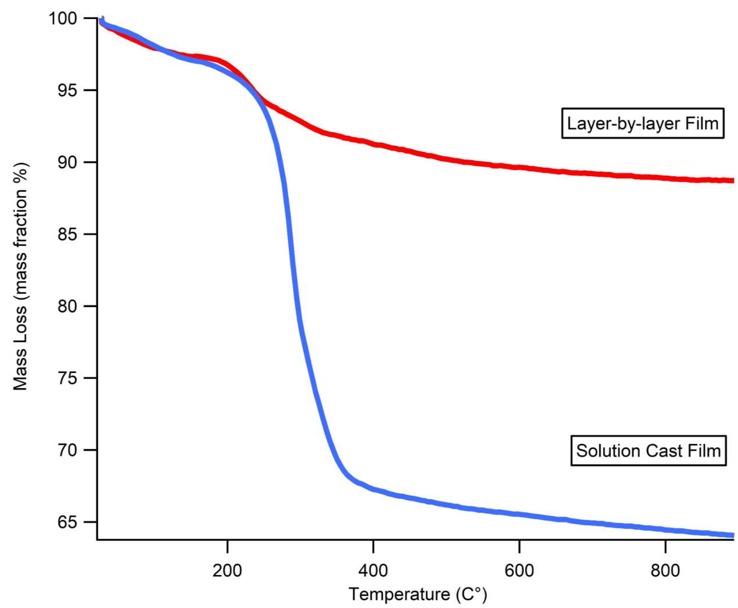

Figure 4.16: TGA curves for LbL and solution cast films showing particle loading densities of 90% and 65% for LbL and solution cast respectfully.

To determine the effects of different types of magnetic materials, $MnFe_2O_4$ samples LbL1 and LbL2 are compared with $CoFe_2O_4$ sample LbL3 in Figure 4.17 since they are all made via the LbL process (both samples have uniform nanoparticle distribution). First, it can be seen that the average group delay for both LbL1 and LbL2 is around 365 ps given only 0.1 μm variance in terms of the film thickness, while LbL3 introduces 357 ps of group delay in

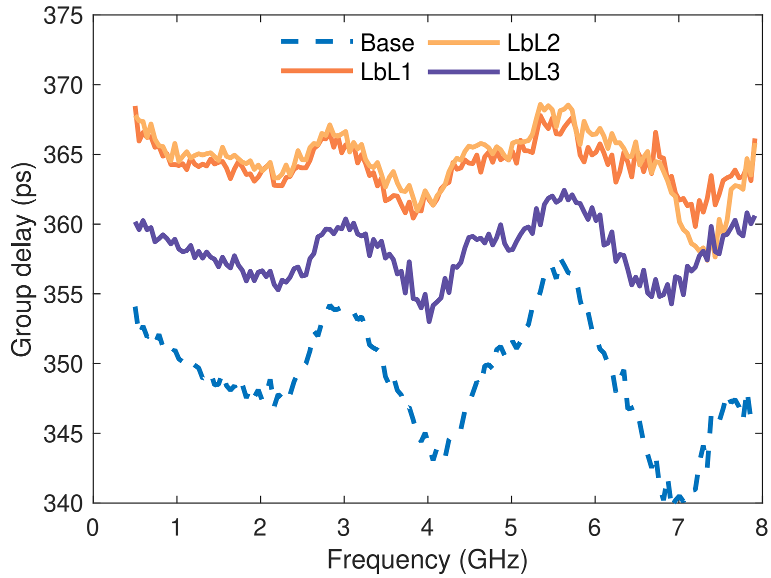

Figure 4.17: Group delay for the $MnFe_2O_4$ samples LbL1 and LbL2 and $CoFe_2O_4$ sample LbL3.

average which is less than that of LbL1 and LbL2. As shown in Table 4.2, LbL3 is even more than twice of the film thickness of LbL1 and LbL2, indicating that manganese ferrite nanoparticles have stronger ability than cobalt ferrite nanoparticles in increasing the group delay.

Based on the above comparisons on fabrication methods and types of magnetic materials, we conclude that the SC method is faster in fabricating magnetic films and the manganese ferrite nanoparticles exhibit stronger effect in increasing the group delay. Thus, we can claim that for the purpose of making the magnetic film achieve a certain level of group delay increase, the most time efficient method is to fabricate such film using manganese ferrites via SC. Such a combination also has the potential for further improvements. If the fill factor of the films made by the SC method can be improved from 68% to 90% or comparable to the LbL process, then-for the same group delay-the required film thickness to be achieved through the SC method can be reduced and, thus, less fabrication time will be needed. In other words, given the same film thickness and fabrication time, the film will introduce higher group delay by improving the fill factor of the SC method.

Figure 4.18 (a) and (c) shows the S_{21} and S_{11} measurements for all the samples, which

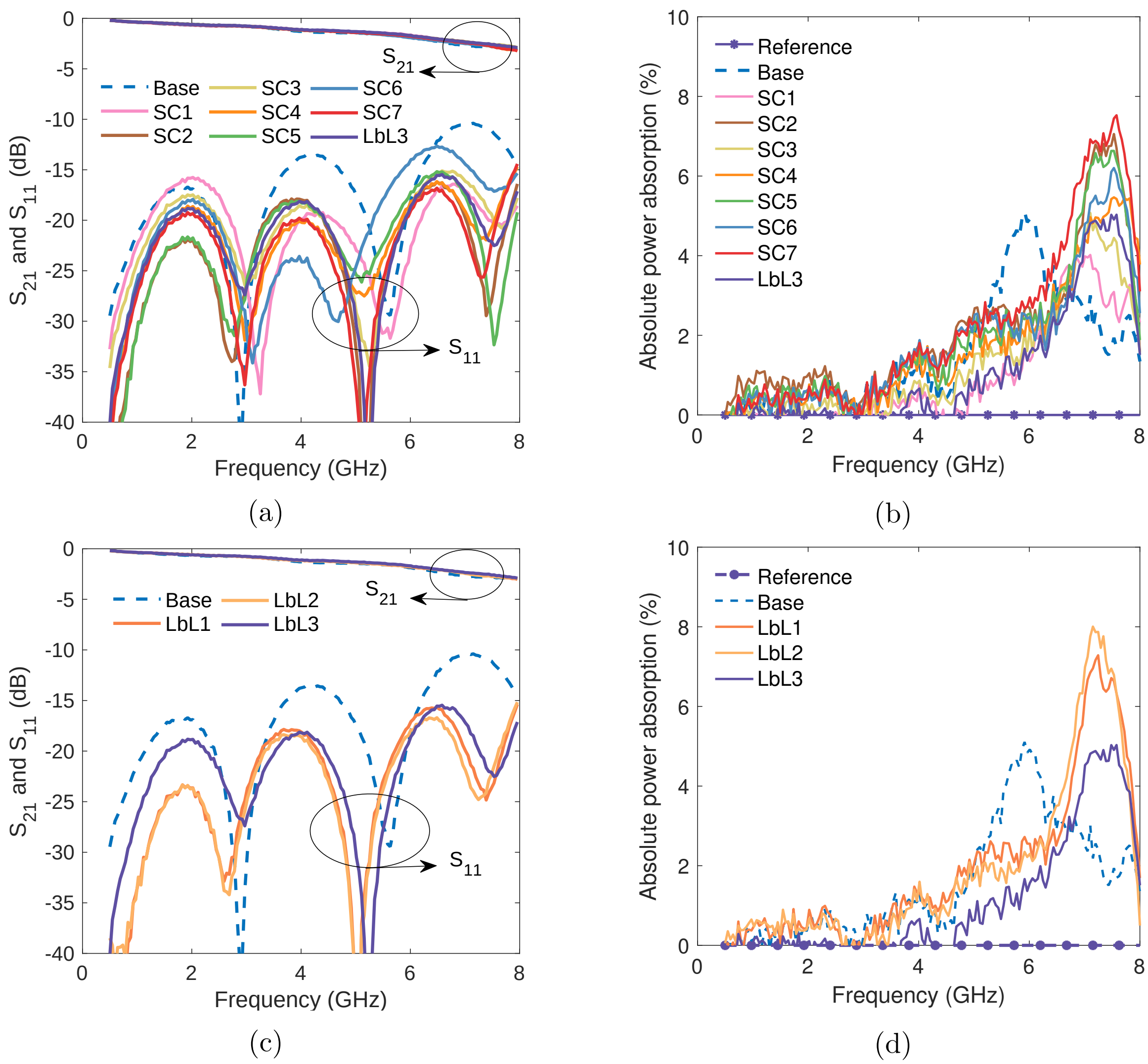

Figure 4.18: (a) S_{21} for all $CoFe_2O_4$ magnetic films (b) The absolute power absorption percentage for all $CoFe_2O_4$ magnetic films (c) S_{21} of LbL1 and LbL2 compared to SC7 (d) The absolute power absorption percentage LbL1 and LbL2 compared to SC7.

can be used to determine the transmitted signal power absorption rate solely due to the presence of the magnetic films. The power absorption is a very important property to know due to the FMR, which can be utilized in microwave devices, like FSLs, to determine the attenuation level to the unwanted interference signals. We first calculate the overall signal power loss percentage PL of all cases by using the following equation:

$$PL = 1 - |S_{21}|^2 - |S_{11}|^2 \tag{4.2}$$

If we denote PL_0 as the calculated power loss of the "Reference" case where only the microstrip line exists (without soda lime glass slide or magnetic films on top), then the absolute power absorption rate PL_r due to the magnetic samples can be obtained by subtracting PL_0 from the calculated PL's of all the magnetic samples, that is:

$$PL_r = PL - PL_0 \tag{4.3}$$

Therefore, the PL_r's of all the magnetic samples including the "Base" case against the frequency are depicted in Figure 4.18 (b) and (d). We can see that the power absorption increases with the frequency and compared to the "Base" case, where merely the glass slide exists, the magnetic samples absorb more transmitted energy and peak around 7.5 GHz. Additionally, we can observe the similar trend shown in Figure 4.14, such that thicker magnetic films absorb more power, because more magnetic nanoparticles existing in the thicker film convert the absorbed power into loss. We also determine the power absorbed by the magnetic nanoparticles PL_n by eliminating the effect of the glass slide, i.e., $PL_n = PL_r - PL_{Base}$. For example, the PL_n of sample SC7 is 5.9% at 7.5 GHz, which corresponds to 0.26 dB of total loss and 0.07 dB/cm of loss given the 4 cm length of the microstrip line. Thus, from the above perspective, we further prove the conclusion about the effectiveness of the proposed fabrication methods and the fact that the added line loss due to the magnetic nanoparticles is negligible.

4.4 Summary

This chapter presents the study of various magnetic nanoparticle based thin films. We propose new methods of fabricating magnetic films, namely the Layer-by-Layer process and the Solution Cast method. The magnetic films are made of $CoFe_2O_4$ or $MnFe_2O_4$ nanoparticles with a film thickness ranging from 2.5 μm - 125 μm. By exploring the relationship among different types of the magnetic materials, deposition methods, magnetic film thickness and the amount of group delay, it is evident that: (1) there exists a positive linear relationship between the magnetic film thickness and the amount of group delay, in other words, thicker magnetic film introduces higher group delay while the added loss is negligible assuming a uniform fill factor; (2) the LbL process produces more condensed magnetic films than the SC method but is less time efficient than the latter in producing thicker films, both methods are proven to be effective to fabricate thick magnetic films so that higher group delay can be introduced; and (3) given the same film thickness and deposition method, $MnFe_2O_4$ nanoparticles have a stronger ability in increasing the group delay than the $CoFe_2O_4$ nanoparticles. Given the aforementioned, we can conclude that it is most time efficient to fabricate magnetic nanoparticle films using manganese ferrites via the SC method to achieve a certain level of group delay increase, which can be further enhanced by improving the fill factor of the SC method. The SC method can be easily implemented in wafer scale or board size fabrication processes. The above conclusions give the guidelines and pave the way for fabricating monolithic microwave integrated circuits and devices utilizing such magnetic films.

CHAPTER 5

PATCH ANTENNA ON NIFE$_2$O$_4$ NANOPARTICLE AIR SUBSTRATE

The rapid development of modern wireless communication systems has led to a continuously growing demand for compact, efficient and wideband antennas [31]. So far, various techniques have been investigated and employed for antenna miniaturization, such as shorting pins [32], fractal shape [33], dielectric loading [34], and using electromagnetic band gap structures or metamaterials [35][36]. However, these techniques generally either sacrifice bandwidth and efficiency or are hard to fabricate and integrate with monolithic circuits.

Another type of miniaturization approach is loading the antenna with bulk ferrite materials or magnetodielectric materials as substrate/superstrate which exhibit relative permittivity ϵ_r and relative permeability μ_r both greater than unity ($\epsilon_r > 1$ and $\mu_r > 1$), so that the antenna can be miniaturized by the factor of $n = \sqrt{\epsilon_r \mu_r}$ [37]–[40]. Normally a large biasing magnetic field is needed for bulk ferrite materials to operate at a high frequency, or their lossy nature prevents them to be used at frequencies larger than 1 GHz under self-biased conditions [41], [42]. Magnetic thin films, however, have been reported for achieving a decent resonant frequency shift (2 – 71 MHz), gain and bandwidth enhancement for patch and annular ring antennas operating higher than 1 GHz under self-biased conditions [43]–[45]. However, the magnetic film is rather thin (2 – 10 μm), thus it would be of great interest to fabricate and utilize thick magnetic films for substantial antenna miniaturization with improved performance.

In our previous work, we have proposed low cost and effective chemical methods of fabricating thick magnetic films using various material composite nanoparticles, which were utilized to develop several RF circuits with improved performance [46]–[48]. Recently in [48], a 30 μm MnFe$_2$O$_4$ nanoparticle film loaded rectangular patch antenna achieves a frequency shift of 0.5 GHz, a gain enhancement of 0.5 dB and an improved bandwidth by 0.14 GHz, which is promising in antenna miniaturization.

In this communication, we report for the first time much thicker Nickel-ferrite ($NiFe_2O_4$) nanoparticle films ranging from 875 – 900 μm within the fully 3D printed air cavity. The loaded patch antennas exhibit a significant resonant frequency shift of 0.75 – 1.75 GHz with an enhanced bandwidth of 0.16 – 0.25 GHz relative to the nonmagnetic counterpart. This large frequency shift indicates a 9.3–21.4% of size reduction. We also obtain enhanced antenna efficiency and gain when good film quality is achieved. To the best of the authors' knowledge, this work demonstrates the thickest magnetic films fabricated for RF and antenna applications using a simple and cost effective chemical method, and the largest resonant frequency shift with enhanced antenna performance which leads to a great potential in low cost, miniaturized RF circuits and antennas.

5.1 Antenna design and theoretical analysis

5.1.1 Antenna on Air Substrate

The microstrip rectangular patch antenna is designed to resonate at 8.14 GHz, and the inset-fed topology is used to match the antenna input impedance to a 50 Ω microstrip line. To minimize the dielectric loss, the antenna pattern is etched on top of a 2 mil ($\approx$ 0.05 mm) Liquid Crystal Polymer (LCP) membrane which is suspended over a 1 mm deep 3D printed metalized cavity, thus forming an air substrate antenna, as shown in Fig.1(a). The LCP has a dielectric constant $\epsilon_r = 3.14$, and a loss tangent $\tan\delta = 0.0025$ [49], and since it only occupies a small portion of the air substrate, the effective dielectric constant of the air substrate is very close to unity ($\epsilon_{r\_sub} \approx 1$) and the loss tangent is close to zero. In fact, the plastic auxiliary part shown in Fig.1(b) slightly increases the ϵ_{r_sub}, therefore, $\epsilon_{r\_sub} = 1.1$ is chosen in our design. The design parameters are labeled and provided in Fig.1.

Such an antenna configuration is beneficial over an antenna on a regular PCB board with $\epsilon_{r\_sub} \gg 1$, because the proposed design can enhance the antenna efficiency by minimizing

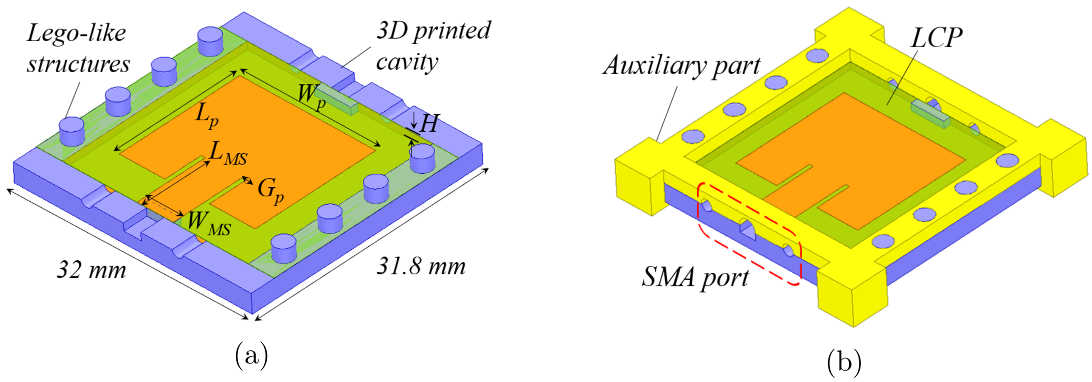

Figure 5.1: (a) The design parameters: $L_p = 18.2$ mm, $W_p = 18.3$ mm, $W_{MS} = 4.9$ mm, $L_{MS} = 9.41$ mm, $G_p = 0.55$ mm, $H = 1.05$ mm; (b) Fully assembled antenna with auxiliary part.

the dielectric loss and improving the space wave radiation. This can be easily understood using the lossy resonator cavity model for the patch antenna, where the TM_{010} mode is the fundamental mode for a broadside radiation pattern of the antenna. As we know, the total quality factor Q of the patch antenna can be decomposed as [74]:

$$Q = \left[\frac{1}{Q_{sp}} + \frac{1}{Q_{sw}} + \frac{1}{Q_c} + \frac{1}{Q_d}\right]^{-1} \tag{5.1}$$

where Q_{sp} denote the desired space wave radiation quality factor, while Q_{sw}, Q_c, and Q_d represent the dissipated power quality factors due to the TM_0 mode surface wave, conductor loss and dielectric loss, respectively. And the antenna efficiency can be thereby defined as [74]:

$$\eta_{rad} = \frac{Q}{Q_{sp}} = \frac{1}{1 + Q_{sp}\left(\frac{1}{Q_{sw}} + \frac{1}{Q_c} + \frac{1}{Q_d}\right)} \tag{5.2}$$

It is obvious from (5.2) that the antenna efficiency can be enhanced by decreasing the space-wave quality factor Q_{sp} and increasing the loss related quality factors Q_{sw}, Q_c, and Q_d. Again, according to [74], the quality factors Q_{sp}, Q_c, and Q_d are given as:

$$Q_{sp} = \frac{2\omega_0\, \epsilon_{r\_sub}}{h_{sub}\, G_t/L_{patch}} K \tag{5.3}$$

$$Q_d = \frac{1}{\tan\delta_\epsilon} \tag{5.4}$$

where h_{sub} is the thickness of the substrate, σ is the bulk conductivity of the metal conductor, G_t/L_{patch} is the total conductance per unit length of the radiating aperture, and $K = \frac{L_{patch}}{4}$ for a rectangular patch antenna operating in the dominant TM_{010} mode.

Because of $\epsilon_{r\_sub} \approx 1$ and $\tan\delta_\epsilon \ll 0.0025$ of the air substrate, we can easily observe from (7.3) and (7.4) that the Q_{sp} and the Q_d of the proposed air substrate antenna are significantly decreased and increased, respectively, compared to the antennas on lossy high dielectric substrates. Meanwhile, both Q_c and Q_{sw} are not affected as they are not related to ϵ_{r_sub} and $\tan\delta_\epsilon$, which for the sake of brevit is not discussed here, instead, they are further discussed in the next section of magnetic film loading. Although the antenna efficiency can be enhanced with the air substrate, the physical dimensions of the antenna are inevitably larger than its counterparts on high dielectric substrates. Thus, it is of great interest to miniaturize the air substrate antenna while maintaining or enhancing the performance.

5.1.2 Antenna on Magnetic Film Loaded Substrate

As mentioned in Section I, one of the effective miniaturization methods is through loading the antenna with high permittivity or high permeability materials as a superstrate to enhance the efficiency while reducing the antenna size. The efficiency enhancement principle can be explained using the transmission line equivalent model, as the superstrate acting as an impedance transformer to improve the coupling between the antenna and the free space [51]. The authors in [44], [45], and [52] demonstrated respectively that by loading magnetic films and dielectric as superstrate, the gain of the antenna can be enhanced. However, the superstrate configuration inevitably increases the vertical height of the overall package since it essentially adds additional top layers to the original circuit, although the horizontal size is reduced. Thus it is hard to integrate superstrate loaded antennas into ICs, especially in the compact hand held devices.

In our work, by taking advantage of the flexibility of the 3D printing technique and the low cost chemical methods [46], we managed to deposit significant amounts of $NiFe_2O_4$

nanoparticles within the air cavity such that the magnetic film thickness is very close to that of the air substrate, thereby creating an antenna on magnetic film loaded substrate, as shown in Fig. 2 (the auxiliary part is not shown). Note that the magnetic film thickness can be adjusted through our chemical deposition process, which grants us another degree of freedom to control the antenna performance.

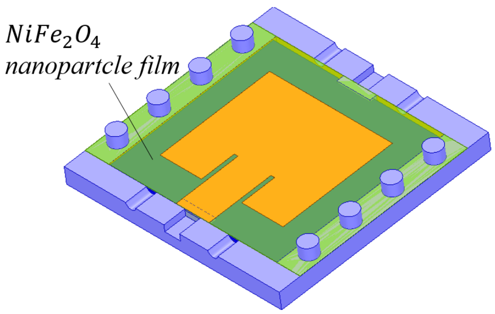

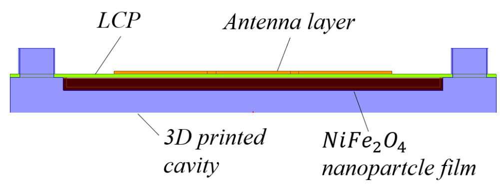

Figure 5.2: (a) Patch antenna on the $NiFe_2O_4$ magnetic film loaded substrate; (b) The cross sectional view of the magnetic film loaded antenna.

Because of the loaded magnetic film, the antenna substrate now has a $\mu_{r\_sub} > 1$, and a magnetic loss tangent $\tan\delta_\mu$ which depends on the inhomogeneity of the film, the nanoparticle fill factor, and the film surface roughness[53]. Therefore, (5.1) and (**??**) can be modified as:

$$Q = \left[\frac{1}{Q_{sp}} + \frac{1}{Q_{sw}} + \frac{1}{Q_c} + \frac{1}{Q_d} + \frac{1}{Q_m}\right]^{-1} \tag{5.5}$$

and

$$\eta_{rad} = \frac{1}{1 + Q_{sp}\left(\frac{1}{Q_{sw}} + \frac{1}{Q_c} + \frac{1}{Q_d} + \frac{1}{Q_m}\right)} \tag{5.6}$$

where the magnetic loss quality factor $Q_m = \frac{1}{\tan\delta_\mu}$. Since the dielectric loss tangent $\tan\delta_\epsilon$ of the $NiFe_2O_4$ nanoparticle films is very low [46], [54], we consider that the dielectric Q_d is not affected. Using the transmission line model, the total conductance G_t can be determined as [74]:

$$G_t = \frac{W_{patch}}{120\pi} k \left[1 - \frac{1}{24}\left(kh_{sub}\right)^2\right] \tag{5.7}$$

where $k = \omega_0\sqrt{\mu_{r\_sub}\,\epsilon_{r\_sub}}$. Substituting (5.7) into (7.3), we find out that Q_{sp} is inversely proportional to μ_{r_sub}, which implies the Q_{sp} is reduced by loading the magnetic film, thus more energy is radiated out. Besides, the conductor loss is reduced as Q_c is increased based on [74]:

$$Q_c = h_{sub}\sqrt{\pi f_0\,\sigma\,\mu_{r\_sub}} \tag{5.8}$$

The surface-wave Q_{sw} can be related to the space-wave Q_{sp} when only the surface-wave loss is considered, which is expressed as [55]:

$$Q_{sw} = Q_{sp}\left(\frac{e_r^{rad}}{1-e_r^{rad}}\right) \tag{5.9}$$

where the efficency e_r^{rad} can be well approximated by [55]:

$$e_r^{rad} = \frac{1}{1+\mu_{r\_sub}(k_0 h_{sub})\left(\frac{3\pi}{4}\right)c_1\left(1-\frac{1}{n_1}\right)^3} \tag{5.10}$$

where c_1 and n_1 are constants. We can see from (5.9) that increasing μ_{r_sub} leads to reduced e_r^{rad}, and so is the function $\frac{e_r^{rad}}{1-e_r^{rad}}$ in (5.8) as it is positively related to $e_r^{rad} \in [0,1]$. Since both Q_{sp} and $\frac{e_r^{rad}}{1-e_r^{rad}}$ are reduced with the magnetic film loading, we obtain the reduced Q_{sw}, which means the surface wave loss is increased.

At this point, the decrease of Q_{sp} and Q_{sw} and the increase of Q_c resulted from the magnetic film loading still leave the behavior of the overall Q and η_{rad} ambiguous. From [56], the bandwidth BW of a patch antenna printed on a magnetodielectric substrate is approximated as:

$$BW \approx \frac{96\sqrt{\frac{\mu_{r\_sub}}{\epsilon_{r\_sub}}}\frac{h_{sub}}{\lambda_0}}{\sqrt{2}\left[4+17\sqrt{\mu_{r\_sub}\,\epsilon_{r\_sub}}\right]} \tag{5.11}$$

which shows that increasing μ_{r_sub} yields broader BW. And due to the following relationship [55]:

$$FBW = \frac{VSWR-1}{Q\sqrt{VSWR}} \tag{5.12}$$

where $FBW = BW/f_0$, we can conclude that loading the magnetic film increases the BW and decreases the overall antenna quality factor Q.

Therefore, based on (5.2), we can summarize that the antenna efficiency η_{rad} can be enhanced by loading the magnetic film when the reduction of Q is less than the reduction of Q_{sp}. However, if the film quality is poor, the excessive magnetic loss and surface loss will lead to more reduction of Q than that of Q_{sp}, resulting in a deteriorated antenna efficiency. While the BW is enhanced due to the increased μ_{r_sub} and/or loss.

5.1.3 Impedance matching, realized gain analysis

For magnetic films that have $\sqrt{\mu_{r\_sub}/\epsilon_{r\_sub}} \approx 1$, the impedance matching of the antenna can be improved. Just like the superstrate, thinking in terms of the transmission line equivalent model, the magnetic films serves as an impedance transformer which helps to enhance the coupling between the antenna and the air. Therefore, it will result in better input reflection coefficient Γ_{in} of the antenna.

With that in mind and let D denote the directivity of the antenna, then we can derive the realized gain of the antenna on the magnetic film loaded air substrate as

$$G_{real} = \eta_{rad} \left(1 - |\Gamma_{in}|^2\right) D \tag{5.13}$$

As we discussed in the last section, the radiation efficiency η_{rad} of the proposed antenna will reduce assuming no advantageous frequency dispersion, however, it does not necessarily imply that the realized gain of the antenna will also hereby decrease. Since we may be able to obtain better impedance matching, the reflected input power of the antenna can be lowered, thus theoretically we can have higher realized gain. But if the radiation efficiency is too low, such that its negative effect outweighs the contribution of the improved matching, the realized gain will still go down. Again, our experiment results reveal that the magnetic film loaded antenna obtained better realized gain in certain case, but such gain can drop down due to far worse radiation efficiency, as we will see in the following section.

5.2 The characteristics of $NiFe_2O_4$ films and Antenna Fabrication Process

Traditionally, bulk ferrite materials with high permeability and low loss are used in RF and microwave applications under 600 MHz, including in antenna miniaturization [39], [40]. At frequencies >600 MHz, the magnetic loss of these materials increases rapidly with FMR being the most significant loss which hinders these materials to be used in GHz frequency range. Therefore, the FMR frequency caps the frequency range in which the antenna substrates can operate on.

Recently, research has shown that the magnetic film laminates, for example NiCo-ferrite films, under self-biased condition exhibiting high magnetization saturation and large in-plane and out-plane anisotropy difference can have FMR frequency in several GHz, and were successfully utilized for antenna miniaturization [43]–[45]. For such applications, two of the most important parameters are the static relative permeability of the magnetic substrate μ_{r_sub} and the FMR frequency of the material f_{FMR}. It is well known that these two quantities are inversely related to each through Snoek's law. For most bulk magnetic materials, it can be described as

$$(\mu_{r\_sub} - 1) f_{FMR} = \frac{2}{3} \gamma \, 4\pi M_s \tag{5.14}$$

where $\gamma \approx 2.8$ MHz/Oe which is the gyromagnetic constant, and $4\pi M_s$ is the magnetization saturation. For thin magnetic films with in-plane anisotropy, this relation can be modified as

$$(\mu_{r\_sub} - 1) f_{FMR}^2 = (\gamma \, 4\pi M_s)^2 \tag{5.15}$$

which shows the μ_{r_sub} are allowed to be larger given the same FMR frequency. It has to be pointed out both (5.14) and (5.15) are estimated results in certain cases. In fact, μ_{r_sub} and f_{FMR} are dependent on the effective anisotropy field of the material, which, in turn, depends on the material composition, as well as the manufacturing process, treatment, small admixtures, etc. In addition, the relative permeability of the magnetic materials can be modeled as a complex format using the Lorentzian dispersion rule at low frequencies. In our paper, for simplicity, we only consider the static relative permeability μ_{r_sub} since the Lorentzian dispersion rule is not applicable at GHz range.

5.2.1 The Characteristics of $NiFe_2O_4$ Films

In our recent work, magnetic films made of various composites that were fabricated using effective and low cost chemical methods have been characterized to exhibit high magnetization saturation and controllable film thickness[46]. These magnetic films have been demonstrated in RF circuits and antennas to show good performance[47], [48]. In this communication, we report for the first time, the 875–900 μm thick $NiFe_2O_4$ nanoparticle films, which to the best of the author's knowledge, are the thickest magnetic films fabricated for RF and antenna applications using a simple chemical fabrication method. The $NiFe_2O_4$ film has a magnetization saturation $4\pi M_s = 40.2$ kG, and a linewdith $\Delta H = 850$ G [47].

The LandauLifshitz-Gilbert (L-L-G) equation is used to describe the magnetodynamics. By defining α as the Gilbert damping factor, H_{appl} is the applied field, and H_k is the in-plane anisotropy field, we have $\omega_{appl} = \gamma\mu_0 H_{appl}$, $\omega_k = \gamma\mu_0 H_k$, and $\omega_m = \gamma\mu_0 M_s$. Then the in-plane susceptibility spectra of the magnetic films is given by

$$\chi(\omega) = \frac{\omega_m\left(\omega_m + \omega_k + \omega_{appl} + j\omega\alpha\right)}{-\omega^2 + j\omega\alpha\omega_m + \omega_m\left(\omega_k + \omega_{appl}\right)} \tag{5.16}$$

5.2.2 $NiFe_2O_4$ Films Fabrication Process

First, the cavity used for $NiFe_2O_4$ nanoparticles deposition was 3D printed using polyjet technology, which was widely used for RF and microwave applications due to its fast prototyping, low cost, and environmentally friendly advantages. We used a professional grade commercially available Connex Objet350 polyjet printer which features a resolution of 100 μm in the X/Y axes and 30 μm in Z axis, and the cavity was printed using a ABS plastic like photosenstive polymer resin called *VeroWhitePlus* [57]. The detailed information about the polyjet technology can be referred in previous chapters.

After the cavity was printed, it was cleaned by flushing away the unnecessary supporting material and was further sanded for smooth surfaces. The inner surfaces of the cavity have to be metalized to provide the RF ground plane for the patch antenna. We first sputtered 0.5 μm of titanium as the seed layer to promote the adhesion between the *VeroWhitePlus* surface and the following copper layer, then an approximate 5 μm of copper was sputtered and electroplated. Based on our experiment trails, we found out the chemical solution that was later used to deposit the $NiFe_2O_4$ nanoparticles was very corrosive which may etch through the thin metal layer. Therefore, in our actual sample as shown in Figure 5.3a, a 50 μm thick copper tape was placed on top of the electroplated copper layer. Note that the ground plane and the two edges where the SMA connectors were meant to be soldered on was covered by the copper tape, and additional small portion of solder was applied to ensure the positioning as well as the electrical connectivity.

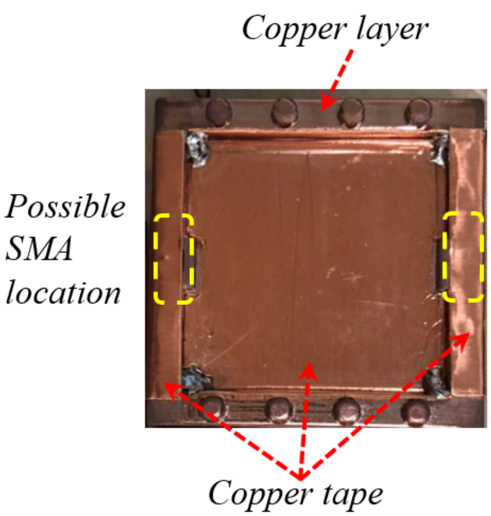

(a)

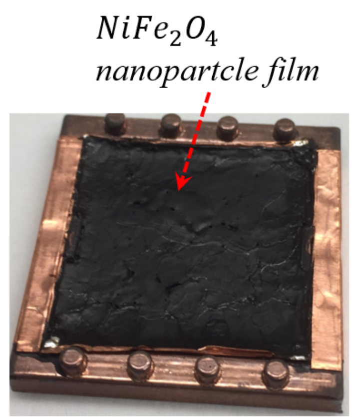

(b)

Figure 5.3: (a) The 3D printed cavity with metalized surfaces; (b) The fabricated $NiFe_2O_4$ magnetic film.

The $NiFe_2O_4$ nanoparticles film was then deposited using the low-cost chemical method called Solution Cast which was proposed in Chapter 4. Specifically, the nanoparticles were first surface treated using (3-glycidyloxypropyl)-trimethoxysilane ethanol solution, and were then collected through a magnet to mix with 10-20% (w/w) poly(methyl methacrylate)

PMMA and an appropriate amount of dichloromethane. This nanoparticle based solution was applied evenly within the 1 mm deep cavity by a syringe. After it was air-dried and stored in a desiccator, a layer of Torlon TF4000 polymer was spin-coated onto the surface to both chemically and physically protect and stabilize the underlying film. Note the thickness of the film can be controlled through the amount of $NiFe_2O_4$ nanoparticles being deposited within the cavity. The size of the magnetic nanoparticles can also be controlled through managing either time or temperature of the reaction solution. Figure 5.3b shows one of the fabricated $NiFe_2O_4$ film loaded air cavity in the experiment test, which has the estimated film thickness of 0.9 mm.

Figs. 5.4(a)-(c) show the three fabricated magnetic film samples. We can observe that all three films display a certain degree of inhomogeneity. Sample 2 (S2) shows the best surface uniformity with the least number of cracks, whereas sample 1 (S1) has more film cracks. And the film surface of sample 3 (S3) is shattered with a concave area in the center. The profilometry data of the film edge and center, as indicated in Fig. 5.4(d), are provided in Fig. 5.4(e) and (f), respectively. The corresponding root-mean-square (rms) surface roughness of S1–S3 is 13, 3, and 31 μm, respectively. Since the cavity depth is 1 mm, then by evaluating the edge–film surface difference, we can estimate the corresponding film thickness of S1–S3 to be 875, 900, and 900 μm, respectively.

In fact, multiple profile scan had been done for the above two areas, although the actual data are somewhat varying, qualitatively the observation results are the same, i.e., the surface roughness from the most to the least: S2>S3>S1 and the vertical difference from the largest to the smallest: S1>S2>S3. Moreover, some surface areas of the film samples accumulate significantly more nanoparticles than the surrounding areas creating a heavily rough profile, which may potentially damage the probe of the profilometer, thus the surface roughness data of these areas and the edge-edge cross section scan data are not available. Despite this, it will not dramatically affect our observation results. Since the variance of the edge vertical differences is less than 30 μm based on multiple scan, our above film thickness estimation is

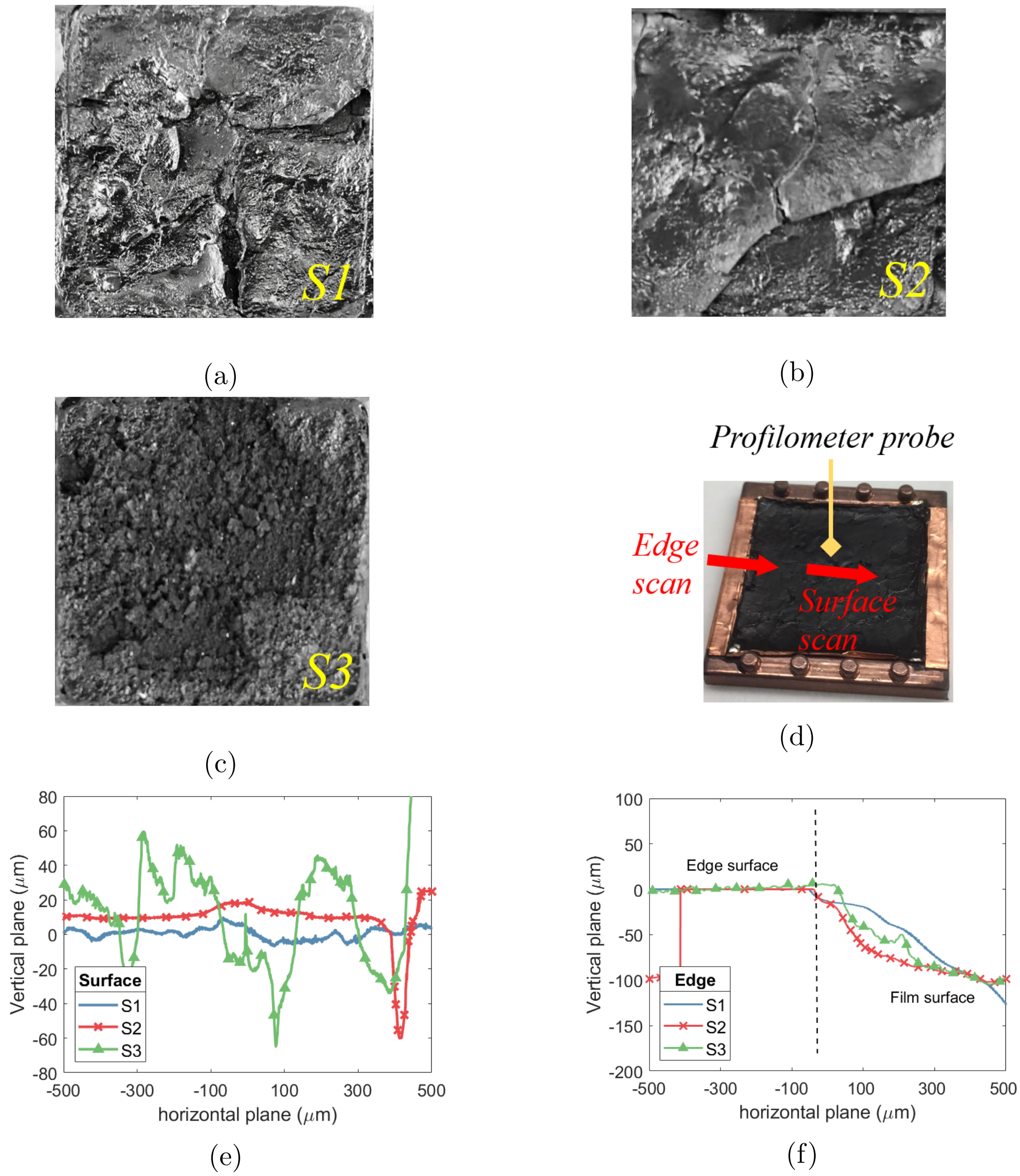

Figure 5.4: (a)-(c): Sample S1, S2, and S3; (d) Illustration of edge and surface scan using profilometer; (e) Surface scan profile; (f) Edge scan profile.

still valid.

Based on our analysis, we would expect the film roughness and thickness to affect our antenna performance. Particularly the cracks of film will introduce additional energy loss. Since it is a magnetic film loaded air substrate, the film thickness will also affect the substrate effective relative permeability μ_{r_sub}. In addition, one of the important figures of the film quality is the fill factor of the $NiFe_2O_4$ nanoparticles which evaluates the concentration of

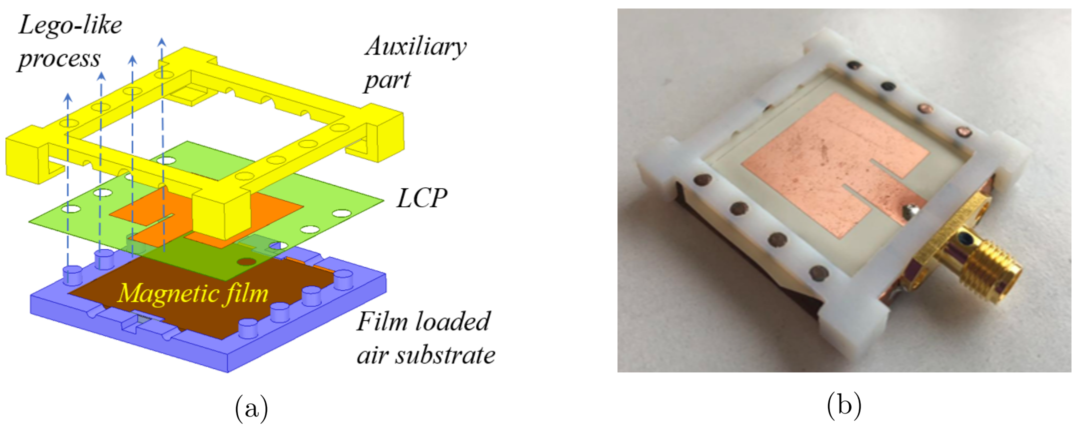

Figure 5.5: (a) The lego-like assembly process; (b) Fully assembled $NiFe_2O_4$ nanoparticle film loaded air substrate antenna

the nanoparticles in a unit volume, however, it may require destructive measurement on the film. The fill factor along with the above film quantities will determine μ_{r_sub}, f_{FMR}, and $\tan\delta_\mu$ etc, and eventually affect our antenna performance.

5.2.3 Antenna Fabrication and Assembly

The designed rectangular patch antenna was patterned on top of a 2 mil Rogers LCP through standard photolithography process, then four holes of each side were punched through near the two edges of the antenna pattern. We also 3D printed an auxiliary part which serves for the two purposes: (1) Evenly stretch and mechanically stabilize the LCP on top of the film loaded air cavity; (2) Facilitate the SMA connector assembly to the antenna. Finally, through the lego-like process shown in Figure 5.5(a), we can achieve antenna on the $NiFe_2O_4$ nanoparticle film loaded air substrate. The fully assembled antenna with SMA connector that is ready for measurement is shown in Figure 5.5(b). We can see the overall antenn package is very compact and light-weight, and the whole fabrication process is very low cost with very little wastes.

5.3 Antenna measurement results and analysis

5.3.1 Antenna measurement setup

The reflection coefficient of the antenna was measured using the Keysight N5227A Performance Network Analyzer, which was calibrated using the SOL method up to the SMA connector. And the antenna radiation pattern measurement was conducted using the SATIMO Starlab near field system, in which the near-to-far field transformation was performed through the built in software. The system is calibrated up to the cable connector using the standard horn antenna customized for the system. Figure 5.6 shows the anechoic chamber measurement setup. We measured the antenna samples on both air substrate and $NiFe_2O_4$ nanoparticle films loaded substrate configurations. Particularly for the later configuration, three antenna samples were measured in two scenarios: (1) The magnetic films under self-biased condition; (2) A DC magnetic bias was applied perpendicular to the patch plane using permanent magnets. The corresponding measurement results are shown in the following two sections, respectively.

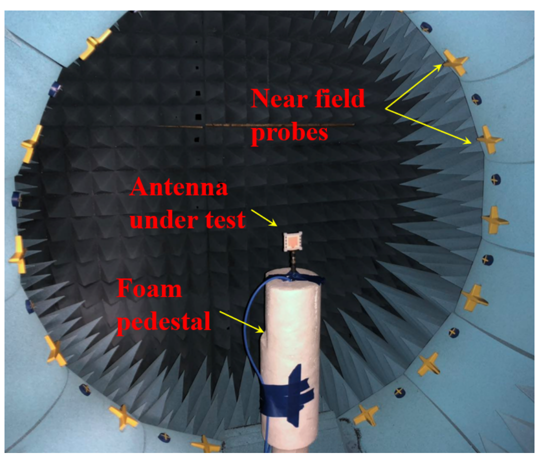

Figure 5.6: The radiation pattern measurement setup using SATIMO Starlab near field system

5.3.2 Antenna on the self-biased magnetic substrate

The measured S_{11} of S1–S3 and the air substrate antennas are plotted in Fig. 5.7. The S_{11} of S1, S2 and the air substrate antennas are simulated using FEKO and HFSS, respectively. Since S1 and S2 have better film quality than S3, the film is assumed to be homogeneous and flat with 875 and 900 μm thickness, respectively, and by closely matching the simulated resonant frequency (S1: 6.39 GHz, S2: 7.04 GHz) to the measured value (S1: 6.46 GHz, S2: 7.11 GHz), we can estimate the $\mu_{r\_sub} = 15$, and $\tan\delta_\mu = 0.04$.

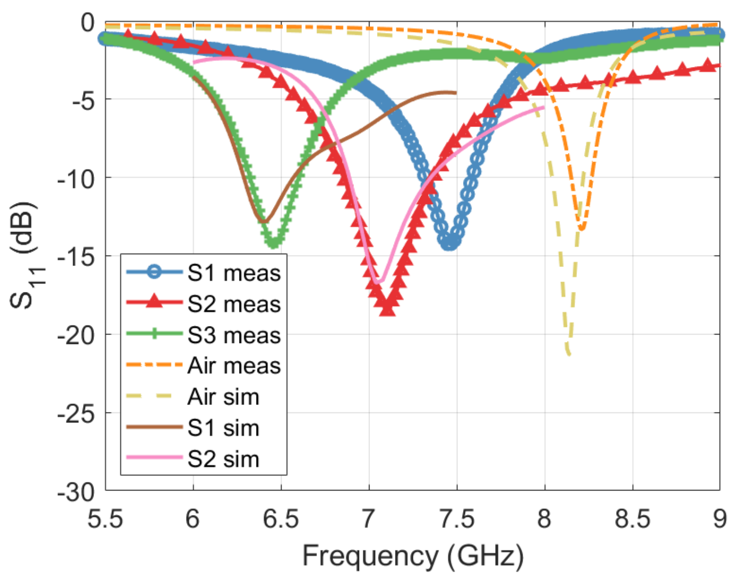

Figure 5.7: The measured S_{11}: S1–S3 and air substrate antenna, the simulated S_{11}: S2 and air substrate antenna.

As shown in Fig. 5.7, for the air substrate case, the measured S_{11}=-13.2 dB at the resonance of 8.21 GHz, which agrees well with the simulated result. The small differences are due to the fabrication error, soldering loss, and the uneven surface of the LCP membrane. By loading the $NiFe_2O_4$ nanoparticle films in S1–S3, we observe a down shift of the resonance. Specifically, compared to the measured resonant frequency of the air substrate case, the resonance down shift of S1–S3 is 0.75 GHz, 1.09 GHz, and 1.75 GHz, respectively. To the best of the authors' knowledge, the results show the largest frequency shifts that have ever been reported in the literature for antenna applications using the magnetic films as substrate/superstrate, which leads to significant antenna miniaturization.

In addition, the impedance matching and the BW are also enhanced for S1–S3. For example, at the resonance, S2 has a S_{11}= -18.5 dB and a BW= 0.51 GHz, which is 5.3 dB better and 0.4 GHz wider than those of the air substrate antenna. This result confirms the conclusion in Section II.C, that loading the magnetic films results in an enhanced BW because of the increase of μ_{r_sub}. This BW enhancement is also partially due to the loss of the films, but is minor compared to the μ_{r_sub} factor.

The measured radiation patterns of S1–S3 and the air substrate antenna are depicted in Fig. 5.8. The measured realized gain and radiation efficiency of the air substrate antenna at the resonance is 8.2 dBi and 85%, respectively, as opposed to the simulated values of 9.2 dBi and 87.4%. The difference is due to the impedance mismatch, unevenness of the LCP and copper tape loss. While for S1–S3, the measured realized gain is 8.5 dBi, 8.8 dBi, and 6.4 dBi, respectively, with the corresponding efficiency of 90%, 91%, and 68%. And we can observe that the broadside patterns of S1–S3 are mostly retained with the cross polarizations less than -20 dB.

Compared to the air substrate case, S1/S2 enhances the gain and efficiency by 0.3 dB/0.6 dB and 5%/6%, respectively. Such efficiency improvement is explained in Section II.C that the magnetic film helps enhance the space wave radiation by lowering Q_{sp}, while the good film quality of S1/S2 ensures minimum magnetic and surface wave loss; thus by (5.6) we obtain enhanced radiation efficiency. In contrast, when the film quality is poor, which is the case of S3, the corresponding efficiency is reduced by 17%. This is evidenced by Fig. 5.4(a)–(c) where S3 has more cracks and more than twice the surface roughness than S1 and S2, so that the film related loss completely counteracts the improved space wave radiation. However, with better film quality, we can expect more enhancement of efficiency, BW, and gain while obtaining significant antenna miniaturization. The reason that S3 has a larger frequency shift than S2 given the same 900 μm film thickness is because the magnetic nanoparticle fill factor of S3 is higher than that of S2, which results in a larger μ_{r_sub} in S3. A detailed comparison in terms of the aforementioned measured metrics of S1–S3 and the air substrate case is presented in Table 5.2. Fig. 5.9 compares the measured maximum realized gain and efficiency over the frequency band for S1–S3 and the air substrate antennas. We can see that with good film quality, the 3 dB gain bandwidth of S1 and S2 are significantly wider (approximately doubled) than that of the air substrate antenna, and a similar trend can be also observed on the efficiency from Fig. 8(b). Again, these results prove that the magnetic film can help improve the space wave radiation.

Table 5.1: Measured performance metrics of S1–S3 and the air substrate case

Terms \ Samples	Air	S1	S2	S3
Resonance f_r (GHz)	8.21	7.45	7.11	6.46
Resonant shift	–	9.3%	13.4%	21.3%
S_{11} (dB)	-13.3	-14.2	-18.5	-14.2
BW (GHz)	0.11	0.27	0.51	0.28
FBW (BW/f_r)	1.3%	3.6%	7.1%	4.3%
Max. realized gain (dBi)	8.2	8.5	8.8	6.4
Efficiency η_{rad}	85%	90%	91%	68%
Film thickness (μm)	–	875	900	900
rms surf. roughness (μm)	–	13	3	31

Table 5.2 compares the presented antennas with the recently published antennas using the similar magnetic material loading configuration or other antenna miniaturization techniques. As we can see, the fabricated magnetic film allows the proposed antennas to operate at a much higher GHz range compared to the traditional magnetodielectric composite substrate used in [38]. Given the patch antenna setting, because of the 875 μm film thickness of S1 which is much thicker than the 8 μm thick film used in [45] or the 30 μm thick film used in [48], S1 thereby has a much larger resonance shift, enhanced BW, efficiency and gain. Again, we expect more of such performance enhancement and size reduction when good film quality is achieved. Since it is known that the resonant frequency is inversely proportional to the antenna size/length, thus the resonant frequency shift can be interpreted as the antenna size reduction. Although other miniaturization techniques employed in [32], [33], [36] can lead to larger size reduction, one or more of their performance metrics are negatively affected, and

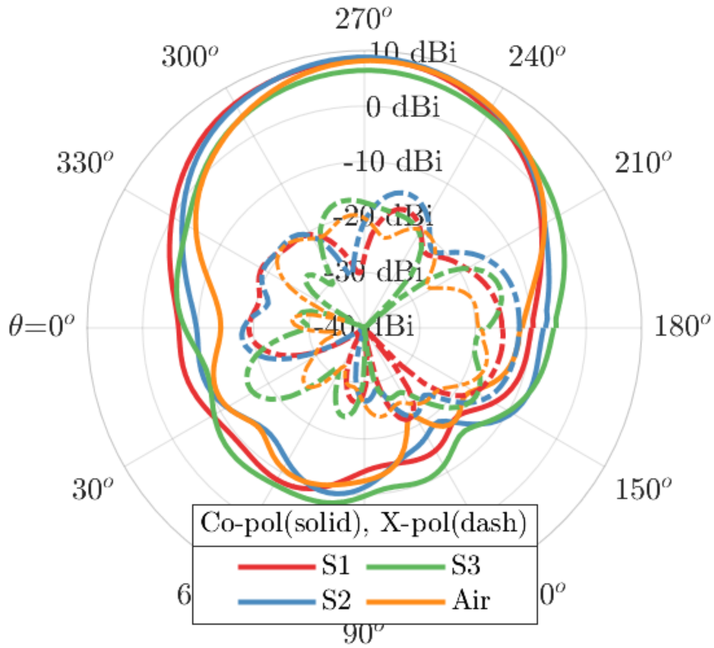

(a)

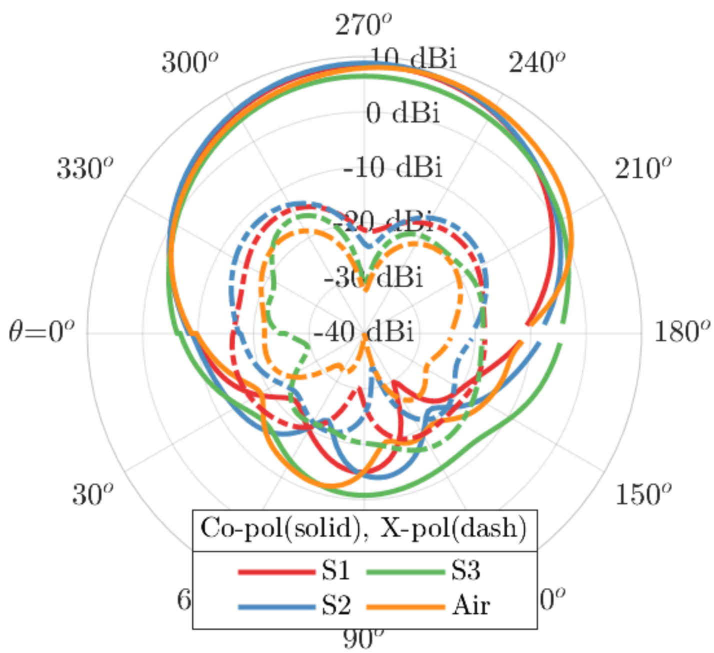

(b)

Figure 5.8: Measured radiation patterns for S1–S3 and air substrate antennas: (a) E plane; (b) H plane. Measured resonant frequencies: 7.45 GHz (S1), 7.11 GHz (S2), 6.46 GHz (S3), 8.21 GHz (Air).

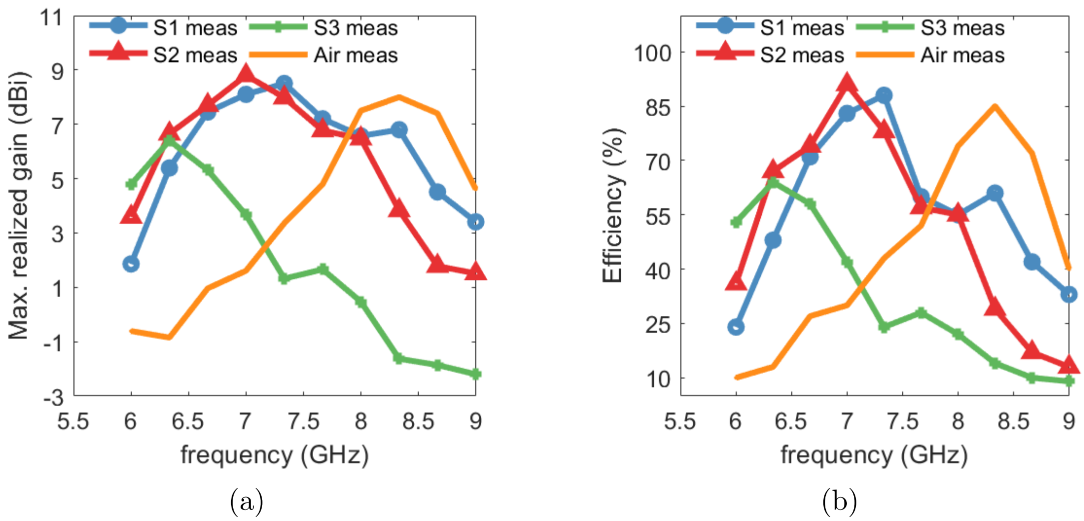

Figure 5.9: Measured maximum realized gain and efficiency vs. frequency for S1–S3 and air substrate antennas: (a) maximum realized gain; (b) efficiency.

some of them are relatively difficult to fabricate.

Therefore, based on our results, we can conclude that by using the proposed magnetic film loaded antenna, we can significantly miniaturize the antenna without comprising the antenna performance, instead, enhancing the antenna's bandwidth, efficiency, and gain at the same time which is usually not possible using traditional techniques. Especially in applications where high antenna gain and wide bandwidth are preferred over certain miniaturization, this work provides a novel way to satisfy such requirement and poses many advantages than the conventional designs.

5.3.3 Antenna on the DC magnetic biased magnetic substrate

One of the special characteristics of the magnetic material is the ferromagnetic resonance phenomenon, which represents the absorption capability of a magnetic material to electromagnetic waves of some frequency. The small-signal theory of FMR was developed by Kittel. This intrinsic property gives rise to the use of the magnetic materials in many tunable RF and microwave devices to achieve the unique performance. The FMR and the magnetic susceptibility characterization of the similar nanoparticles to our $NiFe_2O_4$ nanoparticles are

Table 5.2: Comparison of the reference antennas (data format in the upper half: before/after magnetic material loading, size reduction compared to the patch without loading; lower half: size reduction compared to the $\frac{\lambda}{2}$ patch).

Ref.	f_r & f_r shift size reduction	BW & FBW	η_{rad} (%)	Gain (dBi)
[38]	100/98 MHz 2 MHz / 2%	N.G./2 MHz N.G./2%	N.G.	N.G./0
[44]	1.72/1.671 GHz 49 MHz / 2.8%	5/7 MHz 0.3/0.4%	N.G.	0.6/1.3
[45]	2.147/2.097 GHz 50 MHz / 2.3%	18/39 MHz 0.8/1.9%	41/65	1.3/1.7
[48]	8.3/7.8 GHz 500 MHz / 6%	240/340 MHz 2.9/4.3%	N.G.	6.5/7
S1	8.21/7.45 GHz 760 MHz / 9.3%	110/270 MHz 1.3/3.6%	85 / 90	8.2/8.5
S2	8.21/7.11 GHz 1100 MHz / 13.4%	110/510 MHz 1.3/7.1%	85 / 91	8.2/8.8
S3	8.21/6.46 GHz 1750 MHz / 21.3%	110/280 MHz 1.3/4.3%	85 / 68	8.2/6.4

Ref.	f_r & size reduction	BW & FBW	η_{rad} (%)	Gain (dBi)
[32] DSPA Rogers 5880	2.153 GHz 62%	9.9 MHz 0.46%	77.2	5.2
[32] DSPA FR4	2.455 GHz 62%	37 MHz 1.5%	9	-4.9
[33] Fractal patch	5.2 GHz 38%	21 MHz 0.4%	N.G.	N.G.
[36] Patch on MTM	250 MHz 85%	2 MHz 0.83%	19.8	-3.9

referenced in Chapter 4.

In the antenna applications, the DC magnetic bias is usually applied either through permanent magnets or electromagnetic circuits embedded inside the substrate. The latter approach usually requires costly and complicated fabrication process. By applying the magnetic bias, the antenna can be granted many beneficial properties such as resonant frequency tuning, the change of polarization sense, etc. Here we simply used permanent magnets as the DC magnetic bias source, trying to explore the corresponding effects. As we can see in Figure 5.10, four 7 mm × 7 mm cylinder Neodymium permanent magnets were put together at the back of the antenna, and a double sided tape was placed in between to ensure the magnets adhere to the antenna. The field strength provided by the magnets is measured as 975 Gauss. The measured S_{11} and the radiation patterns are compared against the scenario of self-biased case, which are shown in Figure 5.11 and Figure 5.12(a)–(f), respectively. Note that the antenna samples used in this measurement are not the same samples measured in Fig. 5.7.

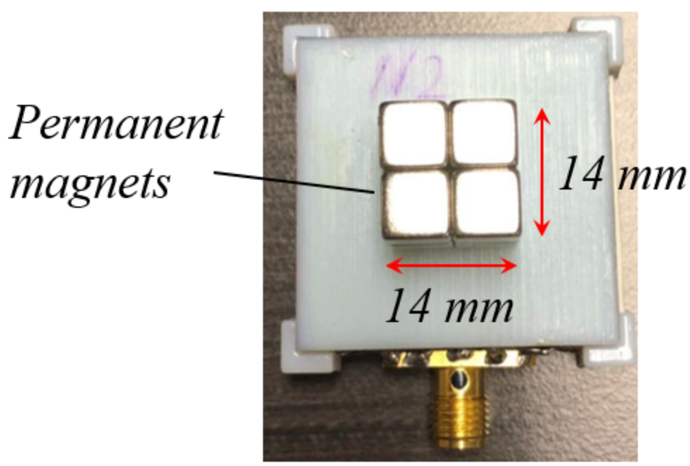

Figure 5.10: The antenna sample with permanent magnets on the back

From Figure 5.11, we can obviously see that the DC magnetic bias causes significant changes to the antenna performance for all three samples, among which S3 experienced the most, i.e., the efficiency was reduced 23.1%, the maximum realized gain was lowered by 2.7 dB, and the level S_{11} dropped down by 32.4 dB. It is interesting to note that for S3, even the impedance matching was improved significantly, the final realized gain was still reduced. This is because the heavily degraded efficiency counteracted such impedance

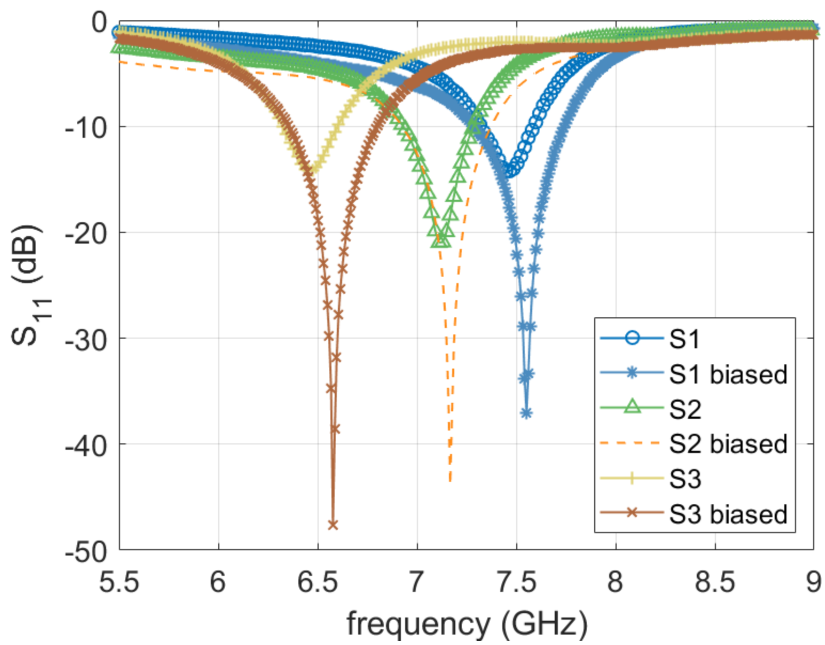

Figure 5.11: Comparison of the measured S_{11} of the magnetic films loaded antennas under self-biased and DC magnetic biased conditions.

Table 5.3: Measured performance metrics of the antenna samples in under self-biased and DC magnetic biased conditions (Date format: self-biased / DC magnetic biased).

Terms \ Samples	S1	S2	S3
Res. freq. f_r (GHz)	7.45/ 7.55	7.11/ 7.17	6.46/ 6.58
S_{11} (dB)	-14.2/ -37.1	-21.0/ -43.8	-14.2/ -47.6
BW (GHz)	0.27/ 0.45	0.36/ 0.45	0.28/ 0.45
FBW (BW/f_r)	3.6%/ 6.0%	5.1%/ 6.3%	4.3%/ 6.8 %
Max. r. gain (dBi)	7.2/ 7.0	5.4/ 4.6	5.1/ 2.4
Efficiency (self)	71.5%	52.3%	48.1%
Efficiency (DC)	65.6%	42.1%	25.0%

matching improvement completely, resulting in an overall negative effect to the antenna gain, which can be again explained by (5.13). Similar observation can be found for both S1 and S2. This is due to the DC magnetic bias excites the ferromagnetic resonance of the $NiFe_2O_4$ nanoparticles creating excessive magnetic loss of the magnetic film, such that part of the accepted power by the antenna was absorbed by the magnetic nanoparticles, instead of getting reflected back. Therefore, strictly speaking, applying DC magnetic bias does not essentially improve the physical impedance matching at the port of the antenna; but rather,

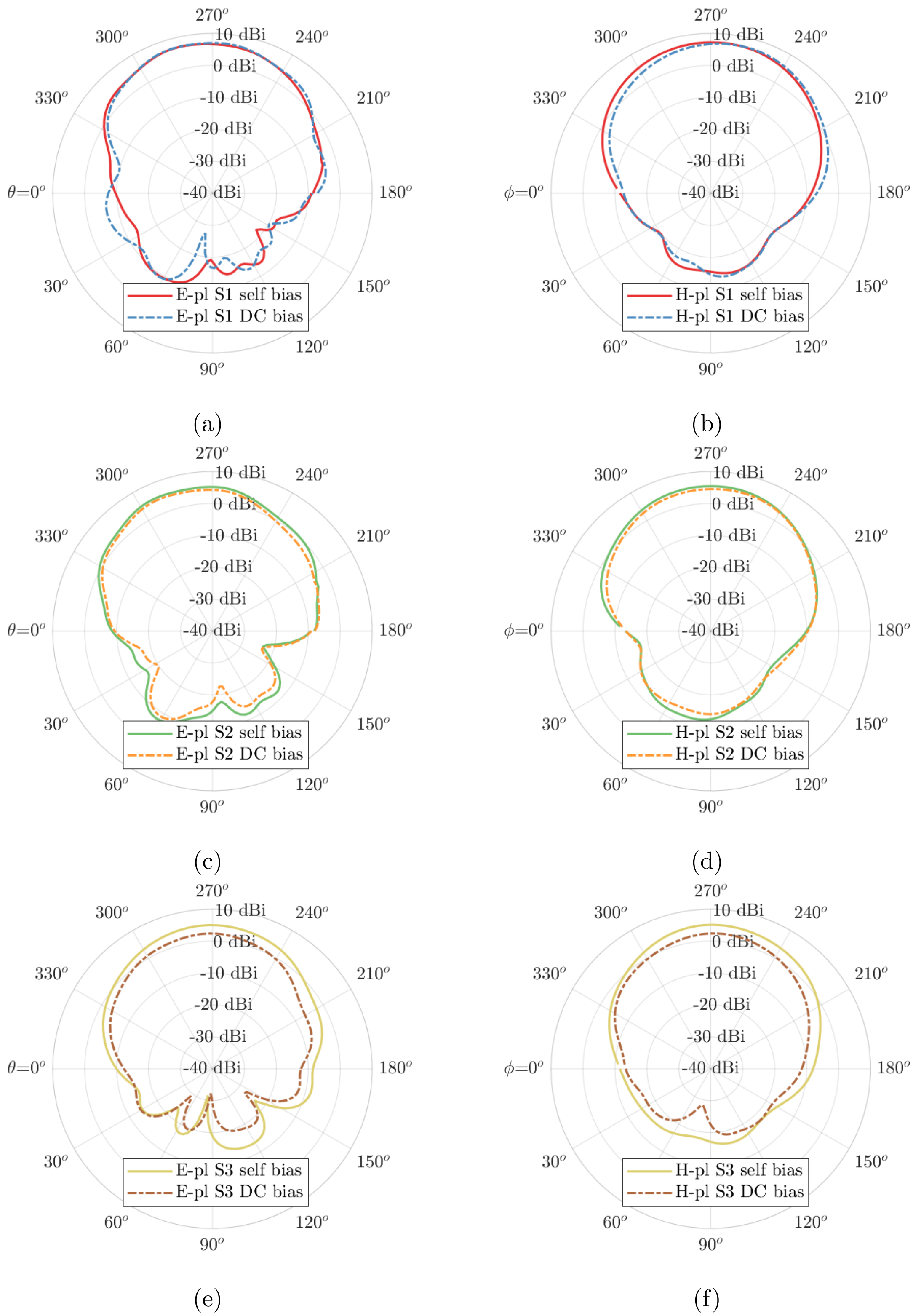

Figure 5.12: The measured E and H planes radiation patterns of sample S1, S2 and S3 under self-biased and DC magnetic biased conditions. S1:(a)(b), S2:(c)(d), S3:(e)(f).

raises the magnetic loss of the magnetic film which reduces the associated magnetic Q_m, causing the overall antenna efficiency to be degraded. Therefore, the more the efficiency is degraded, the stronger the magnetic loss is excited. Due to this increased lossy effect, the total antenna Q is reduced. Then given the relationship provided in (5.12), the bandwidth is thereby increased which is what we see from the measurement results.

Furthermore, since we know higher susceptibility of the magnetic film gives rise to stronger FMR effect, which in turn is determined by the film thickness and especially the fill factor of the film; thus based on our experiment results we can conclude that not only the film thicknesses follows the order S3–S1 from the most to the least, but also the fill factors spans from the highest to the lowest.

With the above knowledge, we know that the antenna efficiency can be enhanced using the air substrate configuration and the antenna can be miniaturized by loading the magnetic film within the air substrate to obtain much more compact package compared to the traditional superstrate loading approach, while bandwidth and impedance matching can be improved. Tradeoff is expected between the antenna miniaturization level and antenna efficiency; however, by carefully choosing the magnetic film thickness and improving the film quality, one can obtain both improved efficiency and realized gain. By applying the DC magnetic bias, the antenna performance can be affected, noticeably, the degraded radiation efficiency and realized gain. However, for applications which requires significant loss characteristics instead of radiation at certain frequency, e.g. filters, the magnetic loss from self-biased and DC magnetic biased conditions are actually advantageous.

5.4 Summary

In this chapter, we designed, fabricated and measured the antennas on the compact $NiFe_2O_4$ nanoparticle films loaded air substrates. First, we analyzed the efficiency improvement provided by the antenna on air substrate configuration, and further discussed the antenna on magnetic film loaded air substrate configuration in terms of antenna miniaturization, radiation efficiency, bandwidth and several other performance metrics. Then we used 3D printing technology and efficient chemical synthesis methods to fabricate antenna samples of both configurations with a compact, low cost, and light-weight package. All four antenna samples were measured, especially the magnetic films loaded antennas were tested in both self-biased and DC magnetic biased conditions to further investigate the antenna performance. The measurement results show very good antenna performance and were analyzed theoretically to gain additional insightful understanding, which provides a useful guide to using such magnetic material and configurations to design miniaturized RF and microwave applications with enhanced performance.

CHAPTER 6

TUNABLE BANDSTOP FILTER ON NANOMAGNETIC THIN FILMS

With the rapid development of the wireless communication technologies, the RF bandwidth scarcity problem is becoming more critical. On the other hand, to better utilize the already crowded frequency spectrum, one of the promising methods is to use frequency-tunable microwave devices. On the other hand, the widespread usage of wireless devices poses serious RF interference problems such that the unwanted signals in a specific frequency range have to be suppressed. This can be done generally by bandpass filters, however, in some cases when the interference signal is particularly strong or a limited number of close frequencies have to be kept apart, one or more bandstop filters will be more efficient than a bandpass filter which discriminates against all frequencies outside the pass band [58]. Therefore, the demand for broadband tunability, low cost and compact bandstop filters (BSFs) has been continuously increasing in modern wireless communication and radar systems.

Traditionally, research on technologies in achieving filter tunability were mainly done on the bandpass filters, which includes electronic tuning through microelectromechanic system varactors or ferroelectric varactors [59][60], mechanical tuning by piezoelectric-transducer controlling[61], magnetoelectric coupling based E- and H-field tuning [62], and magnetic tuning using ferrite based thin film/slab loaded filters [4][63][64]. Among the above four categories, the magnetically tunable filter is attractive because of its compactness, low cost and fast tuning mechanism. Most recently, in [65], a slim ribbon shaped BSF integrated with a 240 μm thick $FeGaB/Al_2O_3$ multilayer film was proposed showing a good tunability of 3.5 GHz by applying a rather modest magnetic bias field less than 400 Oe, and the stopband rejection was over 28 dB with a 3 dB in band reflection loss.

In this section, a microstrip BSF was first fabricated through a low cost thin film and lego-like process as shown in [29][66]. The very low loss air substrate contributes to a 41 dB insertion loss at 8.5 GHz and a 1 dB in band reflection loss. Using the low cost Solution Cast method, various types of magnetic material nanoparticles-$MnFe_2O_4$, $ZnFe_2O_4$, $NiFe_2O_4$, and half-half $NiFe_2O_4$ and $ZnFe_2O_4$ mixed-were deposited within the air cavity to form the magnetic film loaded air substrate. Due to the flexibility of the 3D printing technology, the magnetic film thickness can be controlled, such that the fabricated film thickness ranges from 30 μm to 100 μm, which gave the corresponding self-resonances of the film integrated BSFs from 7.6 GHz to 8.3 GHz. Moreover, by applying a vertical DC magnetic bias of 2500 Oe, we can observe a frequency shift effect, for example from 7.6 GHz to 9.1 GHz. The proposed magnetic film integrated BSF demonstrates not only good in band insertion and reflection loss by taking advantage of the 3D printed air substrate, but also a very compact size for working on multiple frequencies. Therefore, this process shows a great deal of potential for the fabrication of low cost and compact magnetically tunable microwave devices such as filters, resonators and antennas.

6.1 Magnetic nanoparticles properties and bandstop filter design

6.1.1 Magnetic Nanoparticles Properties

It is known that the unique non-linear property of the magnetic materials can be attributed to the Ferromagnetic Resonance (FMR) phenomenon, which represents the absorption frequency of a magnetic material to certain electromagnetic waves. in [67], the small signal theory of FMR was developed. This intrinsic property gives rise to the use of magnetic materials in many tunable and frequency selective microwave devices. Note that different types of magnetic materials may display a distinct FMR effect which is due to the magnetic susceptibilities of the materials. Since FMR is really an excitation of the nanoparticles between two energy states, with a higher magnetic susceptibility, the degree of magnetization would be larger in response to an applied magnetic field, and thus cause a larger energy difference between two energy states. In this work various magnetic nanoparticles—$MnFe_2O_4$, $NiFe_2O_4$, and $ZnFe_2O_4$—were studied for their FMR properties by carrying out the Electron Paramagnetic Resonance (EPR) measurement. For example, Fig. 6.1 shows the FMR absorption files of $MnFe_2O_4$ nanoparticles with particle size of 6 nm and 7 nm [46]. At 9.88 GHz, the FMR of the $MnFe_2O_4$ nanoparticles film appears around 3300 Gauss of EPR field, and exhibits a 1400 Gauss of linewidth. Similar FMR profiles were obtained for $NiFe_2O_4$ and $ZnFe_2O_4$ nanoparticles, and the FMRs were around 3200 Gauss and 3400 Gauss with a linewidth of 850 Gauss and 1000 Gauss respectively. The relatively narrow linewidth implies these magnetic materials have good potential in RF applications.

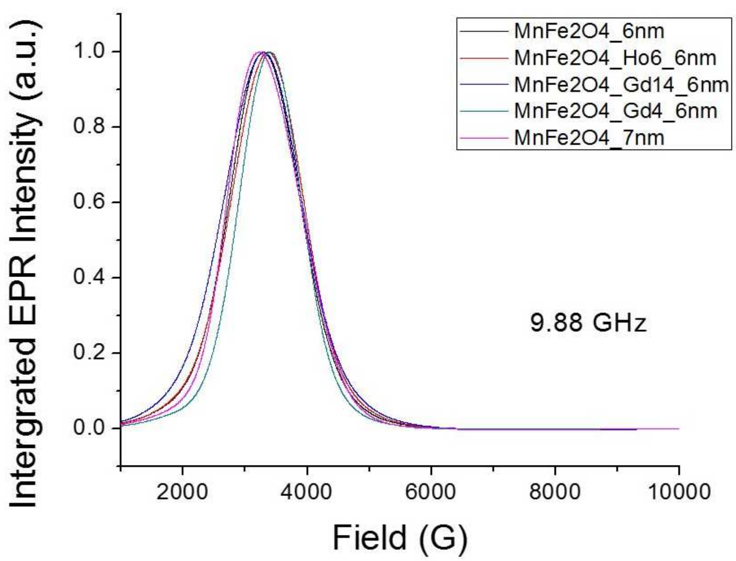

Figure 6.1: Selected FMR absorption profiles of $MnFe_2O_4$ nanoparticles [?].

6.1.2 Bandstop Filter Design

The BSF is designed to operate at the center frequency of 8.5 GHz with a 3 GHz bandwidth, and to have a rejection level higher than 30 dB at the center frequency. It is implemented using the microstrip open-circuited stubs and is optimized by incorporating the redundant unit elements in the design, so that a wide stopband and steeper rejection characteristics can be obtained [68]. Then we take advantage of the 3D printing technology to create a low loss air substrate such that the filter is suspended above the ground plane to minimize the in band reflection loss of the BSF. The 3D printed lego-like structure facilitates the filter assembly. Moreover, compared to the separate film fabrication and post film-filter integration in [63], we can directly deposit the magnetic nanoparticles within the air cavity to form the magnetic film, so that the film is integrated simultaneously as a magnetic film loaded air substrate. In [63], the yttrium iron garnet (YIG) material was either deposited on the gadolinium gallium garnet (GGG) substrate or sandwiched between two GGG substrates to fabricate a stand-alone magnetic film; then the film was flipped on top of the filter surface as a superstrate to enable magnetic tuning, and additional clamping structures maybe needed for mechanical stability. Fig.6.2 illustrates the topology and design parameters of the BSF. The detailed assembly and film fabrication will be discussed in Section III.

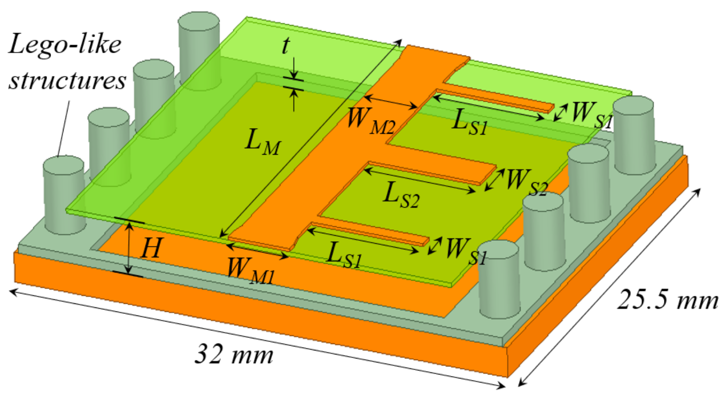

Figure 6.2: The design of the BSF on the air substrate: $L_M = 25.5$ mm, $W_{M1} = 4$ mm, $W_{M2} = 3.6$ mm, $L_{S1} = 7.3$ mm, $W_{S1} = 0.8$ mm, $L_{S2} = 7.2$ mm, $W_{S2} = 2.3$ mm, $H = 1$ mm, $t = 120$ µm - 300 µm.

6.2 Magnetic Films and Filter Fabrication

6.2.1 Magnetic Film Loaded Air Cavity Fabrication

A square well with a certain depth of either 30 µm or 100 µm was 3D printed on top of the copper sheet creating an air cavity, as shown in Fig. 6.3a. A photopolymer resin material called *VeroWhitePlus* and a commercially available Connex Objet350 3D printer , which features a resolution of 100 µm in the X/Y axes and 30 µm in Z axis [**?**], were used.

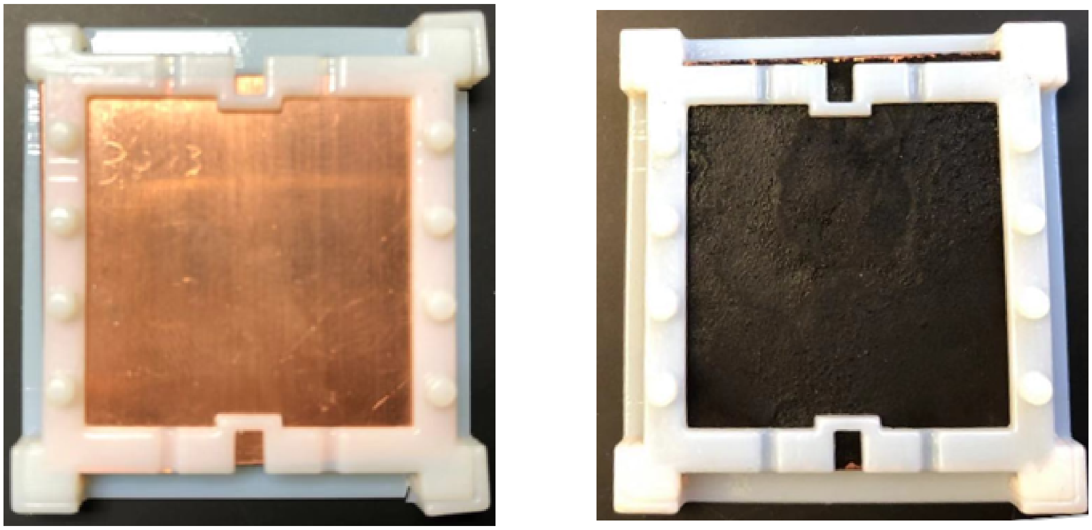

(a) (b)

Figure 6.3: Fabricated sample: (a) 3D printed air cavity on the copper sheet; (b) 100 μm thick $MnFe_2O_4$ film loaded air cavities.

In the next step one of the following magnetic nanoparticles: $MnFe_2O_4$, $NiFe_2O_4$, $ZnFe_2O_4$, and half-half mixed $NiFe_2O_4$ and $ZnFe_2O_4$, were deposited within the cavity through the SC method. Specifically, the nanoparticles were first surface treated using (3-glycidyloxypropyl)-trimethoxysilane ethanol solution, and were then collected through a magnet to mix with 10-20% (w/w) poly(methyl methacrylate) PMMA and an appropriate amount of dichloromethane. This nanoparticle based solution was applied evenly within the cavity by a syringe. After it was air-dried and stored in a desiccator, a layer of Torlon TF4000 polymer was spin-coated onto the surface to both chemically and physically protect and stabilize the underlying film. Note that by controlling the depth of the 3D printed cavity, we can have the film in a variety of thicknesses; here we have 30 μm and 100 μm. The size of the magnetic nanoparticles can be also controlled through managing either time or temperature of the reaction solution. Fig. 6.3b shows a fabricated $MnFe_2O_4$ film loaded air cavity which has a film thickness of 100 μm.

6.2.2 Bandstop Filter Assembly

The microstrip BSF design as shown in Fig. 6.2 was patterned on top of a Rogers Ultralam 3850HT LCP substrate through photolithography. The LCP substrate has a dielectric constant of 3.14, a loss tangent is 0.002 [**?**], and the thickness is chosen as 2 mil to minimize the dielectric loss. We also 3D printed two other auxiliary structures *A1* and *A2* for the following two purposes: (1) Evenly stretch and mechanically stabilize the LCP on top of the film loaded air cavity; (2) Facilitate the RF connector assembly for the filter. Finally, through the lego-like process shown in Fig. 6.4a, we can achieve an air suspended BSF loaded with the magnetic film where the air substrate is 1 mm thick. Due to the fact that the thickness of the LCP is only 2 mil, which is very thin compared to that of the air substrate, the effective dielectric constant of the air substrate is slightly larger than 1. Fig. 6.4b which shows the fully assembled BSF with two SMA connectors that is ready for measurement.

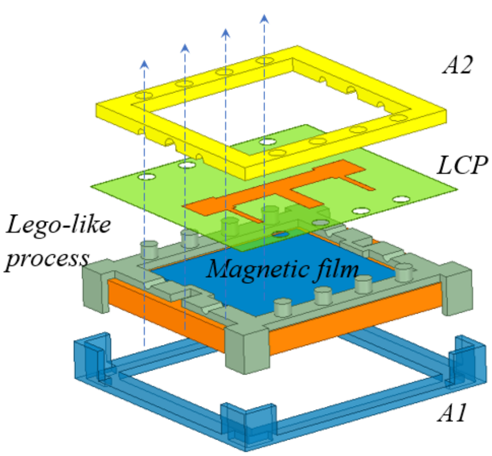

(a)

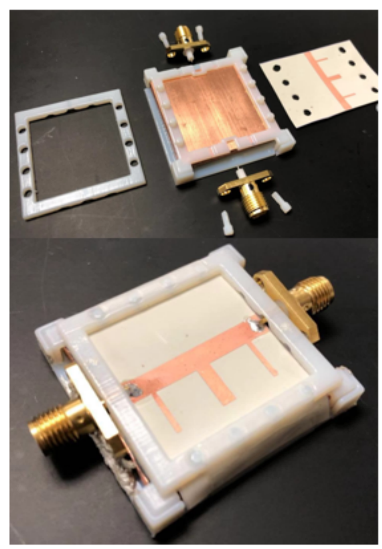

(b)

Figure 6.4: Fabricated sample: (a) The lego-like assembly process; (b) Fully assembled microstrip BSF.

6.3 Filter Measurements and Discussions

The S-parameters of the filters were measured using a Keysight N5227A Performance Network Analyzer which was calibrated with the SOLT method up to the RF connectors. The

S_{21} and S_{11} denote the insertion and the reflection loss of the filter, respectively, and are shown in Fig. 6.5a - 6.5b. For the non-magnetic film loaded air substrate BSF, both the measured insertion and reflection loss agree with the simulations. Due to the low loss nature of the air substrate, we can see the steep rejection characteristic with 41.1 dB of insertion loss at 8.5 GHz, and the minimum 1.6 dB of in band reflection loss. Also, the out-of-band insertion loss can be as low as 0.33 dB and the reflection loss is better than 12 dB. When loaded with the magnetic films, the self-resonances of the filters shift downward which can be as low as 7.6 GHz which corresponds to 0.9 GHz of frequency shift due to the 30 μm $ZnFe_2O_4$ film. Similar results can be obtained for the other films. In addition, we can observe that for all the magnetic film loaded cases, the inband insertion loss is higher than 30 dB, and the reflection loss can be as good as 0.7 dB. The out-of-band insertion and reflection loss are also very good. This frequency shift effect due to the magnetic film loading is because the magnetic film has a relative permeability $\mu_r > 1$, which serves as a perturbation to the air substrate. The electromagnetic wavelength $\lambda = \frac{1}{f\sqrt{\epsilon_r \mu_r}}$ at a fixed frequency in the air substrate reduces when loaded with the magnetic film, causing the filter to be electrically larger. Therefore, the center frequency of the magnetic film loaded BSF shifts lower. Moreover, we notice that the frequency shifts of both the 30 μm $ZnFe_2O_4$ and $NiFe_2O_4$ films are very close to that of the 100 μm $MnFe_2O_4$ film. This indicates that the $ZnFe_2O_4$ and $NiFe_2O_4$ nanoparticles have higher magnetic susceptibilities than the same amount of $MnFe_2O_4$ nanoparticles. The above results imply that we can miniaturize such BSF or other circuits on the similar air substrate package that is operating at a fixed frequency by just loading the magnetic films; and the thicker the magnetic films or the higher magnetic susceptibility of the nanoparticles, the smaller the filter size. Again, because the magnetic film is simply integrated with the substrate and the film thickness can be easily controlled by the 3D printed air cavity, the overall package of the BSF is very compact and the fabrication is very low cost.

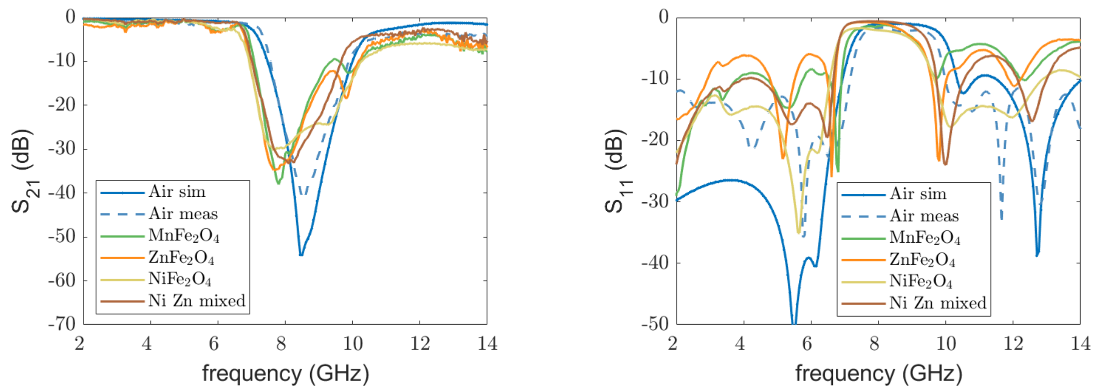

(a) (b)

Figure 6.5: Measured (a) insertion loss and (b) return loss of the films and non-films loaded BSF. The corresponding film thicknesses t of $MnFe_2O_4$, $NiFe_2O_4$, $ZnnFe_2O_4$ and half-half mixed $NiFe_2O_4$ and $ZnnFe_2O_4$films are 100 μm, 30μm, 30 μm, and 30μm.

To further explore the effect of the loaded magnetic films in terms of the material types and film thicknesses, we applied an external DC magnetic bias field of 2500 Oe to the filter. The DC magnetic bias was applied vertically to the plane of the film loaded filter by placing the filter between the two poles of the electromagnets. The results are shown in Fig. 6.6a - 6.6d. A shift of the operation frequency can be observed in all four film cases. For example in Fig. 6.6a, the stopband center frequency of the $MnFe_2O_4$ film case increased from 7.8 GHz to 8.7 GHz when 2500 Oe of the magnetic bias was applied, while the 10 dB bandwidth shrinks from 3.3 GHz to 2.5 GHz. Similar results can be observed for the $NiFe_2O_4$ film case. While keeping the same film thickness of 30 μm, $NiFe_2O_4$ films resulted in even larger resonant frequency shift of 1.5 GHz (from 7.6 GHz to 9.1 GHz) at 2500 Oe of DC magnetic bias, as we can see from Fig. 6.6e. This is due to the higher magnetic susceptibility in $NiFe_2O_4$ nanoparticles, which implies that a smaller magnetic bias field is needed for the same amount of tuning when compared to the other films. We can also see that the rejection at the center resonance increases with the magnetic bias strength for $NiFe_2O_4$ and the mixed films; however it remains relatively unchanged for the $MnFe_2O_4$ and $ZnFe_2O_4$ films. For instance in Fig. 6.6e, the rejection at the resonant frequency increases from 30 dB to 46 dB as the magnetic bias is at 2500 Oe. This again is due to the larger magnetization saturation of the $NiFe_2O_4$ nanoparticles. Table 6.1 provides the comparison of the center resonant frequency, the rejection at the center resonant frequency, the 10 dB bandwidth, and the magnetic film thicknesses of the BSF before and after applying the 2500 Oe of the magnetic bias.

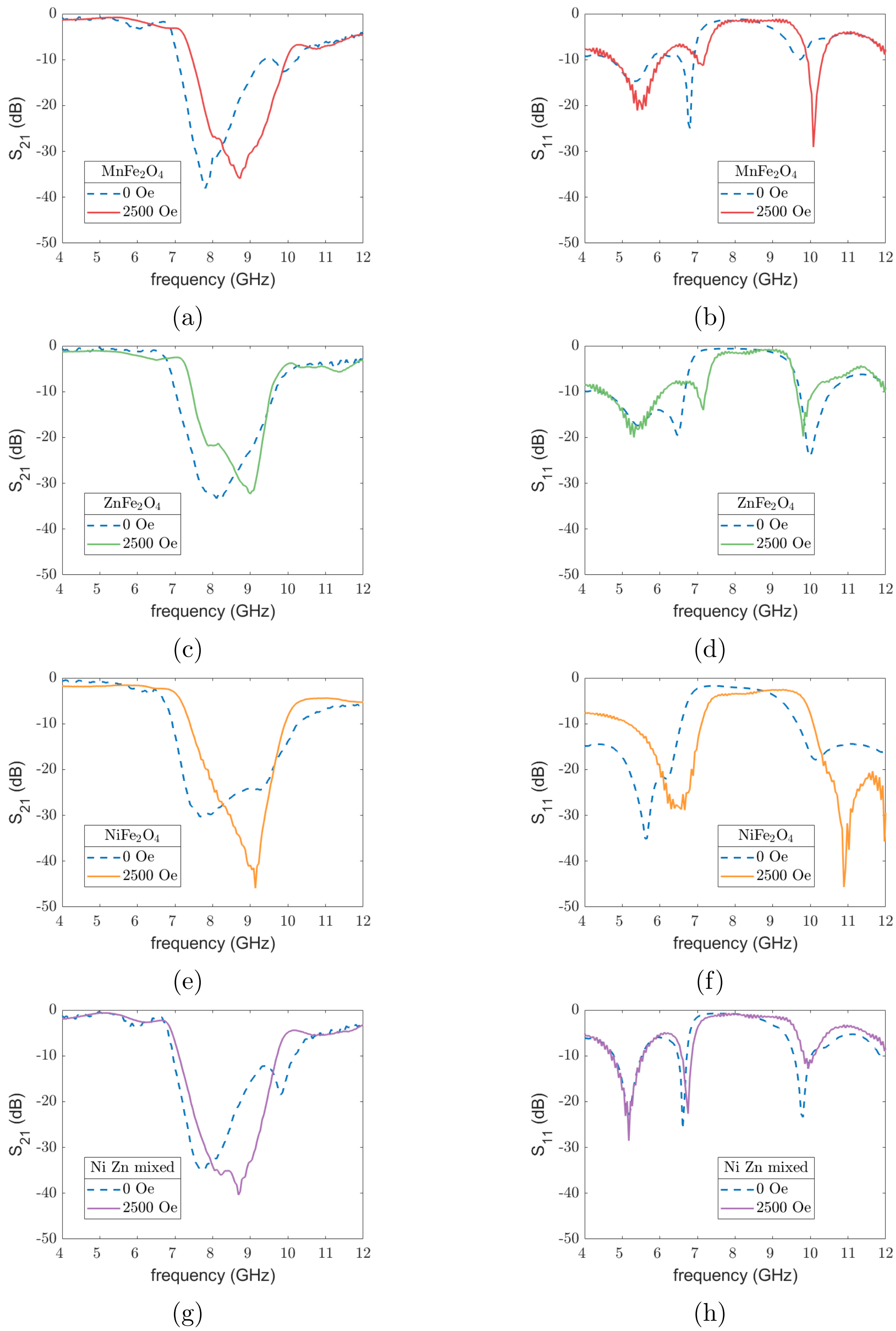

Figure 6.6: Measured insertion loss and reflection loss of all four film cases under the DC magnetic bias of 2500 Oe.

Table 6.1: Performance metrics of the BSF before and after applying the 2500 Oe of magnetic bias (Data format: before/after).

Films / Terms	$MnFe_2O_4$	$ZnFe_2O_4$	$NiFe_2O_4$	Mixed
Ctr.freq (GHz)	7.8/8.7	8.1/9	7.6/9.1	7.6/8.7
Rej.level (dB)	38/36	33/32	30/46	35/40
BW (GHz)	3.1/2.5	2.7/2.1	3.3/2.5	3.3/2.6
Film thickness	100 µm	30 µm	30 µm	30 µm

6.4 Summary

In this Chapter a magnetic film loaded microstrip BSF was developed and characterized. Various types of magnetic films with different thicknesses were deposited within a 3D printed cavity well using the low cost SC method. The self resonances of the magnetic films loaded BSFs ranges from 7.6 GHz to 8.3 GHz. In addition, by applying a vertical DC magnetic bias of 2500 Oe, the $NiFe_2O_4$ film loaded BSF exhibits a center frequency shift of 1.5 GHz, as well as 16 dB more rejection at the center frequency. This work demonstrated a low cost and compact magnetically tunable BSF which has good potential in RF and microwave applications.

CHAPTER 7

TUNABLE SPHERICAL CAVITY RESONATOR USING MAGNETIC FILM

Tunable resonators are attractive due to the performance agility to meet different regional industry standards which makes it a key role in RF front ends. Traditionally, most of the tunable resonators were developed to be electronically tunable based on RF MEMS or ferroelectric tuned elements [70]–[71], which are usually difficult and expensive to fabricate. Recently, the authors in [72] proposed a magnetically tunable ferrite slab loaded substrate integrated waveguide cavity resonator which achieved a tuning range of more than 6% and an unloaded Q (quality factor) more than 200. Such tuning often requires an external magnetic bias circuitry which makes the system large and complex. And the above tunable resonators usually have relatively large tuning step which is ineffective when fine tuning is desired. Lately, a spherical cavity resonator was demonstrated to have an unloaded Q of 3728 using 3D printing technology [73]. Thus, it is possible to develop high Q fine–tunable resonator with cost effective fabrication process and simple topology.

In this paper, a 3D printed X-band spherical cavity resonator with very fine tuning using a magnetic nanoparticle film is proposed and characterized for the first time. The polyjet 3D printing technology facilitates the fabrication of light-weight spherical cavity assemblies for tuning. A magnetic nanoparticle film deposited on a LCP host substrate is placed at the center of the 3D printed cavity where the magnetic fields are the strongest. By mechanically rotating the films the resonant frequency can be tuned accordingly due to the perturbed magnetic fields. The measurement results show a frequency tuning range of 70 MHz with the average and minimum tuning step of 11.7 MHz and 4.4 MHz, respectively. The corresponding unloaded quality factors ranges from 539 to 732, which is at the expense of a narrow tuning range. However, the tuning range can be increased by improving the magnetic nanoparticle fill factor in the film and choosing a ferrite material with a higher

μ_r. This work shows a cost effective and light-weight high Q spherical cavity resonator with very fine tuning based on a simple design, which can be used in designing high performance filters and other microwave structures.

7.1 Tunable Resonator Design and Theoretical Analysis

7.1.1 Spherical Cavity Resonator Design And Mode Analysis

The spherical cavity is known for its extremely high Q compared to its rectangular and cylindrical counterparts, as it does not posses any sharp corners or edges, thus its volume and surface area are better utilized by the interior fields. Depending on the orientation of the designated coordinate system, the field configuration can be treated as TE^r and/or TM^r mode; and based on the field distributions, the exact mode can be determined. The resonant frequency of the lowest-order TM$^r_{m11}$ mode of the air-filled spherical cavity as shown in Fig. 7.1 can be found as [74]:

$$(f_r)^{TM^r}_{m11} = \frac{\zeta'_{11}}{2\pi R\sqrt{\mu\epsilon}}, \quad m = 0 \; or \; 1 \tag{7.1}$$

where $R = 16$ mm, $\zeta'_{11} = 2.744$, $\mu = 4\pi \times 10^{-7}$ H/m, and $\epsilon = 1/(36\pi) \times 10^{-9}$ F/m, which yields $(f_r)^{TM^r}_{011} = (f_r)^{TM^r}_{111}(\text{even}) = (f_r)^{TM^r}_{111}(\text{odd}) = 8.18$ GHz, corresponding to three degenerate modes. Thus the first step is to determine which mode(s) is (are) excited specifically.

The spherical cavity is designed to be electrically excited by two probes oriented along the Z axis, as indicated in Fig. 7.1. We can thereby plot the magnitude of the total H (magnetic) field in the XY plane as shown in Fig. 5.2a. It can be seen that the total H field is symmetrical which is invariant of the azimuth angle ϕ. By examining all the H components (r, θ, ϕ) of three degeneracies and letting the elevation angle $\theta = 90°$, we find out that the observed H field distribution corresponds solely to the H_ϕ component of TM$^r_{011}$ mode, which we can conclude is the only excited mode within the spherical cavity. To verify

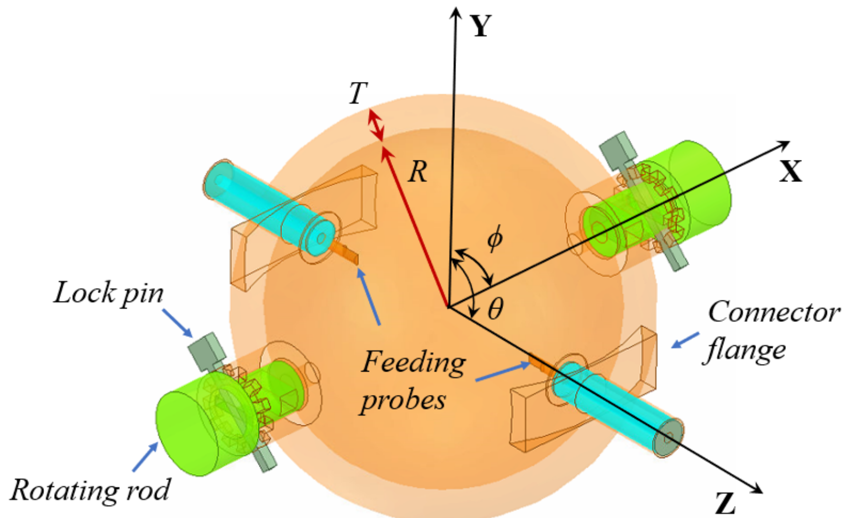

Figure 7.1: The electrically excited air-filled cavity resonator with rotating rods (magnetic film is not shown for clarity). $R = 16$ mm, $T = 3$ mm.

the above conclusion, the H_ϕ component of TM^r_{011} mode can be written as [74]:

$$H_\phi = \frac{C}{\mu\, r} \hat{J}_1 \left(2.744 \frac{r}{R}\right) \sin\theta \tag{7.2}$$

where C is constant, r is the radial coordinate of the spherical cavity. Since $H_r = H_\theta = 0$ for the TM^r_{011} mode, therefore in the XY plane where $\theta = 90°$, the total magnetic field is $H_{total} = H_\phi = \frac{C}{\mu r} \hat{J}_1 \left(2.744 \frac{r}{R}\right)$, which shows that the magnitude of the total H field in the XY plane is independent of ϕ and varies with r following the special spherical Bessel function $\hat{J}_1(2.744 \frac{r}{R})$, as can be seen from Fig. 5.2b. This mode analysis lays the foundation of implementing the magnetic tuning mechanism, as shown in the next section.

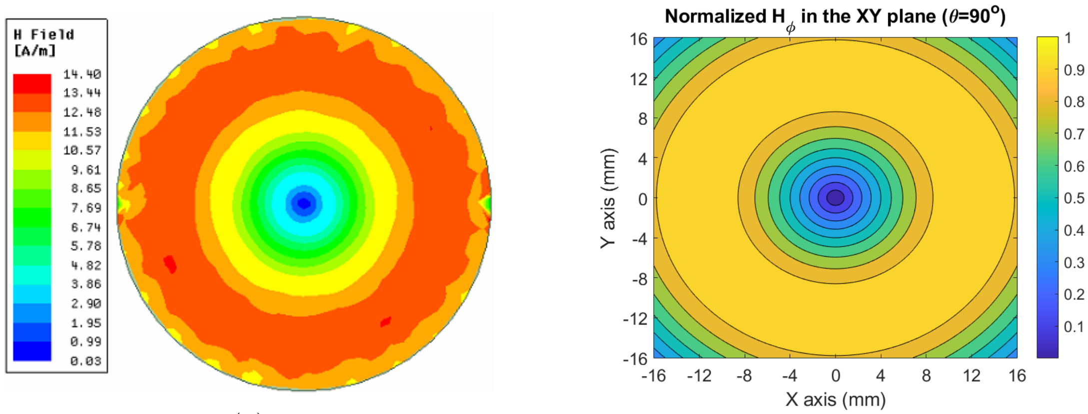

(a)

(b)

Figure 7.2: Magnetic field distributions in the XY plane: (a) simulated total magnetic filed; (b) normalized theoretical H_ϕ using (7.2).

7.1.2 Tunable Resonator Design

The perturbation theory states that the resonant frequency of the cavity can be decreased by increases in the permittivity ϵ and permeability μ of the filled material which interacts with the internal fields [75]. Hence, the frequency tuning in this work is achieved through perturbing the H field inside the cavity using the magnetic film.

As shown in Fig. 7.2a and (7.2), the total H field of the dominant TM^r_{011} has the maximum value in the XY plane, thus the magnetic film will result in the most resonant frequency tuning effect when it is placed in the XY plane. Moreover, the planar shape and size of the magnetic film, as well as the film thickness also determine the tuning range. Obviously, a circular shaped magnetic film will have the strongest tuning effect compared to other planar shaped films, as it has the full interaction with the total H field in the XY plane.

In practice, given the fabrication limitation, a rectangular magnetic film is suspended in the XY plane ($\theta = 90°$) by adhering to the ends of two dielectric rods protruding from the cavity, as shown in Fig. 7.1. By mechanically rotating the rods along the X axis, the magnetic film is rotated in an angle of θ with respect to Z axis. In this case, the magnetic film has less interaction with the H field whose strength is also decreased with smaller θ.

Therefore, the resonant frequency is tuned accordingly with the rotation of the film, and the very fine tuning step can be achieved by accurately controlling the rotation angle θ, whereas the tuning range is dictated by the geometric and magnetic properties of the nanoparticle film. Note that the mechanical tuning range is restricted by $\theta \in [0°, 90°]$, as the H_ϕ in (7.2) varies sinusoidally with respect to θ given a fixed r, such that the frequency tuning dynamic repeats in a period of 90°.

7.2 Resonator Fabrication Process

7.2.1 Magnetic Film Deposition And Characteristics

Using a cost effective Solution Cast chemical method in [46], the magnetic films made of $NiFe_2O_4$ nanoparticles are fabricated on a 25 mm × 15 mm × 2 mil rectangular LCP host substrate, as shown in the inset of Fig. 7.3. The measured average film surface roughness is 1.5 μm. By measuring the difference between the film and LCP surface, the film thickness is estimated to be 35 μm, as indicated in Fig. 7.3.

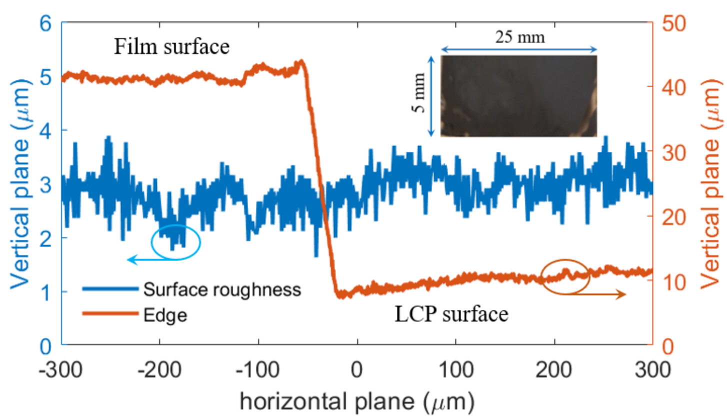

Figure 7.3: Measured film surface roughness and edge profile. Inset: fabricated $NiFe_2O_4$ film on a 2 mil LCP host substrate.

7.2.2 Resonator Fabrication And Assembly

Two hemispherical resonator parts are 3D printed using a photopolymer resin material called *VeroWhitePlus* and a commercially available Connex Objet350 polyjet printer, which has a resolution of 100 μm in the X/Y axes and 35 μm in Z axis [66]. Then the inner surfaces of the cavities are metalized with a layer of 15 μm thick copper using electroplating, as shown in Fig. 7.4a. The 3 mm thick cavity wall helps the cavity to remain mechanically in shape during the metalization process. In addition, as mentioned earlier, two 3D printed dielectric rods are used to suspend and rotate the film to achieve the frequency tuning. Note the magnetic film is adhered to the ends of the rods using two 1 mm $\times$ 1 mm tapes. The two cavity parts are then assembled through a lego-like process. An amount of silver epoxy is applied to the interfaces of the two hemispherical parts to ensure reliable electrical connection, and two SMA connectors are used to characterize the cavity. The whole package as depicted in Fig. 7.4b is 60 g in total weight, which is very light-weight.

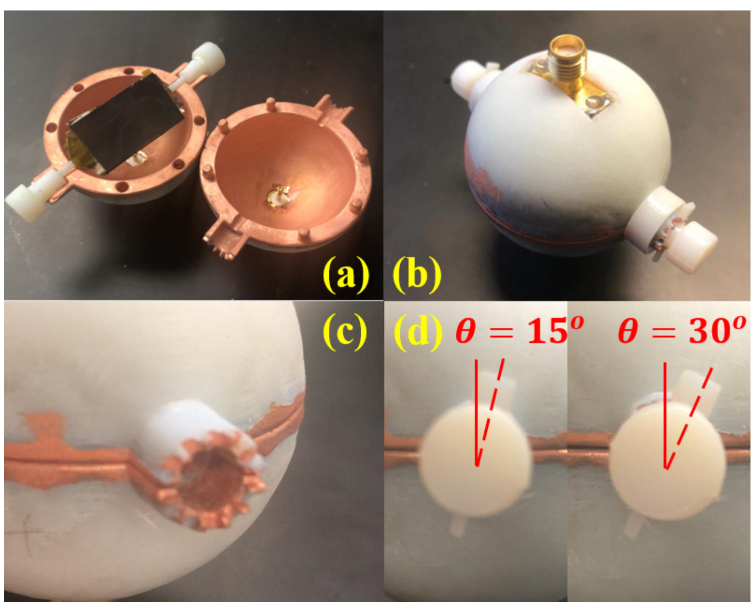

Figure 7.4: Fabricated samples: (a) metalized cavity parts with magnetic film placed: (b) fully assembled cavity resonator; (c) enlarged picture of corrugated rod sleeve; (d) rotation position at $\theta = 15^\circ$ and $\theta = 30^\circ$.

In order to precisely rotate the film, a corrugated rod sleeve with a rotation lock pin is designed, as displayed in Fig. 7.4c–d. The corrugated sleeve has 24 evenly spaced slots on the circumference, which gives 15° per slot. For each rotation, a lock pin is used to pass through the slot and the hole in the rod to stabilize the film. Fig. 7.4d shows the film is rotated at $\theta = 15°$ and 30°, respectively.

7.3 Results and Analysis

The S-parameters of the cavity resonator are measured using a Keysight N5227A Performance Network Analyzer which is calibrated with the SOLT method up to the SMA connectors. From Fig. 7.5 we can observe that the measured S parameters matches very well with the simulated results for the air-filled cavity resonators. The measured resonance at 8.05 GHz has a S_{11}=-24.2 dB and S_{21}=-0.71 dB, which is slightly different from the corresponding simulated results of 8.06 GHz resonant frequency with S_{11}=-22.7 dB and S_{21}=-0.14 dB. The minor difference is due to the cavity surface roughness, and mainly due to the resistance of the solder applied at the conjunction of the probe and the inner cavity surface. This resistance is estimated to be 14.5 Ω by simulating the solder ring as shown in the inset of Fig. 7.5, such that the simulated S_{21} and S_{11} at 8.05 GHz are -0.71 dB and -23.3 dB, respectively, which matches closely with the measured results.

The measured results of the tunable resonator are shown in Fig. 6, where the film is rotated by $\theta \in [0°, 90°]$ per 15°. The simulation with the same film size and $\mu_r = 15$ was carried out using HFSS. The plot is not shown for clarity and the key simulated data are provided in the following discussion. From Fig. 6, We can see the resonant frequency shifts downward with the increased rotation angle θ. When $\theta = 0°$, the resonant frequency is at 8.028 GHz which is 25 MHz lower than that of the air-filled cavity. This is because the 2 mil LCP has a dielectric constant of 3.14 [49], thus slightly perturbs the electrical field in the XZ plane ($\theta = 0°$) where the electrical field is maximum. As θ increases, large magnetic perturbation resulted from the magnetic film dominates, leading to a smaller resonant frequency. Particularly at $\theta = 90°$, the resonant frequency shifts down to 7.958 GHz which indicates

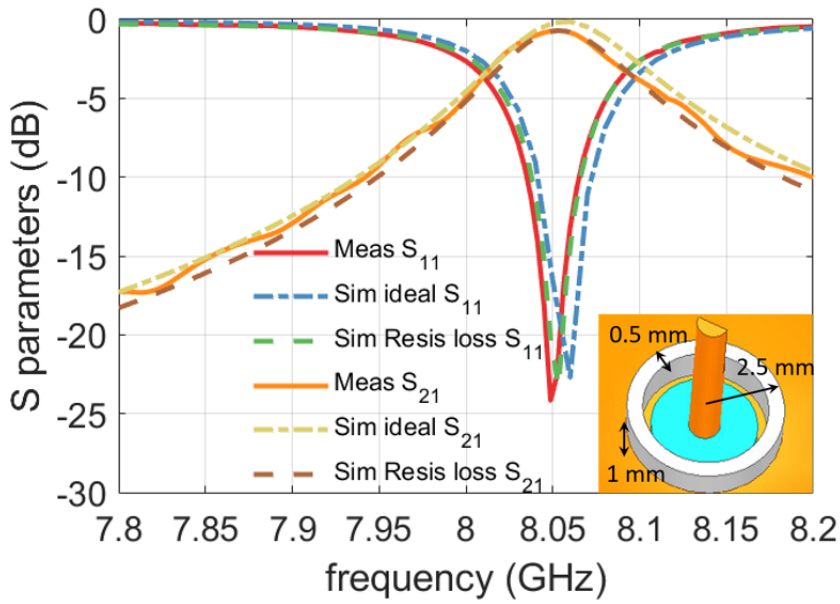

Figure 7.5: Measured and simulated S parameters of the air-filled cavity resonator. Sim ideal/resistive: without/with the resistive solder ring. The dimensions of the solder ring are shown in the inset.

the maximum magnetic perturbation effect is obtained. In addition, the maximum tuning step is 26.3 MHz when θ turns from 0° to 15°, whereas the minimum step is 4.4 MHz as θ increases from 75° to 90°. This can be attributed to the $\cos\theta$ dependence of the $\frac{\partial H_\phi}{\partial \theta}$ which can be derived from (7.2); as θ getting closer to 90°, the change of the H_ϕ becomes smaller, thus less perturbation is obtained, and vice versa. Fig. 7.7a shows that the trend of tuning step roughly follows the curve of $\cos\theta$. The difference is because the $\cos\theta$ dependence is given a circular shape film fully interacting with the H field. However, the rectangular film used here has less such interaction, thus smaller the tuning step change. While the measured tuning step matches with the simulation closely, the minor difference is due to the flexibility of the film and not being flat during the rotation.

In addition, we observe the second high resonance starts to appear when $\theta \in [15°, 75°]$, then disappear at $\theta = 90°$. This resonance becomes less obvious as θ becomes larger. This phenomenon is because of the disturbed coupling between the two excitation probes due to the rotation of the magnetic film which causes the excited wave travel through two different path resulting in two resonances; whereas at $\theta = 0°$ and 90°, probes are normally coupled so that the wave travels in a single patch and thus only the fundamental resonance is formed. Note that the small deterioration of S_{21} with the film loading compared to the air-filled case is due to the magnetic loss of the film.

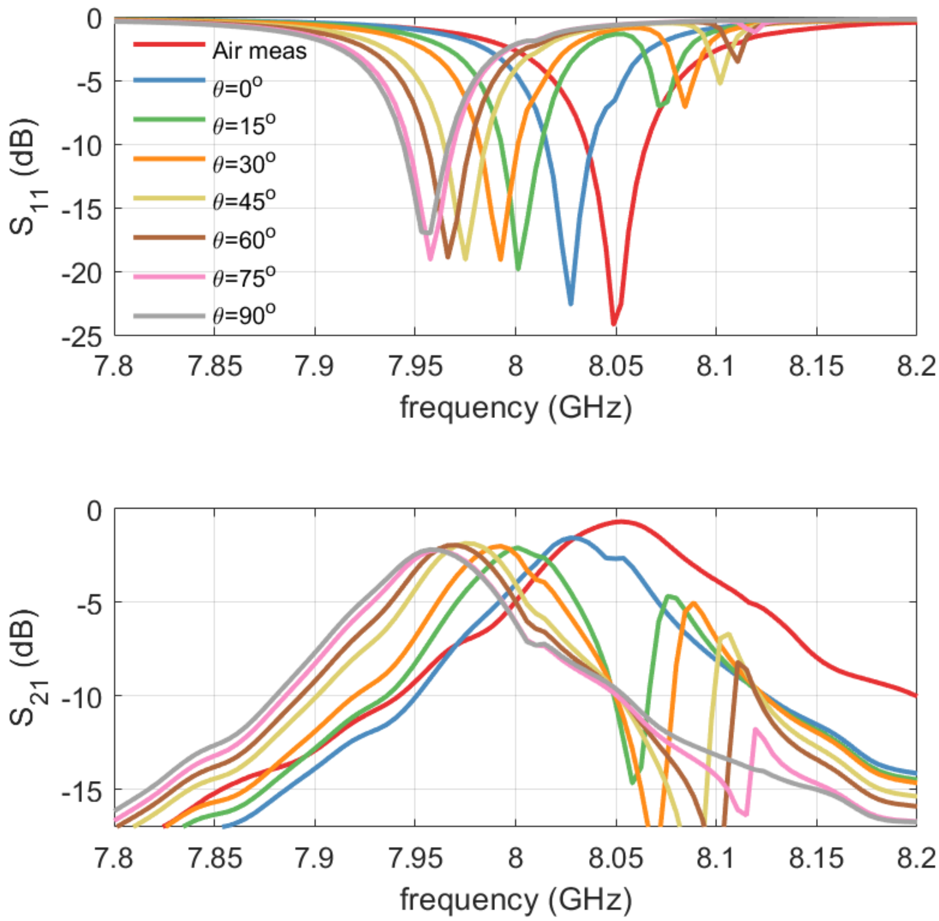

Figure 7.6: Measured S_{11} and S_{21} of 7 tuned resonances at the corresponding rotation angle θ compared to the air-filled case.

The unloaded quality factor Q_u of the cavity resonator can be calculated as [75]:

$$Q_u^{-1} = Q_L^{-1} - Q_e^{-1} \tag{7.3}$$

where the loaded quality factor Q_L and the external quality factor can be determined by [75]:

$$Q_L = \frac{f_r}{\Delta f_{3dB}} \quad and \quad Q_e = \frac{Q_L}{10^{S_{21}(dB)/20}} \tag{7.4}$$

where $S_{21}(dB)$ takes the value at the resonant frequency f_r. Fig. 7.7b shows the closely matched simulated and measured tuned resonant frequency f_r, and the measured Q_u is 83

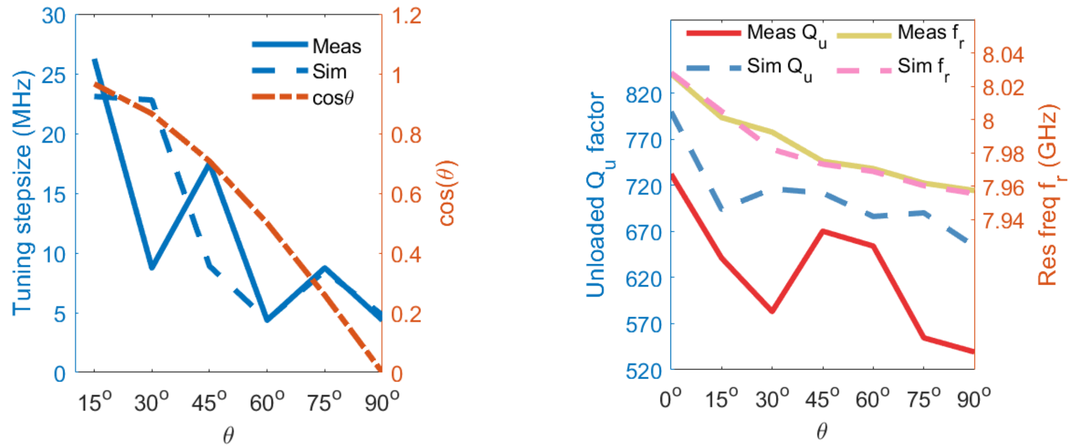

(a)

(b)

Figure 7.7: (a)Tuning step and $\cos\theta$ V.S. θ; (b) Q_u and f_r V.S. θ

in average less than the simulated values, which is due to the surface roughness and the magnetic loss of the film that are not considered in the simulation. The data of measured Q_u, f_r, and the S parameters of all tuning cases are included in Table 7.1. We observe that the air-filled cavity has a Q_u of 1188 which is slightly less than the simulated value of 1211 based on Fig. 7.5. As for the film loaded cavity, the Q_u has a maximum of 732 at $\theta = 0°$, and as θ increase, the film interacts more with the H field resulting in more energy loss from the film, therefore a reduced Q_u with a minimum of 539 at $\theta = 90°$. This trend of Q_u can be also observed from Fig. 7.7b. Note the above Q_us are not far away from those extracted from a weakly coupled such resonator (air: 1393, $\theta = 0°$: 764), which are not shown given the limited space. In addition, the Q_u can be further improved by polishing the 3D printed cavity surface [73] and reducing the magnetic film roughness loss.

Table 2 shows the state-of-the-art tunable and 3D printed resonators. We can see that the proposed resonator has a high Q and fine tuning step, which also eliminates the need for external biasing network. However, a rotor may be needed to mechanically rotate the film in real practice. The tuning range can be increased by improving the magnetic nanoparticle fill factor and choosing a higher μ_r ferrite material.

Table 7.1: Measured unloaded quality factors and S parameters at the resonances of the air-filled case and all tuning cases.

Metric	Air	$\theta = 0°$	$\theta = 15°$	$\theta = 30°$
Meas. Q	1188	732	641	583
f_r (GHz)	8.053	8.028	8.001	7.993
S_{21} / S_{11} (dB)	-0.7 / -19.4	-1.5 / -22.6	-2.0 / -19.8	-2.0 / -19.1
Metric	$\theta = 45°$	$\theta = 60°$	$\theta = 75°$	$\theta = 90°$
Meas. Q	670	654	555	539
f_r (GHz)	7.975	7.971	7.962	7.958
S_{21} / S_{11} (dB)	-1.9 / -19.1	-1.9 / -18.9	-2.1 / -19.1	-2.1 / -17.0
Max./min./average tuning step (MHz): 26.3 / 4.4 / 11.7				

Table 7.2: Comparison of the state-of-the-art tunable and 3D printed resonators.

Ref.	Type	Tunability	Bias	Q_u
[70]	RF MEMS	4–6 GHz 0.11 GHz step	0–50 V per switch	300–500
[72]	Ferrite loaded SIW	12.4–13.2 GHz 0.18 GHz step	0-0.45 T	289–360
[73]	3D printed sph. cavity	10.07 GHz Not for tuning	N.A.	3728
[66]	Rect. cavity w. tuning posts	8.21–10.12 GHz 0.53 GHz step	Not needed	72–391
This work	Sph. cavity w. mag. film	7.958–8.028 GHz 11.7 MHz step	Not needed	539–732

7.4 Summary

In this chapter, a tunable spherical cavity resonator is achieved by perturbing the magnetic field using a 35 μm $NiFe_2O_4$ magnetic film. The resonant frequency can be tuned from 7.958 GHz to 8.028 GHz, with the minimum and average tuning step of 4.4 MHz and 11.7 MHz. The measured Q_u ranges from 539–732. It demonstrates a light-weight and high Q cavity resonator with fine tuning based on a simple design and cost effective fabrication process.

CHAPTER 8
SUMMARY

In this work, the application of using additive manufacturing technology and magnetic nanomaterials in the RF devices and components is explored. First, several types of RF devices including filter, resonator, and antennas are fabricated using the polyjet or Aerosol jet printing technology, and the combined process. Good performances such as low insertion loss, wideband tunability, and high gain are achieved respectively, which shows the advantage of fabricating low cost and high performance RF and millimeter wave devices using additive manufacturing technology. Second, two economical and efficient methods are proposed to fabricate magnetic films using various types of magnetic nanoparticle composites. These films are characterized to demonstrate good magnetic properties, such as high magnetization saturation and high relative permeability. Then by utilizing the flexibility offered by the additive manufacturing technology, we are able to design and fabricate novel reconfigurable devices using these magnetic films. Due to the high permeability, we can achieve a good amount of size miniaturization; and with good magnetization saturation, we can tune the filter and cavity resonator either in a wideband manner or fine tuning. Also by carefully choosing the antenna type and the film position, we can obtain enhanced antenna gain and efficiency along with the size reduction, which is not realizable using the transnational methods. This work paves the way for using additive manufacturing technology and low cost magnetic materials to design and fabricate novel reconfigurable RF devices in a low cost and light-weight package.

BIBLIOGRAPHY

BIBLIOGRAPHY

[1] https://formlabs.com

[2] https://www.stratasys.com

[3] https://optomec.com/

[4] J. D. Adam, L. E. Davis, G. F. Dionne, E. F. Schloemann and S. N. Stitzer, "Ferrite devices and materials," in *IEEE Transactions on Microwave Theory and Techniques*, vol. 50, no. 3, pp. 721–737, March 2002.

[5] David M. Pozar, *Microwave Engineering*, 4th ed. New Jersey: John Wiley & Sons, Inc., 2012. ch.8, pp.422–426.

[6] Liu, L., et al., "Compact harmonic filter design and fabrication using IPD technology,"*IEEE Transactions on Components and Packaging Technologies*, Vol. 30, No. 4, 556–562, 2007.

[7] Kim, D. W., et al., "High performance RF passive integration on a Si smart substrate for wireless applications," *Etri Journal*, Vol. 25, No. 2, 65–72, 2003.

[8] Fan Cai, Wasif Tanveer Khan, John Papapolymerou. "A Low Loss X-band Filter Using 3-D Poly jet Technology," in *IEEE MTT-S Int. Microwave Symp.* ,Phoenix, AZ, May 2015 pp. 1–4.

[9] Constantine A. Balanis, *Antenna Theory Analysis and Design*, 4th Edition. New Jersey: John Wiley & Sons, Inc., 2016. ch.10, pp.559–580.

[10] F. Cai et al., "Low-Loss 3-D Multilayer Transmission Lines and Interconnects Fabricated by Additive Manufacturing Technologies," in *IEEE Transactions on Microwave Theory and Techniques*, vol. 64, no. 10, pp. 3208–3216, Oct. 2016.

[11] C. X. Wang et al.,"Cellular architecture and key technologies for 5G wireless communication networks," in *IEEE Communications Magazine*, vol. 52, no. 2, pp. 122–130, February 2014.

[12] J. P. Magalhes, J. M. N. Vieira, R. Gmez-Garca and N. B. Carvalho, "Bio-Inspired Hybrid Filter Bank for Software-Defined Radio Receivers," in *IEEE Transactions on Microwave Theory and Techniques*, vol. 61, no. 4, pp. 1455–1466, April 2013.

[13] T. K. Thrivikraman, A. Madan, and J. D. Cressler, "On the large-signal robustness of SiGe HBT LNAs for high-frequency wireless applications," in *Proc. IEEE Radio Wireless Symp. (RWS)*, Jan. 2010, pp. 364–367.

[14] M. van Wanum and F. E. van Vliet, "A 58-dBm S-band limiter in standard 0.25-μm BiCMOS technology," *IEEE Trans. Microw. Theory Techn.*, vol. 61, no. 8, pp. 3034–3042, Aug. 2013.

[15] J. Givernaud et al., "Microwave power limiting devices based on the semiconductormetal transition in vanadiumdioxide thin films," *IEEE Trans. Microw. Theory Techn.*, vol. 58, no. 9, pp. 2352–2361, Sep. 2010.

[16] T. R. Billeter, "EPR frequency-selective limiter," *Proc. IEEE*, vol. 56, no. 3, pp. 370–371, Mar. 1968.

[17] F. Ramirez, R. Melville, A. Suarez, and J. S. Kenney, "Nonlinear analysis and design of frequency selective limiters based on parametric circuits," in *IEEE MTT-S Int. Microw. Symp. Dig.*, Jun. 2008, pp. 947–950.

[18] J. C. S. Chieh and J. Rowland, "X-band frequency selective limiter using absorptive notch filters embedded multiplexers," 2017 *IEEE MTT-S International Microwave Symposium (IMS)*, Honololu, HI, USA, 2017, pp. 1919–1922.

[19] E. J. Naglich and A. C. Guyette, "Frequency-Selective Limiters Utilizing Contiguous-Channel Double Multiplexer Topology," in *IEEE Transactions on Microwave Theory and Techniques*, vol. 64, no. 9, pp. 2871–2882, Sept. 2016.

[20] J. D. Adam and F. Winter, "Magnetostatic Wave Frequency Selective Limiters," in *IEEE Transactions on Magnetics*, vol. 49, no. 3, pp. 956–962, March 2013.

[21] J. D. Adam. "Mitigate the Interference: Nonlinear Frequency Selective Ferrite Devices," *IEEE Microwave Magazine*, Vol. 15, No. 6, pp. 45–56, Sep–Oct. 2014.

[22] F. K. H. Gellersen, F. M. Klichowski, A. G. C. Rusche and A. F. Jacob, "Barium hexaferrite films prepared by means of the sol-gel method for self-biased nonreciprocal microwave devices," *2016 German Microwave Conference (GeMiC)*, Bochum, 2016, pp. 221–224.

[23] F. K. H. Gellersen, J. Peschel, A. Ochsenfarth and A. F. Jacob, "Scandium-doped barium hexaferrite thin-films for nonreciprocal satellite components," *2017 Topical Workshop on Internet of Space (TWIOS)*, Phoenix, AZ, 2017, pp. 1–4.

[24] A. L. Geiler and V. Harris. "Atom Magnetism," *IEEE Microwave Magazine*, Vol 15, No. 6, pp. 66–72, Sep–Oct. 2014

[25] M. A. Morton, C.R. Vestal, J. Papapolymerou, Z.J. Zhang. "Fabrication and Characterization of Spinel Magnetic Nanoparticle Thin Film Transmission Lines," *33rd European Microwave Conference*, 2003,Volume: 3, pp. 1307–1309, 7–9 Oct. 2003.

[26] Y. He, S. Pavlidis, W. Y. Chen, E. Drew, Z. J. Zhang and J. Papapolymerou, "Fabrication and characterization of CPW transmission lines with CoFe2O4 nanomagnetic thin films," *2017 IEEE Radio and Wireless Symposium (RWS)*, Phoenix, AZ, 2017, pp. 72–75.

[27] C. Kittel, "Interpretation of the anomalous Larmor frequencies in ferromagnetic resonance experiment," *Phys. Rev.*, vol. 71, no. 4, pp. 270–271, 1947

[28] Chen, W.Y. 2018 "Aminolytic synthesis and ferromagnetic resonance of cobalt and manganese based spinel ferrite nanoparticle", Doctorate of Philosophy in Chemistry, Georgia Institute of Technology, Atlanta, GA.

[29] L. Hernandez, Y. He, A. Kaur, J. Papapolymerou and P. Chahal, "Low-loss RF filter through a combination of additive manufacturing and thin-film process," *2017 IEEE Radio and Wireless Symposium (RWS)*, Phoenix, AZ, 2017, pp. 114–116.

[30] http://www.stratasys.com/polyjet-technology

[31] Gokhan Mumcu, Thomas Weller, "Small Antennas and Miniaturization Techniques," *Antenna Engineering Handbook*, J. L. Volakis, 5th ed. New York: McGraw Hill, 2018, ch.10.

[32] Z. Shao and Y. P. Zhang, "Differential Shorted Patch Antennas," in *IEEE Trans. Antennas Propag.*, vol. 67, no. 7, pp. 4438–4444, July 2019.

[33] J. P. Gianvittorio and Y. Rahmat-Samii, "Fractal antennas: a novel antenna miniaturization technique, and applications," in *IEEE Antennas Propag. Mag.*, vol. 44, no. 1, pp. 20–36, Feb. 2002.

[34] D. H. Schaubert, D. M. Pozar and A. Adrian, "Effect of microstrip antenna substrate thickness and permittivity: comparison of theories with experiment," in *IEEE Trans. Antennas Propag.*, vol. 37, no. 6, pp. 677–682, June 1989.

[35] D. Sievenpiper, Lijun Zhang, R. F. J. Broas, N. G. Alexopolous and E. Yablonovitch, "High-impedance electromagnetic surfaces with a forbidden frequency band," in *IEEE Trans. Microw. Theory Techn.*, vol. 47, no. 11, pp. 2059–2074, Nov. 1999.

[36] K. Buell, H. Mosallaei and K. Sarabandi, "A substrate for small patch antennas providing tunable miniaturization factors," in *IEEE Trans. Microw. Theory Techn.*, vol. 54, no. 1, pp. 135–146, Jan. 2006.

[37] A. D. Brown, J. L. Volakis, L. C. Kempel and Y. Botros,"Patch antennas on ferromagnetic substrates," in *IEEE Trans. Antennas Propag.*, vol. 47, no. 1, pp. 26–32, Jan. 1999.

[38] R. V. Petrov, A. S. Tatarenko, S. Pandey, G. Srinivasan, J. V. Mantese, and R. Azadegan, "Miniature antenna based on magnetoelectric composites," in *Electron. Lett.*, vol. 44, no. 8, pp. 506–507, 10 April, 2008.

[39] J. Lee, Y. Hong, S. Bae, G. S. Abo, W. Seong and G. Kim, "Miniature Long-Term Evolution (LTE) MIMO Ferrite Antenna," in *IEEE Antennas Wireless Propag. Lett.*, vol. 10, pp. 603–606, 2011.

[40] J. Lee, J. Lee, K. Min and Y. Cheon, "Miniaturized Antennas With Reduced Hand Effects in Mobile Phones Using Magneto-Dielectric Material," *IEEE Antennas Wireless Propag. Lett.*, vol. 13, pp. 935–938, 2014.

[41] P. J. Rainville and F. J. Harackiewicz, "Magnetic tuning of a microstrip patch antenna fabricated on a ferrite film," in *Microwave and Guided Wave Letters*, vol. 2, no. 12, pp. 483–485, Dec. 1992.

[42] H. How, P. Rainville, F. Harackiewicz and C. Vittoria, "Radiation frequencies of ferrite patch antennas," in *Electron. Lett.*, vol. 28, no. 15, pp. 1405–1406, 16 July 1992.

[43] G. M. Yang et al., "Tunable miniaturized patch antennas with self-biased multilayer magnetic films," in *IEEE Trans. Antennas Propag.*, vol. 57, pp. 2190–2193, July 2009.

[44] G. Yang et al., "Planar Annular Ring Antennas With Multilayer Self-Biased NiCo-Ferrite Films Loading," in *IEEE Trans. Antennas Propag.*, vol. 58, no. 3, pp. 648–655, March 2010.

[45] G. M. Yang et al., "Loading effects of self-biased magnetic films on patch antennas with substrate/superstrate sandwich structure," in *IET Microw. Antennas Propag.*, vol. 4, no. 9, pp. 1172–1181, September 2010.

[46] Y. He, W. Chen, E. Drew, Z. J. Zhang and J. Papapolymerou, "Fabrication and Characterization of $CoFe_2O_4$ and $MnFe_2O_4$ Nanomagnetic Thin Films for RF Applications," *IEEE Trans. Compon. Packag. Manuf. Technol.*, vol. 9, no. 5, pp. 973–983, May 2019.

[47] Y. He, E. Drew, Z. J. Zhang, T. Hogan and J. Papapolymerou, "Compact BandStop Filter Utilizing Low Cost Solution Cast Nanomagnetic Thin Films," *2019 IEEE MTT-S International Microwave Symposium (IMS)*, Boston, MA, 2019, pp. 1118–1121.

[48] Y. He and J. Papapolymerou, "Compact Microstrip Patch Antenna Utilizing Low Cost Solution Cast Nanomagnetic Thin Film," *2019 IEEE International Symposium on Antennas and Propagation & USNC/URSI National Radio Science Meeting*, Atlanta, GA, 2019, pp. 1531–1532.

[49] [Online] http://www.rogerscorp.com/documents/730/index.aspx

[50] Constantine A. Balanis, *Antenna Theory: Analysis and Design*, 4th ed. New Jersey: John Wiley & Sons, Inc., 2016. ch.14, pp.788–815

[51] D. Jackson and N. Alexopoulos, "Gain enhancement methods for printed circuit antennas," in *IEEE Trans. Antennas Propag.*, vol. 33, no. 9, pp. 976–987, September 1985.

[52] J. M. Edwards and G. M. Rebeiz, "High-Efficiency Elliptical Slot Antennas With Quartz Superstrates for Silicon RFICs," in *IEEE Trans. Antennas Propag.*, vol. 60, no. 11, pp. 5010–5020, Nov. 2012.

[53] P. M. Ikonen, K. N. Rozanov, A. V. Osipov, P. Alitalo, and S. A.Tretyakov, "Magnetodielectric substrate in antenna miniaturization: Potential and limitations," in *IEEE Trans. Antennas Propag.*, vol. 54, pp. 3391–3399, Nov. 2006.

[54] N. Popandian, P. Balay, A. Narayanasamy, "Electrical conductivity and dielectric behaviour of nanocrystalline $NiFe_2O_4$ spinel," in *J. Phys.: Condens. Matter* 14, 3221, 2002.

[55] David R. Jackson, "Microstrip antennas," *Antenna Engineering Handbook*, J. L. Volakis, 5th ed. New York: McGraw Hill, 2018, ch.7.

[56] R. C. Hansen and M. Burke, "Antennas with magneto-dielectrics," *Microw. Opt. Tech. Lett.*, vol. 26, no. 2, pp. 75–78, Jul. 2000.

[57] M. I. M. Ghazali, S. Karuppuswami, A. Kaur and P. Chahal, "3-D Printed Air Substrates for the Design and Fabrication of RF Components," in *IEEE Trans. Compon. Packag. Manuf. Technol.*, vol. 7, no. 6, pp. 982–989, June 2017.

[58] L. Young, G. L. Matthaei and E. M. T. Jones, "Microwave Bandstop Filters with Narrow Stop Bands," *PGMTT National Symposium Digest*, Washington, DC, USA, 1962, pp. 46-51.

[59] G. M. Rebeiz, K. Entesari, I. C.Reines, S. J. Park, M. A. El-Tanani, A. Grichener, and A. R.Brown, "Tuning in to RF MEMS," *IEEE Microw. Mag., Focused Issue Feature*, pp. 5072, Oct. 2009.

[60] J. Papapolymerou, C. Lugo, Z. Zhao, X. Wang, and A. Hunt, "A miniature low-loss slow-wave tunable ferroelectric bandpass filter from 11-14 GHz," in *IEEE MTT-S Int. Microw. Symp. Dig.*, San Francisco, CA, USA, Jun. 2006, pp. 556-559.

[61] T. Y. Yun and K. Chang, "Piezoelectric-transducer-controlled tunable microwave circuits," *IEEE Trans. Microw. Theory Tech.*, vol. 50, pp. 1303-1310, May 2002.

[62] A. S. Tatarenko, V. Gheevarughese, and G. Srinivasan, "Magnetoelectric microwave bandpass filter," *Electron. Lett.*, vol. 42, pp. 540-541, Apr. 2006.

[63] G. Yang, J. Wu, J. Lou, M. Liu and N. X. Sun, "Low-Loss Magnetically Tunable Bandpass Filters With YIG Films," in *IEEE Transactions on Magnetics*, vol. 49, no. 9, pp. 5063–5068, Sept. 2013.

[64] S. Adhikari, S. Hemour, A. Ghiotto and K. Wu, "Magnetically Tunable Ferrite-Loaded Half-Mode Substrate Integrated Waveguide," in *IEEE Microwave and Wireless Components Letters*, vol. 25, no. 3, pp. 172–174, March 2015.

[65] Y. He et al., "Integrated Tunable Bandstop Filter Using Self-Biased FeGaB/Al_2O_3 Multilayer Thin Film," in *IEEE Transactions on Magnetics*, vol. 54, no. 9, pp. 1–4, Sept. 2018.

[66] Y. He, P. Chahal and J. Papapolymerou, "A lego-like reconfigurable cavity using 3-D Polyjet technology," *2017 IEEE MTT-S International Microwave Symposium (IMS)*, Honolulu, HI, 2017, pp. 525–528.

[67] C. Kittel, "Interpretation of the anomalous Larmor frequencies in ferromagnetic resonance experiment," *Phys. Rev.*, vol. 71, no. 4, pp. 270-271, 1947.

[68] Jia-Sheng Hong, M. J. Lancaster, *Microstrip Filters for RF/Microwave Applications*, John Wiley & Sons, 2001.

[69] http://www.stratasys.com/polyjet-technology

[70] S. Park, I. Reines, C. Patel and G. M. Rebeiz, "High-Q RF-MEMS 4–6 GHz Tunable Evanescent-Mode Cavity Filter," in *IEEE Trans. Microw. Theory Techn.*, vol. 58, no. 2, pp. 381–389, Feb. 2010.

[71] S. Courreges, Y. Li, Z. Zhao, K. Choi, A. Hunt and J. Papapolymerou, "Ferroelectric Tunable Bandpass Filters for Ka-Band Applications," *2008 38th European Microwave Conference*, Amsterdam, 2008, pp. 55–58.

[72] S. Adhikari, Y. Ban and K. Wu, "Magnetically Tunable Ferrite Loaded Substrate Integrated Waveguide Cavity Resonator," in *IEEE Microw. Wireless Compon. Lett.*, vol. 21, no. 3, pp. 139–141, March 2011.

[73] C. Guo et al., "Shaping and Slotting High-Q Spherical Resonators for Suppression of Higher Order Modes," *2019 IEEE MTT-S International Microwave Symposium (IMS)*, Boston, MA, USA, 2019, pp. 1205–1208.

[74] Constantine A. Balanis, *Advanced engineering electromagnetics*, 4th ed. New Jersey: John Wiley & Sons, Inc., 2016. ch.10, pp. 561–568.

[75] David M. Pozar, *Microwave Engineering*, 4th ed. New Jersey: John Wiley & Sons, Inc., 2012. ch.10, pp. 305–308.